Switchless Electrostatic Vibration Micro-Power Generators

by

Mohamed A. E. Mahmoud

A thesis
presented to the University of Waterloo
in fulfillment of the
thesis requirement for the degree of
Doctor of Philosophy
in
Electrical and Computer Engineering

Waterloo, Ontario, Canada, 2010

Abstract

Energy harvesting from the surrounding environment has become a hot topic in research as an alternative powering solution. The concept deals with scavenging, as well as, harvesting energy from the surrounding energy sources. Harvesting vibrations, through Micro-Power Generators (MPGs), has drawn a lot of attention recently due to the reduction in the power requirement of the current sensors and Integrated Circuits (ICs), and the abundance of ambient vibrations in many environments.

Vibration Micro-Power Generators (VMPGs) use one of three transduction mechanisms: piezoelectric, electromagnetic or electrostatic. Although electrostatic MPGs are the most compatible mechanism with ICs technology, many challenges face their optimal operation including low efficiency due to power electronics switching losses, the need for pre-charge, and the inability to operate in vibration environments with low frequencies and amplitudes.

The objective of this thesis is to develop novel electrostatic micro-power generators using switchless architecture to achieve low cost, small footprint, self-sustained and optimal power generation in different vibration environments including low frequencies and amplitudes.

The first electrostatic MPG uses an out-of-plane capacitive transducer. The new generator is sensitive enough to extract output power at very low base excitations. It is designed to use ready-made electret as a charging source and is therefore portable and self-sustained. Moreover, the new MPG can be configured as a wideband MPG in its impact mode of operation. A bandwidth of up to 9 Hz has been realized in this mode of operation. An improved version of the MPG is also presented that produces almost 1mW output power at a base excitation amplitude and frequency of $0.08\,g$ (RMS) and 86 Hz. Two nonlinear models developed for the free-flight and impact modes of operation of the MPG are presented to allow future analysis and optimization of the system.

The second electrostatic MPG uses a novel interdigitated in-plane parallel plate electrostatic transducer. The new implementation can achieve 78% more output power than the original cited implementation. The MPG is fabricated using MEMS surface micromachining. The MPG introduces a new beam suspension system in which the source voltage is unlimited by the pull-in instability and low MPG center frequency can be realized. The MPG uses charged silicon nitride as a charging source. The MPG produces 65mV at a base acceleration amplitude and frequency of $2\,g$ and 1.1 kHz. The prototype achieves 27% less resonance frequency with only one eight the size of the previous implementation.

A third electrostatic MPG architecture is introduced. The new architecture eliminates the need for restoring force elements (springs) in the MPG. The architecture can realize arbitrarily low MPG center frequency. It is suitable for both rectilinear and cylindrical structures and can be used with different vibration energy transduction methods. A prototype is fabricated and tested to demonstrate the feasibility of this architecture. The center frequency of the prototype is found to be 2 Hz demonstrating low frequency operation.

The nonlinear behavior of switchless (continuous) electrostatic MPGs is further studied for optimal power operation. A consistent approximate analytical solution is developed to describe the nonlinear behavior of switchless comb-finger electrostatic MPGs. The method of multiple scales is used to develop such model. The model was found to be valid for MPGs operating under tight electromechanical coupling conditions and for moderately-large base excitations.

Acknowledgements

All praise is due to God, Most Gracious, Most Merciful, Whose bounties and blessings are ever dominating throughout my life. I would like to express my deep gratitude and appreciation to my supervisors, Prof. Raafat Mansour and Ehab El-Saadany. I am extremely grateful to their understanding and support throughout the years I have spent in Waterloo.

Throughout the period I spent doing my Ph.D., I received tremendous support from many people. I am grateful to Prof. Eihab Abdel-Rahman for his tremendous help and guidance. I am also grateful to Prof. Shesha Jayaram and Emad Sharifi-Ghazvini for allowing me to use their lab equipment and helping me in testing the electret.

I also want to acknowledge my friends and colleagues from the Center for Integrated RF Engineering (CIRFE) for the help and support they provided to me during this journey. I always enjoyed the technical discussions I had with Mostafa Soliman, Maher Bakri-Kassem, Ahmed Bauomy, Siamak Fouladi, and Arash Fomani. I will miss their company.

Many thanks go to Bill Jolley, the CIRFE lab manager, who was very patient and supportive to all my demands and continuous requests and questions, Phil Regier and Fernando Hernandez, ECEs system administrators, and Louise Green and Wendy Boles for taking care of the paperwork requirements.

My wife, Eman, shared with me every day throughout the course of this work. Her support, patience, and understanding played a major role in helping me finish this thesis. My daughters, Fatma and Asma'a, brought so much joy to my life which has been and continue to be a great source of encouragement.

My deepest gratitude to my mother and father for their ever continuous support, encouragement, and prayers. No words of appreciation could ever reward them for all they have done for me. I am, and will ever be, indebted to them for all achievements in my life.

Dedication

To my parents, Ahmed El-Sheikh and Nagwa Darwish, with love and appreciation.

To my wife, Eman, and children, Fatma and Asma'a

Contents

List of Tables

List of Figures

List of Abbreviations

RFIDs	Radio-Frequency Identifications
ICs	Integrated Circuits
VEH	Vibration-based energy harvester
VMPG	Vibration Micro-Power Generator
MPG	Micro-Power Generator
MEMS	Micro Electro Mechanical Systems
BSN	Body Sensor Network
RF	radio frequency
PZ	Piezoelectric
ES	Electrostatic
EM	Electromagnetic
PZT	Lead Zirconate Titanate

Chapter 1

Introduction

1.1 Motivations

Nowadays, with the advances of ICs and low power applications, it has become easy to operate sensors with an extremely low power. These sensors with the advances of wireless communications led to the evolution of a new concept known as Body Sensor Network (BSN). Using advanced new architecture, low-voltage, and low-power transceivers' circuits, the power consumption of these sensors systems can go as low as 20 μW [21]. In such applications, the power required is extremely low and requires nearly a life-time power source to operate it, especially in embedded and biomedical systems.

In the last decade, the storage densities of batteries have grown substantially for both primary and secondary batteries. Commercial Lithium-ion batteries, which are known for their highest energy density, have typical capacities of up to 160 W.h/kg or 1.1 kj/cm^3 [21]. These batteries offer a good solution for these systems when it comes to 1$\sim$2 years of operation. However, for life-time operation where sensors are required to operate indefinitely without the need for batteries to be replaced, or in the case of embedded sensors that are not easily accessible, batteries or constant energy sources reach their limitations. Moreover, even drained batteries represent a huge risk to the environment since they contain hazardous chemical materials

As an alternative, energy harvesting from the surrounding environment has become a hot topic in research as an alternative powering solution over the last few years. This concept deals with scavenging as well as harvesting energy from the surrounding energy sources. Although, the concept is not new, it drew a lot of attention due to the advances and the reduction in the power requirement of the current sensors and ICs.

Vibration-based energy harvesters (VEHs) represent one of the appealing methods currently involved in research to produce electrical energy in the range of micro-watts [15]. These vibration harvesters or MPGs fall into one of three categories: piezoelectric, electromagnetic or electrostatic. Piezoelectric and electromagnetic have drawn a lot of research interest in the past years because of their large power density and the robustness of their operation theory. However, the implementation of these two types of MPGs requires a magnetic or ceramic material that is not fully compatible with the current ICs fabrication technology.

On the other hand, electrostatic VEHs are fully compatible with the ICs fabrication technologies as they involve the use of one or more variable capacitors as an energy transducer. Therefore, implementing MPGs using this conversion method promotes their seamless integration in sensors.

However, all the commercial vibrational MPGs are either piezoelectric or electromagnetic [22]. Several operational limitations have prohibited electrostatic VEHs from being efficient power generators. The presence of power electronics for power handling during the energy conversion of switched electrostatic VEHs lowers the conversion efficiency and thus the harvested energy. The need for an electrical source for initial capacitance charging also limits their life-time operation. Moreover, the lack of rigorous study of the electromechanical coupling in electrostatic MPGs affected the optimization of the harvesters for power generation and led to a superficial conclusion of the low power density of the electrostatic technique in comparison to the piezoelectric and electromagnetic harvesting techniques.

Moreover, electrostatic energy harvesters share the same design challenges facing vibration energy harvester, including the need for miniaturization, low cost fabrication, and operation in low frequency vibration environments.

1.2 Objectives

The purpose of this thesis is to propose novel electrostatic micro-power generators using switchless architecture to achieve low cost, small footprint, self-sustained, and optimal power generation in different vibration environments, including low frequencies and amplitudes. Rigorous models are developed to account for the electromechanical coupling and the nonlinear behavior of the mechanical system. These models are used to design the electrostatic MPGs under different design constrains. Validation of the new architectures is carried through fabrication of experimental prototypes and testing them to ensure the achievement of the design goals.

To achieve this objective, we developed a portfolio of switchless (continuous) electrostatic MPGs. The course of development efforts took the following three stages:

1. Development of an out-of-plane electrostatic MPG using low-cost fabrication for self-sustained, wideband, and optimal power generation in low-amplitude vibration environments.

2. Development of two electrostatic MPGs using an in-plane interdigitated transducer for small form-factor devices and vibration environments with low vibration frequencies.

3. Study of the electromechanical coupling in electrostatic MPGs to understand the effect of the interaction between the MPG's transducer and the mechanical oscillator on the performance.

1.3 Thesis outline

The thesis is organized in six chapters. The first chapter outlines research motivations and objectives. A literature review of the existing vibration energy harvesters with a focus on electrostatic vibration harvesters is presented in Chapter 2.

Chapter 3 illustrates the transducers architectures used for switchless energy harvesters and contrasts their ability to harvest energy. The chapter then focuses on out-of-plane transducers and their use in energy harvesting. An energy harvester prototype using this transducer is built and tested to demonstrate the power generation of the transducer. Using electret as a charging source, we built a self-sustained MPG prototype using precision machining. The MPG performance is tested and modeled for different operation regions, including free-flight and impact modes. An improved version of the MPG architecture is developed to demonstrate achievement of the design goals.

Chapter 4 presents the in-plane electrostatic MPGs. The interdigitated parallel plate transducer design is illustrated and compared with other existing designs. The implementation of this architecture in two different MPGs is presented. The 1st MPG addresses the miniaturization challenges in MPGs. A MEMS prototype of the novel structure is designed and fabricated using a combination of standard fabrication using a polysilicon multi-user MEMS process (PolyMUMPs) and an on-site fabrication and assembly. The 2nd MPG aims for low frequency operation using a springless suspension system based on a rail and carriage. The model equations and testing results of a fabricated prototype are also presented in this chapter.

Chapter 5 studies the electromechanical coupling in electrostatic MPGs using an existing architecture as a test case. Analysis of the MPG's linearized model is carried out to identify different regions of operations and the limitation of the current linearized model. The method of multiple scales is used to obtain a uniformly-consistent second-order solution of the nonlinear system. The solution is validated with the experimental results obtained from the literature and the numerical solution of the system differential equations.

Chapter 6 summarizes the contributions of the thesis and points out the problems that will be solved in future work.

Chapter 2

Literature Survey

2.1 Introduction

Power sources are key components in wireless systems. They determine the operating distance, duty cycle, and the system processing power. Improving the existing power sources or using new techniques aim to reduce the footprints of these systems and obtain more sustainable operation. Numerous techniques were proposed in the literature to power wireless systems [2, 23–27].

These power sources can be categorized into two main groups: constant energy and constant power sources. Constant energy sources are like batteries and fuel cells. These sources have certain amount of energy that they deliver and then recharging/refueling is needed. As a result, these sources have the disadvantage of being frequently serviced, depending on their discharge rates.

Batteries can be primary (single charging) or secondary (rechargeable several times) types. Different materials are used in batteries, including acidic, alkaline, Nickel-Cadmium (Ni-Cd), Nickel-Metal Hydride (Ni-MH), and Lithium-ion (Li-ion) types [26]. Li-ion batteries have the highest energy density reaching 160 W.h/kg or 1.1 kj/cm^3 [21].

The gravimetric energy density of fuel cells is expected to be three to five times larger than that of Li-ion cells and more than ten times than that of Ni-Cd or Ni-MH batteries, whereas the volumetric energy density is six to seven times larger than that of Li-ion [24]. Fuel cell's gravimetric energy densities reaches 8 kW.h/kg [21]. However, the use of fuel requires conversion and exhaustion mechanisms that complicate their operation when being miniaturized.

On the other hand, constant power sources rely on the concept of energy harvesting to obtain sustainable energy supply. Energy harvesting is defined as the process of extracting electrical power from ambient sources. This approach has recently gained a lot of interest in academia. Although the power obtained from the energy harvesting is generally less than constant energy sources and depends on the operating environment, the concept is boosted by the advances in electronics and ICs fabrication technologies. Different energy harvesting techniques have been reported in the literature, including light, radio frequency (RF), temperature gradient, solar energy, and vibrations [24].

Solar energy is the most successful and conventional source to scavenge energy. The energy conversion efficiency of a solar cell ranges from 30% for inexpensive crystalline silicon to 10% for flexible amorphous silicon [27]. The amount of harvested energy ranges from mW to μW, depending on the location of operation whether it is outdoor or indoor as well as the climate conditions whether it is sunny or cloudy. Therefore, solar cells are very good source for outdoor operation and stable climate conditions, but fall behind other sources when operated indoor.

Temperature gradient and surrounding heat energy harvesting are another way to obtain electrical energy in the range of 10 μW/cm^3 [24]. However, they depend on the temperature gradient, which can change during the operation of the generator.

Vibration energy represents one of the sources of energy that exists everywhere. Vibration energy can be obtained from nearby machinery, people, or animal activities. These sources vary widely in their strength and frequency of vibration. Therefore, availability of such an energy source makes it very appealing and makes it fit in many applications, like automotive and biomedical applications.

The energy generated can theoretically reach up to 800 μW/cm^3 when operating at a resonance condition, depending on the strength of the source [15]. Different mechanisms have been reported for harvesting such energy starting from watches that use the vibration energy as a source to micro-generators that scavenge such energy for microelectronics' circuit operation [21, 28]. However, vibration energy has not yet received much attention in comparison with solar energy. Therefore, vibration energy has been chosen as the focus of this research in order to enhance its energy scavenging and obtain higher output power density.

2.2 Vibration Energy Harvesters

Using ambient vibrations for energy harvesting can provide an adequate power solution for wireless sensors in numerous environments. The existence of different vibration sources with different frequencies and amplitudes within the environment allows different levels of power generation. The vibration sources can be from moving bodies whether it is living or nonliving things, building components like doors and floors, and domestic and industrial machines.

Vibrations can be periodic with fundamental frequency and harmonics, random, or single event motions, such as impacts and triggered motions occurring at low frequencies. Most of the ambient vibration sources are periodic. They are defined through acceleration amplitudes at their fundamental frequencies. Different vibration sources resulting from different activities have been measured and characterized in [1–3]. Table 2.1 lists these sources with their acceleration amplitudes at their fundamental frequencies.

Table 2.1: Examples of vibration sources. [1–3]

Source	**Acceleration (m/s^2)**	**Frequency (Hz)**
Person nervously tapping their heel	3	1
Car instrument panel	3	13
Parking meter	0.0327	13.8
A/C duct center (Low setting)	0.0328	15.7
Small tree	0.003	30.0
Car hood - 750 rpm	0.0744	35.6
A/C duct side (High setting)	0.0990	53.8
A/C duct center (Low setting)	0.0398	55
Base of 3-axis machine tool	10	70
CD on notebook computer	0.6	75
Windows next to a busy road	0.7	100
Microwave oven top	1.11	120
Clothes dryer	3.5	121
Door frame just after door closes	3	125
Office desk	0.0879	120.0
Car hood - 3000 rpm	0.257	147.5
Microwave oven side	4.21	148.1
Bridge railing	0.0215	171.3
Car engine compartment	12	200
Refrigerator	0.1	240
Computer side panel	0.0402	276.3
Rotational machines	$0.196 \sim 0.784$	$1 \sim 5$k

The vibration sources listed in Table 2.1 fall into three main groups: vibration due to human activities, domestic vibrations, and rotational machine vibrations. Human-based vibrations are characterized by low fundamental frequencies (<10 Hz). Vibrations due to domestic activities and machines have fundamental frequencies below 300 Hz and vary significantly in their amplitudes. Rotational machines vibrations can have large fundamental frequencies due to the high rotational speed of their shafts.

Vibration energy harvesters generate electrical energy by allowing an inertial mass to vibrate relative to a frame. This relative displacement is used to convert mechanical energy to electrical energy using a transducer. The transduction mechanism can be through straining a piezoelectric material, moving a conductor in a magnetic field, or changing the capacitance of a charged capacitor. As a result, vibration energy converters are divided according to the transduction method into three main categories: piezoelectric, electromagnetic, and electrostatic. In the reminder of the chapter, an overview of the theory behind the three methods and the existing literature are presented, illustrating the main advantages and disadvantages of each type with a special focus on the electrostatic technique.

2.3 Piezoelectric Energy Harvesters

Piezoelectric (PZ) vibration energy harvesters use ceramic materials with good piezoelectric property to transduce vibration to voltage output. The piezoelectricity phenomenon is the deformation of materials in the presence of an electric field or the production of an electric charge when the material is mechanically deformed. The governing equations for the operation of a piezoelectric materials are

$$\begin{aligned} \varepsilon_m &= \frac{\sigma_m}{Y} + d.E \\ D &= \epsilon E + d.\sigma_m \end{aligned} \tag{2.1}$$

where ε_m and σ_m are the mechanical strain and stress on the ceramic piece, respectively; E and D are the electric field and displacement across the the ceramic piece; Y, d, and ϵ are the modulus of elasticity, the piezoelectric strain coefficient, and the dielectric constant of the piezoelectric material, respectively. The first equation in (2.1) is simply Hooke's law with an added term to account for the effect of the electric field, whereas the second equation is the dielectric equation but with an added term to account for the mechanical stress.

Piezoelectric micro-power generators (PZ MPGs) can be classified according to the method of operation into three types: impact-coupled, direct-coupled, and inertial-coupled types [28]. Impact-coupled PZ MPGs generate output voltage through impacting the piezoelectric material by a moving mass (e.g., a ball). Direct-coupled PZ MPGs apply compressive forces directly to the piezoelectric material. These two types are well suited for low-frequency vibration sources (e.g., human motion). Inertial-coupled PZ MPGs use an inertial mass in a frame to couple the vibration to the PZ structures. These structures are mechanically stressed during their motion, leading to voltage generation. This type of generators is not suitable for low-frequency operation as they efficiently work around the natural frequency of the suspended structure.

PZ MPGs have many advantages and some limitations [28]. They offer the simplest harvesting approach, whereby vibrations are converted into a voltage output by using an electroded PZ material. They generate large output voltages but with limited currents. They are suitable for miniaturization through micro-fabrication where several processes exist for depositing piezoelectric films. On the other hand, the transduction efficiency of PZ MPGs is limited by the piezoelectric material properties rather than by their design. Moreover, the ceramic nature of the piezoelectric material limit the lifetime and durability of the generator. The load impedance of this generator type needs to be high for efficient generation (> 100 kΩ).

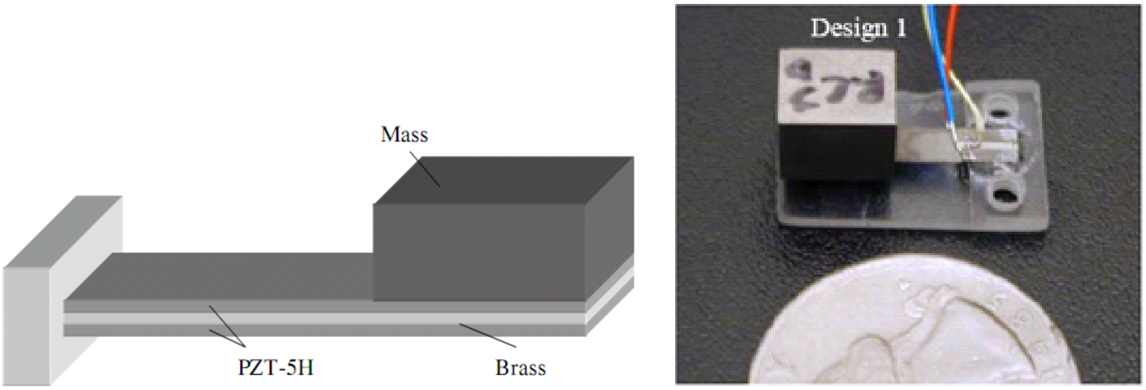

(a) (b)

Figure 2.1: Proposed piezoelectric MPG [2]: (a) Schematic, (b) Picture.

Different authors [21, 28–30] have reviewed the existing PZ MPGs. From these cited MPGs, Roundy et al. [2] have demonstrated the use of thin film piezoelectric films in MPGs. They fabricated an inertial-type PZ MPG prototype. The prototype was fabricated by attaching a PZT-5A shim to each side of a steel center beam. A cubic mass made from an alloy of tin and bismuth was attached to the end and the generator was tuned to resonate at 120 Hz. The volume of the prototype is 1 cm^3. A model of the developed piezoelectric generator, Figure 2.1, was constructed and validated. For an input vibration of 2.25 m/s^2 at about 120 Hz, the maximum power density generated in a resistive load is 335 μW/cm^3, whereas that generated in a purely capacitive load is 180 μW/cm^3.

The Volture PEH20W PZ MPG offered by Midé, Inc. is an example of the existing commercial solutions in the VMPGs market [8]. Figure 2.2 shows a picture of the packaged MPG. The volume of the MPG with the power electronics is around 40.5 cm^3. The system produces up to 16 mW at 80 Hz for 1g peak vibration amplitude. The harvesting bandwidth is 3 Hz. The resulting power density is equal to 395 μW/cm^3 which is close to Roundy et al.'s MPG power density.

Figure 2.2: Volture PZ MPG offered by Mide, Inc [8].

2.4 Electromagnetic Harvesters

The operation principle behind electromagnetic transduction is explained using Faraday's law. He states that the change in the magnetic field lines passing through a closed-loop fixed conductor leads to the generation of current in the conductor as shown in Figure 2.3. The resulting voltage is equal to

$$V_{induced} = -\frac{d\phi_B}{dt} \tag{2.2}$$

where ϕ_B is the magnetic flux.

The conductor typically takes the form of a coil and the electric current is generated by the relative movement of the magnet and coil. The generated voltage depends upon the strength of the magnetic field B, the velocity of the relative motion v, and the number of turns of the coil N. Using (2.2), the resulting open circuit voltage across the coil is

$$V_{induced} = NBLv \tag{2.3}$$

where L is the length of one coil.

Decreasing the volume of the MPG limits the value of the generated voltage as the values of N and L become small. The typical open-circuit voltage for 1 cm^3 was reported to be below 150 mV [2]. As a result, EM MPGs need to step-up the output voltage before rectification using transformers or voltage doublers. Transformers at the small scale are characterized by low efficiency due to the high core losses. In addition, the requirement of

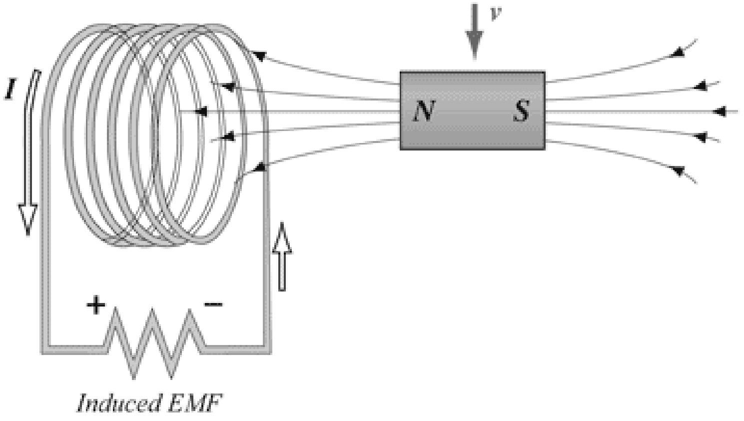

Figure 2.3: Principle of operation of electromagnetic MPGs.

a high magnetic field requires a strong permanent magnetic whose implementation is not compatible with current MEMS processes.

On the other hand, EM MPGs have some advantages over other MPGs. They do not require an initial source because they rely on a permanent magnet as a source of magnetic flux. The mechanical part of the EM MPGs can be easily designed without the need for mechanical contact, which improves its reliability and reduces its mechanical damping. In addition, the existing literature in AC generators gives a boost to the effort of designing and implementing commercial vibrational MPGs.

Different authors [21, 28, 31] have reviewed the existing EM MPGs. Several attempts to implement an electromagnetic micro-generator were demonstrated both on the micro and macro sizes. One of the earliest implementations is that of Williams et al. [9]. A micro-size electromagnetic generator was designed and fabricated. A rare-earth magnet was assembled to provide the needed magnetic field. Figure 2.4 shows a schematic of the cross-section of the generator. The size of the generator is 5 mm × 5 mm × 1 mm and it generates 0.3 μW from a 4 MHz excitation input. Such a high vibration frequency as well as the use of an external magnet reduce the usability of these generators for real applications.

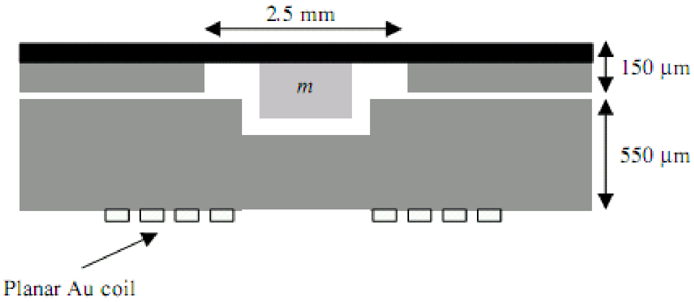

Figure 2.4: Cross-section of the electromagnetic MPG proposed by Williams et al. [9].

Figure 2.5: Commercial Perpetuum EM energy harvester [10].

As an example of commercial EM MPGs, Perpetuum Ltd [10] has developed a series of vibration-powered electromagnetic generators, which cover a broad range of vibration frequencies. Power outputs of up to 5 mW at an acceleration of 0.1 m/s^2 have been demonstrated and their devices, shown in Figure 2.5, have been used to power sensors and commercial wireless modules.

Examination of the literature on MPGs shows that EM MPGs have been a hot topic in research over the last few years because of the well-established operating principles of AC generators. Moreover, macro-scale EM MPGs have demonstrated the generation of mWs output power enough to power commercial wireless modules. However, scaling down the size of EM MPGs produces small output voltages below the rectifying diodes cut-in voltage. As a result, additional transformer or voltage doublers circuits are needed.

2.5 Electrostatic Energy Harvesters

Many similarities in the theory of operation exist between electromagnetic and electrostatic generators. In electrostatic generators, mechanical energy is stored in an electric field in contrast to electromagnetic generators in which it is stored in a magnetic field for. Moreover, an energy storage device is present in both cases. In electromagnetic generators, the inductance of a coil stores the magnetic field while a capacitor stores the electric field in electrostatic generators.

Electrostatic generators are older than electromagnetic generators. The first primitive electrostatic generator was invented in 1663 by Otto von Guericke. Since that time, several electrostatic machines have been demonstrated. The method of generation in these machines varies between friction, charge induction and variable capacitor techniques [32].

Electrostatic generation machines can be classified into two groups: three-element machines and two-element machines. In three-element machines, a charge induction element causes a charge to be produced and deposited on a transporting element. This transporter can be an insulating belt, a disc, a gas, or an oil or water droplet. By allowing the motion of this charged transporter away from the induction source, the potential of the charges is raised until the charges are collected by the other terminal. These machines are also called fixed-capacitance or charge-transporter machines. An example of these machines is the Van de Graaff belt-type machine [33].

However, this group of electrostatic machines is suitable for large-scale machines only. For efficient operation of these machines, a sufficient charge production and a long transportation distance to raise the potential are required. These conditions are not suitable for micro-power generation on the small-scale and can lead to electric discharge in the air or breakdown of the dielectric.

The two-elements machine is simply a variable capacitor that varies cyclically between minimum and maximum values. This type of machines is characterized by higher efficiency and power density compared to the first type. Besides, two-element machines are based on variable capacitors, which can be implemented on the small-scale for micro-power generation.

To illustrate the concept, we can write the electrical power stored in a capacitor with variable capacitance and electric field as

$$\begin{aligned} P &= vi = v\frac{dq}{dt} \\ &= v\frac{d(cv)}{dt} \\ &= cv\frac{dv}{dt} + v^2\frac{dc}{dt} \end{aligned} \tag{2.4}$$

The first term in (2.4) represents the power stored in the electric field due to an applied electric source, while the second term represents additional contribution to the power due to the change in the capacitance with time. Therefore, by changing the capacitance with time, we can change the amount of power stored in the charged capacitor. In short, allowing vibrations to change the capacitance value of a charged capacitor will change the amount of stored energy inside the capacitor.

The main advantages of the electrostatic generator are the compatibility with the backbone of MEMS technology as well as the possible integration with electronic circuits. Unlike electromagnetic generators, electrostatic generators produce a satisfactory voltage suitable for electronic circuits that will be attached for power conditioning. On the other hand, electrostatic generators suffer from a main operational limitation. They require an initial source of electrical energy in order to start the conversion.

Comparing the three transduction mechanism, we noted that the main limitation facing both piezoelectric and electromagnetic generators is the use of special materials (i.e., ceramic materials and magnets). These materials place a limitation towards MPGs integration with ICs technology. These problems can be solved only on the process level through improving or inventing processes that allow the development of these generators as well as the integration of external electronics. On the other hand, the short comings of electrostatic MPGs are operational and not problems in the fabrication processes. In other words, with a better design of the transducer as well as finding alternatives for the initial energy source, the performance of electrostatic generators can be improved without the use of special costly processes.

In the next section, classification of electrostatic MPGs according to their charging mechanism is presented with a discussion on the existing implementations.

2.5.1 Switched Electrostatic Micro-Power Generators

In this type, the capacitive transducer is charged at the maximum capacitance instance and then either the charge or the voltage on the capacitor is constrained during the free flight of the movable electrode. The charge is drained from the capacitor when the minimum capacitance position is reached. This charging cycle is called conversion cycle and occurs every vibration period.

Figure 2.6 shows the Q–V plot of the capacitive transducer during energy conversion using charge-constrained and voltage-constrained operation. The amount of generated energy is the area enclosed by the curve. Increasing the amount of generated energy requires increasing the capacitance of the transducer and the tuning range of the capacitor and a proper control of the switching times.

As a result, power electronics circuits are present in this type of ES MPGs to perform three main functions: extracting power from the generator, returning some of the energy back to the generator in order to initiate the next conversion cycle, and regulating the

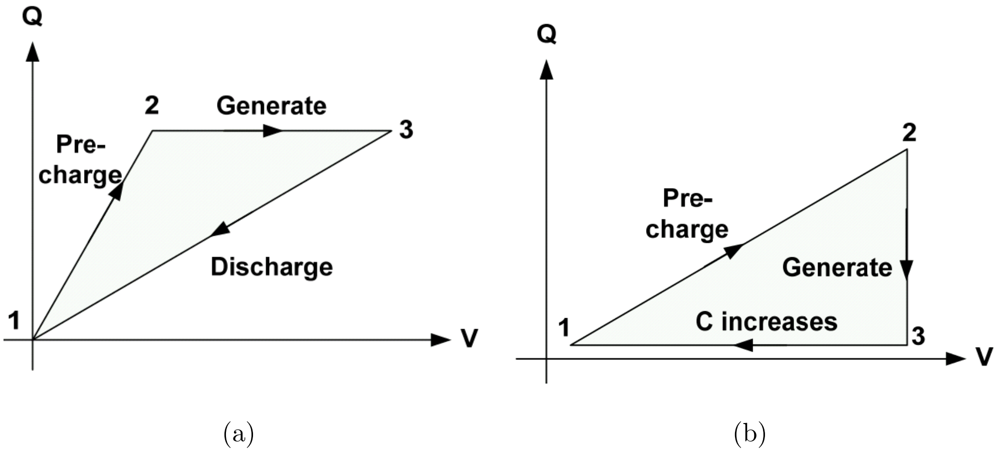

(a) (b)

Figure 2.6: Switched electrostatic MPG's conversion cycle: (a) charge-constrained, and (b) voltage-constrained.

output in order to deliver a constant voltage to the load. Although the wording "power electronics" is confusing because the generator is dealing with power in the μW to mW range, it is still valid because of the presence of relatively high voltage and high current during switching. Moreover, control circuits are needed to control the operation of the generator by controlling the timing of the switches used in the power electronics circuits. A functional block diagram for switched electrostatic MPGs is illustrated in Figure 2.7.

In the block diagram shown in Figure 2.7, we have distinguished among the transducer, energy harvester, and the micro-power generator blocks. The capacitive transducer block is the variable capacitor. The energy harvester includes beside the variable capacitor, a mechanical oscillator with the capacitor's movable electrode attached to the inertial mass of the oscillator. The micro-power generator includes the power electronics and control circuits, the energy harvester, and the charging source.

Different switched ES MPGs have been proposed in the literature. In fact, the first electrostatic MPG was of the switched-type. The first electrostatic micro-generator system was proposed in [11, 34]. A schematic of the micro-generator is shown in Figure 2.8 in

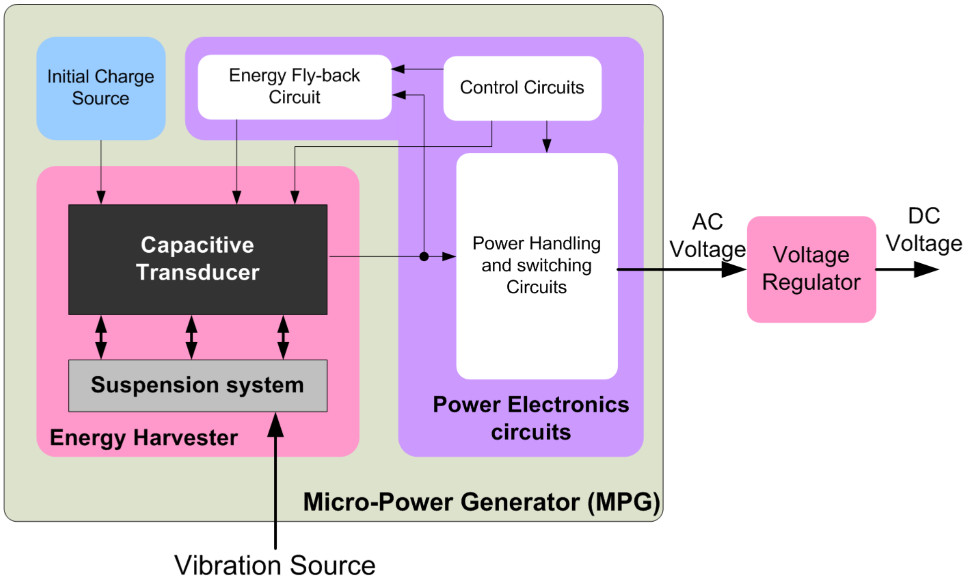

Figure 2.7: Traditional electrostatic micro-power generator block diagram.

which the size of the proposed transducer is 1.5 cm × 0.5 cm without including the spring. A comb-like structure with overlap variation topology was used to build the transducer. The thickness of the device is 500 μm. The finger length was 512 μ with a width of 7 μm and a gap of 7 μm. The capacitance of this device varies between 2 pF and 260 pF. The device is capable of two conversion cycles per vibration cycle, thereby doubling the amount of harvested power. The amount of harvested power is predicted to be 8.66 μW from a vibration source of frequency 2520 Hz and an acceleration equal to 0.196 m/s^2 (2% of the gravitational acceleration). This device was only proposed but not fabricated. Subsequently, the fabrication steps and structure of the transducer were further developed in [3]. However, the device failed to be fabricated due to the stringent dimensions/requirement for the fingers and the gap between them.

Tashiro et al. [12] presented a macro-size ES MPG in which a honey-comb-type variable capacitor with a capacitance variation of 32 – 200 nF was used to convert mechanical energy into electrical energy. A sketch of how the capacitance varies is shown in Figure 2.9.

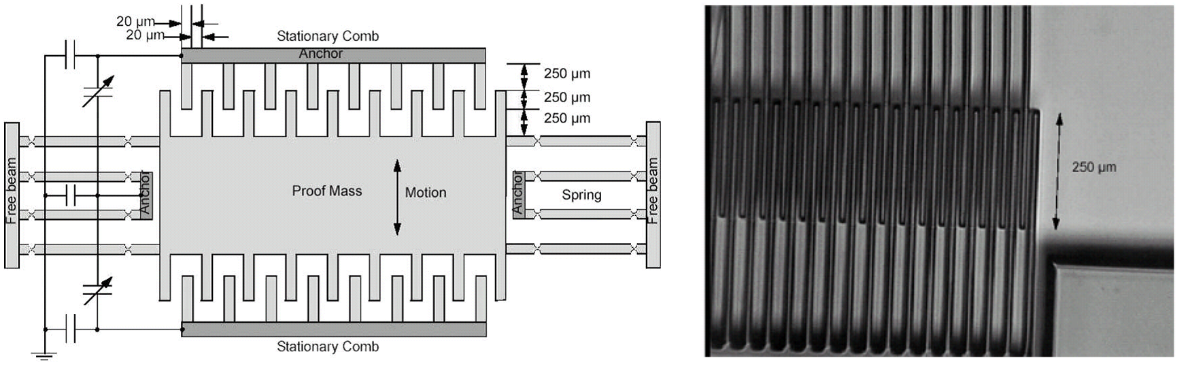

(a) (b)

Figure 2.8: Meninger et al.'s electrostatic MPG: (a) schematic, and (b) SEM picture [11].

The capacitance is changed by changing the gap between honeycomb-type structures. An output of 58 mW was reported for this generator using a 24 V charging source and a load of 1 MΩ. The device weighs 0.64 kg.

In 2002, Roundy et al. presented a transducer that is capable of producing a predicted power of 54 μW using a comb-finger structure with a gap variation topology [2]. The device has a nominal gap separation of 530 μm, a finger length of 50 μm, a 0.25 μm minimum gap, and a device thickness of 200 μm. A vibration source of amplitude 2.25 m/s^2 at 120 Hz was used to power the micro-generator. The authors proved the concept of operation using a macro-scale generator. The device was based on out-of-plane gap closing topologies. It produced an output power of 0.1 nW for a 3 V source and about 1 nW for a 9 V source with an operating vibration frequency of 100 Hz. Three prototypes using different MEMS fabrication processes and sizes were fabricated. However, the devices failed to operate due to problems in the fabrication processes, integration of the diodes, the high electric resistivity of the electrodes, and the stringent dimensions of the fingers.

A working out-of-plane cantilever-based MPG was presented by Miyazaki et al. [13]. A picture of the generator is shown in Figure 2.10. The MPG has a base capacitance of 1 nF and a variable capacitance of between 30 pF and 350 pF. The device resonated at

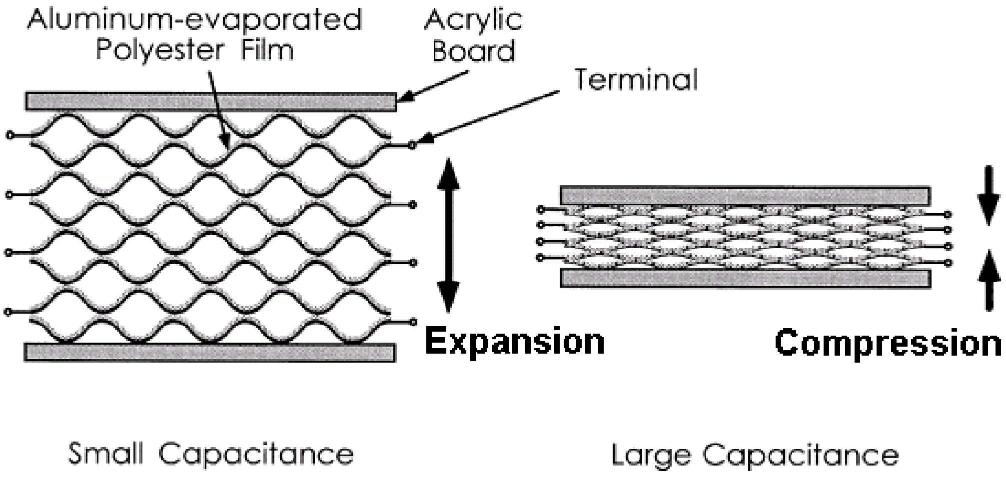

Figure 2.9: Capacitance variation in Tashiro et al.'s ES MPG [12].

45 Hz. The device was tested on a wall with a 1 μm displacement up to 100 Hz. A power of 120 nW was harvested for a wall acceleration of 0.08 m/s^2.

Despesse [35] reported on an electrostatic MPG with a wide bandwidth(<100 Hz). He used an in-plane gap-closing transducer operating in the charge-constrained mode to achieve high electrical damping. A fabricated macroscale bulk tungsten structure, with a volume of 18 cm^3, delivered 1.05 mW at 50 Hz and 1 g acceleration, with an inertial mass of 104 gm. Another silicon microstructure of volume 81 mm^2 $\times$ 0.4 mm with a 2 gm inertial mass excited by a vibration amplitude of 95 μm at 50 Hz is predicted to produce a scavenged power of 70 μW.

An electrostatic generator with a transducer topology based on out-of-plane parallel plate transducer was presented in [14]. The cross-section of the transducer is shown in Figure 2.11(a). The capacitor was a hybrid integrated device. The generator is a mesoscale generator. It is 28 mm × 28 mm × 2 mm. It had a considerably large gold inertial mass. The mass of the moving plate of the capacitor is estimated from the dimensions on the schematic to be about 2.5 gm. The inertial mass is suspended using a highly flexible

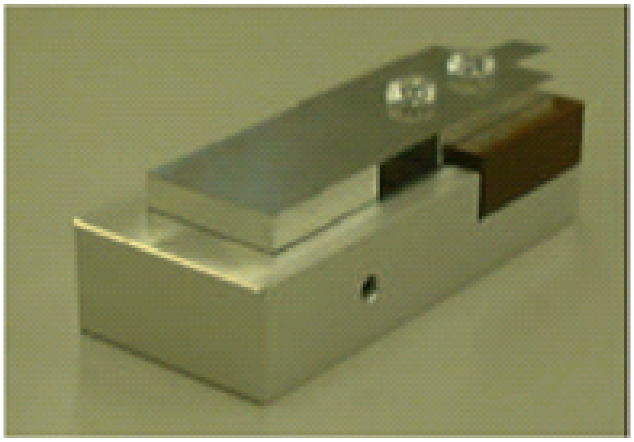

Figure 2.10: Picture of the capacitor proposed in [13].

polyimide membrane. Metal is deposited on the fixed plate as well as the moving plate to insure good contact. The capacitance variation of this structure was estimated between 1 pF and 100 pF. The transducer was driven using a 26 V voltage source and the output voltage reached 2.3 kV. This large output voltage makes integrating the transducer with integrated electronics difficult. The amount of power generated from this device based on the charging and discharging of the charges was calculated to be 24 μW at a vibration frequency of 10 Hz.

Based on this energy harvester, a non-resonant MPGs was presented by Mitcheson et al. [15]. The new MPG is called “the Coulomb-force-parametric generator (CFPG)”. The CFPG is inherently a nonlinear mechanical device where it uses a very low stiffness suspension to eliminate the dependance on the natural frequency. The device was fabricated using a three-wafer construction. The central wafer contains a silicon inertial mass, forming one plate of the variable capacitor, along with a silicon frame and a polyimide suspension metallized for electrical contact. Polyimide is chosen to give a very low suspension stiffness. The bottom wafer is glass to minimize parasitic capacitance. Charging and discharging are through studs with which the moving mass makes contact at the ends of its travel, resulting

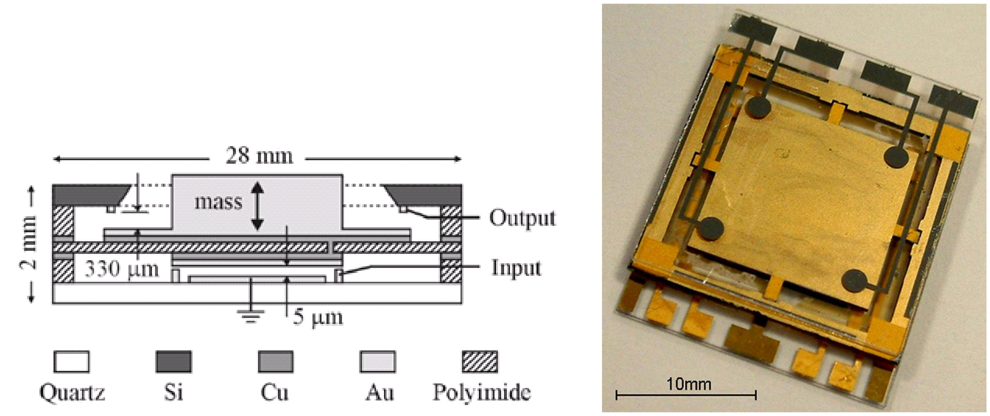

(a) (b)

Figure 2.11: CFPG electrostatic MPG [14, 15]: (a) device's cross section and (b) MPG picture.

in self-synchronous operation. Figure 2.11(b) shows a picture of the complete device. The measured output energy was 120 nJ per cycle at 30 Hz, with a source acceleration of 10 m/s^2.

2.5.2 Switchless Electrostatic Micro-Power Generators

Switchless or continuous ES MPG relies on operating the capacitive transducer charged all the time. The system dynamic will change both the voltage and charge on the capacitor as vibration occurs, leading to a net energy generation. The Q–V curves of this type of MPGs is presented in details in Section 3.2. The operation in this case is neither charge nor voltage constrained.

Figure 2.12 shows the functional block diagram of the switchless type MPG. The power electronics and control circuits used for charging and discharging control are eliminated. As a result, the energy consumed in those circuits is eliminated, resulting in a simpler structure with higher conversion efficiency.

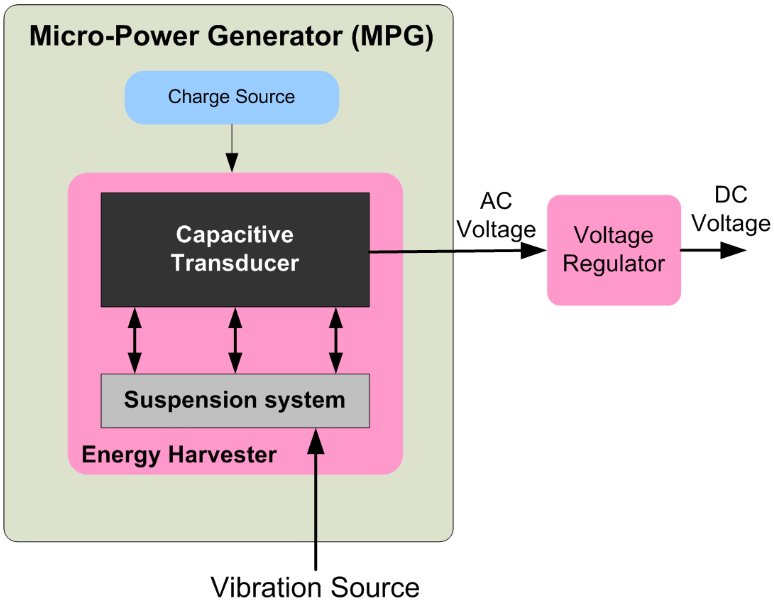

Figure 2.12: Switchless electrostatic micro-power generator block diagram.

The charging sources can be either an external DC voltage or a layer of electret, which is used to induce charges on the electrodes of the capacitive transducer. The electret acts similar to a magnet. A magnet is a body that possess long-lasting magnetism. Similarly, an electret is a body that possess long-lasting electrization or polarization. In other words, an electret is a dielectric material that exhibits a quasi-permanent electrical charge. The term ”quasi permanent” means that, if the electret layer is properly handled, it can retain its charge for years. Such materials are widely used in microphones. More information about the history and nature of electrets can be found in [32, 36].

Significant efforts have been devoted to developing electret-based electrostatic MPGs in the last five years. Boland et al. [16] miniaturized an electret-based electrostatic generator proposed by Tada [37]. The fabricated MPG shown in Figure 2.13 had a rotor diameter of 8 mm and an output power of 25 μW at 4170 RPM.

Tsutsumino et al. [17, 38] developed the electric subsystem of an electrostatic MPG using electret-based interdigitated parallel-plate capacitors. The moving electrode of the

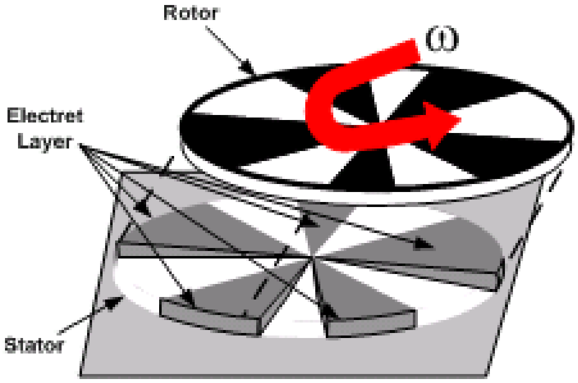

Figure 2.13: Rotary electrostatic MPG [16].

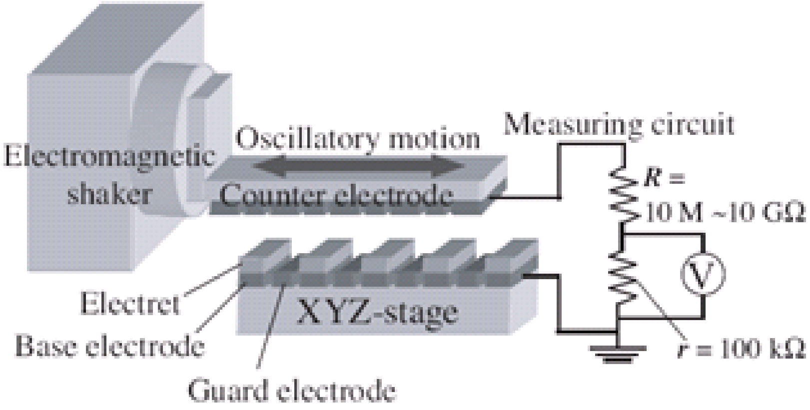

Figure 2.14: 3D schematic of Tsutsumino et al.'s electric subsystem [17].

variable capacitor was attached to a shaker to move it parallel to the fixed electrode as shown in Figure 2.14. Using rectangular electrodes, 10×20 mm^2, they realized maximum output power of 278 μW. Later, they modified their design to divide the variable capacitor into two out-of-phase capacitors and found that this architecture improves the power extraction capacity of the MPG and transforms the electric damping force from Coulomb-like to viscous [38, 39].

Edamoto et al. [18] constructed a fully functioning MPG, Figure 2.15, by combining

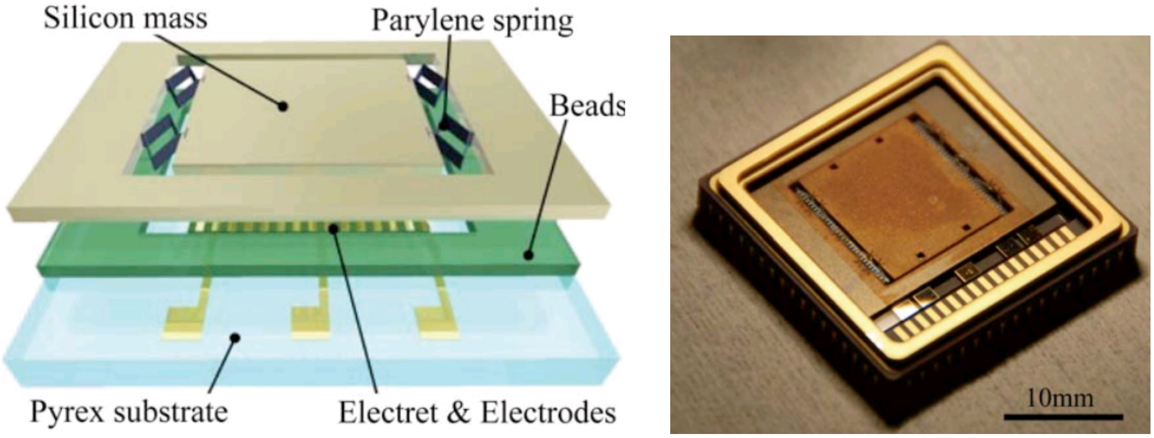

(a) (b)

Figure 2.15: Electret-based interdigitated parallel plate electrostatic MPG [18] (a) 3D schematic of the MPG, (b) Packaged MPG picture.

this electric subsystem with a mechanical subsystem. The movable electrodes were attached to an inertial mass suspended from soft parylene springs to create a low-frequency resonator [40]. They also used two electret layers to induce levitation forces in the movable electrodes, thereby protecting against pull-in [41]. The simulated output power was 12.5 μW, but it dropped in experimental measurements to 0.28 μW due to misalignment between the electrodes of the variable capacitor [42].

Naruse et al. [19] used interdigitated capacitive electrodes with a microball bearing suspension [43] to develop low-frequency electret-based electrostatic MPGs. The microball bearing suspension, shown in Figure 2.16, allowed the use of compliant springs, while keeping a firm separation gap. The MPG used an electret layer formed using a new technique that made the electret's surface voltage reaches up to 800V with the use of silicon oxide as an electret material. The dimensions of the device are 20 mm×45 mm. The fabricated MPG produced 20 μW output power from a vibration source of frequency 2 Hz and an acceleration amplitude equals to 0.4 g. The comb-finger capacitive transducer

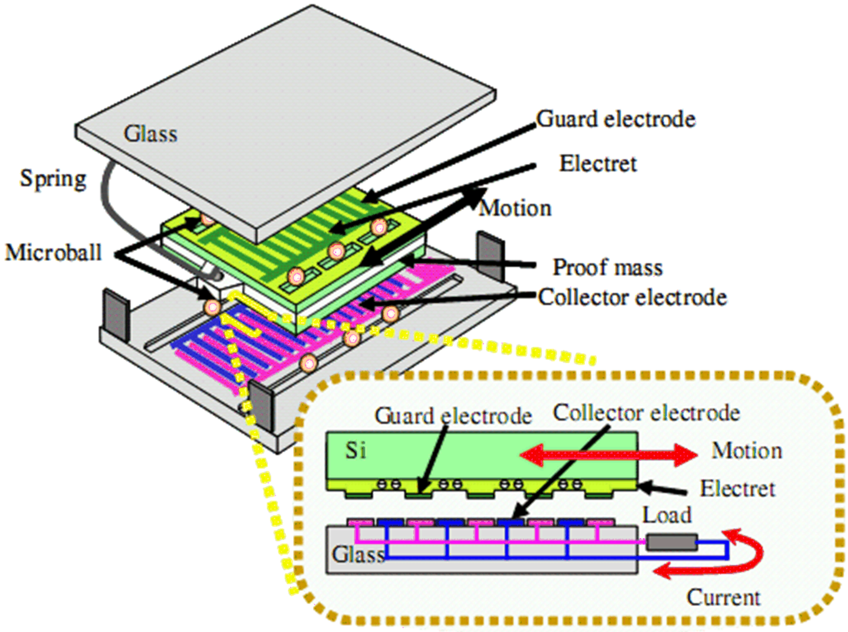

Figure 2.16: New structure of Naurse at al.'s MPG supported with microball bearings [19].

is employed in electrostatic MPGs in several implementations. Sterken et al. [20] proposed and fabricated a rectilinear electret-based electrostatic MPG using comb-finger variable capacitors and a predicted output power of 50μW. Bartsch et al. [44] fabricated two MPG prototypes based on Sterken et al.'s topology: a meso-sized prototype (59 mm × 86 mm) and a micro-sized prototype (3 mm × 6 mm) with output powers of 0.36 μW and 1.4 nW, respectively, [6].

2.6 Discussions and Summary

From the above survey, it is difficult to compare the performance of different reported generators based on the output power density only. Two reasons are behind these difficulties. The first reason is the wide variation in the vibration sources, which has a direct impact on the amount of output power generated because it is equal to the product of the output energy and the operating frequency, which in most cases is the vibration frequency. Moreover, the smaller the vibration frequency is, the larger the inertial mass is, resulting in larger generator volume which affects the energy density.

The second reason is that some of the published works report the movable electrode displacement without mentioning the vibration displacement, which makes it difficult to normalizes the output power with respect to the input vibration power. Moreover, one of the generators was of the rotational type, which makes it even more difficult to compare its performance with respect to others.

As a result, rather than using the output power or energy density as the only measure of performance,other operating parameters need to be considered. Some of these parameters are:

- **Frequency of operation**

  The operating frequency of an electrostatic generators is limited by the frequency of the vibrating source. The reason behind this is to achieve maximum displacement of the movable electrode by working at the natural frequency of the mechanical structure of the transducer. However, for low-frequency vibration sources, it is very difficult to match the natural frequency of the device to the vibration frequency because this requires a large inertial mass. The direct impact of the low frequency of the excitation source is to have larger volume and lower output power, which are unavoidable using current implementations.

- **Electrostatic MPG types**

  The use of electret layer in switchless ES MPGs as a source of charge induction seems to be the best solution for several reasons. The first reason is the possibility of integrating it within the generator without the need of assembly or special processes. The second reason is the possibility of using SiO_2 and Si_2N_3 interface for trapping charges to act like an electret [45]. The third reason is the elimination of the power electronics circuitry needed to pass energy between the capacitor and the energy source to sustain the conversion process. The presence of such circuits complicates the design, increases the power losses in the conversion cycle, and decreases the resulting output power. However, the drawback of switchless ES MPGs is the need of a large resistive load (in the range of 10 MΩ to 100 MΩ) to work efficiently.

- **The design of the transducer**

  The two main structures proposed in the published work are either a comb-finger or a parallel plate structure. Although the comb-finger structure can achieve a large capacitance variation and is easy to operate compared to the limitation in parallel plate capacitors (pull-in problem, stiction, . . .etc), they fail in most of the cases. The reason behind this is that implementing large capacitance requires a large number of fingers with large aspect ratio as well as small gap operation, which make fabrication of the device more difficult as well as costly because of the need for a high-aspect ratio bulk micro machining fabrication facility.

  Moreover, due to the large size of the comb-structure transducer, a comparable distributed resistance appears across the transducer due to the limited conductivity of polysilicon. Such resistance may cause the transducer operation to fail [2]. As a result, most of the reported literature using comb-like structures failed to fabricate or operate the actual designs; instead, they were forced to fabricate reduced size transducers, which affect both the operation and the expected output power.

  On the other hand, parallel plate structure can achieve large capacitance values using more planar technology and using metallic electrodes to minimize the effect of shunt distributed resistance. In addition, it is possible to include intermediate layers, such as electrets or high dielectric materials, to elevate the performance and reduce the size. In conclusion, a parallel plate structure suits more the requirements of electrostatic MPGs.

According to the aforementioned discussion, switchless (continuous) electrostatic MPGs using electret is a suitable implementation for portable and lifetime operation. This MPGs type eliminates the power electronics and control circuits needed in the conversion process. However, current implementations of switchless electrostatic MPGs suffer from limitation according to their topology and the operating frequency. Therefore, improved structures are needed to enhance the performance of switchless electrostatic micro-generators as well as the easiness of implementation.

Chapter 3

Out-of-plane Switchless Micro-Power Generators

3.1 Introduction

In this chapter, the theory of Switchless (continuous) MPGs is developed. In-plane and out-of-plane transducers for switchless energy generation are presented with special focus on their energy harvesting capacities. A system model of the out-of-plane transducer is derived and validated using a macro prototype. The experimental results of the prototype are compared with the model results showing good agreement.

Practical implementation of the MPG by embedding an electret film within the transducer is presented. The experimental results demonstrate the energy harvesting capability of this type of MPGs. Moreover, the results show the occurrence of impacts and their role in obtaining wideband energy harvesting. A comprehensive model is developed that takes into account the impact process. Finally, an improved version of the MPG prototype is presented. The MPG achieves high energy generation, low vibration amplitude and wideband operation.

3.2 Switchless Energy Harvesters

Consider the circuit shown in Figure 3.1. The circuit consists of a DC voltage source V_{dc}, a variable capacitor C_v, and a load resistance R. When C_v is held constant, the steady-state voltage drop across the capacitor is equal to the source voltage, leaving no current through or voltage drop across the resistance. On the other hand, if C_v is allowed to vary over time, an AC voltage drop V_{ac} develops across the capacitor and a similar and opposite-polarity voltage drop develops across the resistor.

There is no power dissipation in the voltage source because its voltage is held constant while the current passing through it is AC. On the other hand, the root mean square of the electrical power delivered to the load is

$$P_e = R\,(I_{ac})^2_{rms}$$

where I_{ac} is the current passing through the load. Therefore, net power generation is achieved. The circuit in Figure 3.1 is used to generate electrical energy out of vibrations by allowing those vibrations to vary the capacitance C_v.

The electrical model of the transducer in Figure 3.1 can be derived by applying Kirch-

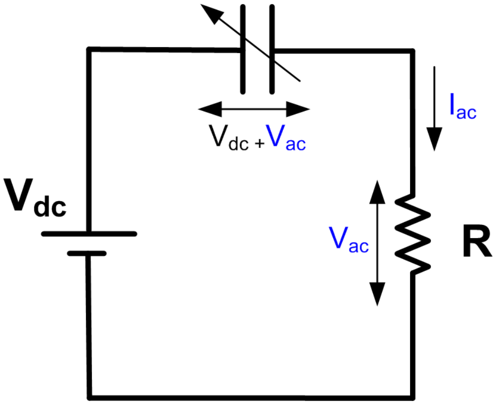

Figure 3.1: A circuit diagram for switchless (continuous) energy harvesting.

hoff's voltage law to the circuit, the resulting differential equation is

$$\begin{aligned} V_{dc} &= V_C(t) + I(t)R \\ &= \frac{q(t)}{C_v(t)} + \dot{q}(t)R \end{aligned} \tag{3.1}$$

where $q(t)$ is the charge stored in the capacitor $C_v(t)$, $V_C(t)$ is the voltage across the same capacitor, and $\dot{q}(t)$ is the current passing through the resistance R. Implementation of variable capacitors can be of either the in-plane or out-of-plane type. The relative motion between the electrodes of in-plane variable capacitors, like the overlap comb-finger capacitor shown in Figure 3.2, occurs in the plane of one or both electrodes. The relative motion between the electrodes of out-of-plane variable capacitors, like the parallel plate capacitor shown in Figure 3.3, is perpendicular to their planes.

The capacitance of the in-plane overlap comb-finger capacitor is

$$C_v = C_\circ\Big(1 - \frac{x(t)}{h_\circ}\Big) \tag{3.2}$$

where $C_\circ$ is the nominal capacitance at a nominal finger length, $h_\circ$, while $x(t)$ is the displacement of the movable electrode. The capacitance of out-of-plane parallel plate capacitors is

$$C_v = \frac{C_\circ}{\big(1 - x(t)/g_\circ\big)} \tag{3.3}$$

where $C_\circ$ is the nominal capacitance at a nominal gap, $g_\circ$, between the electrodes while $x(t)$ is the displacement of the movable electrode. Using (3.2) in (3.1), the electrical model of the in-plane comb-finger transducer can be written as

$$\dot{q} = \frac{V_{dc}}{R} - q\Big[\frac{1}{RC_\circ\big(1 - x/h_\circ\big)}\Big] \tag{3.4}$$

Similarly using (3.3) in (3.1), the electrical model of the out-of-plane implementation can be written as

$$\dot{q} = \frac{V_{dc}}{R} - q\Big[\frac{\big(1 - x/g_\circ\big)}{RC_\circ}\Big] \tag{3.5}$$

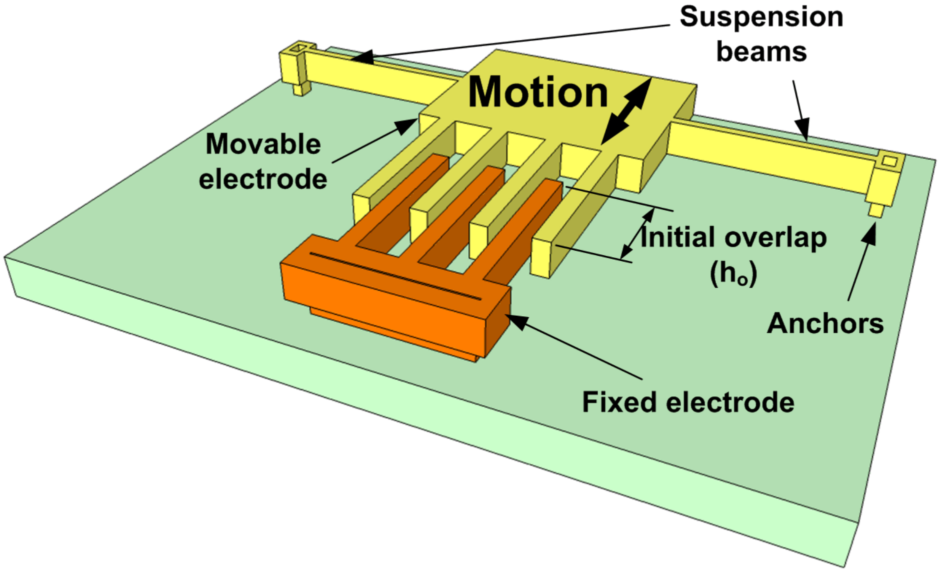

Figure 3.2: A schematic of an in-plane variable capacitor.

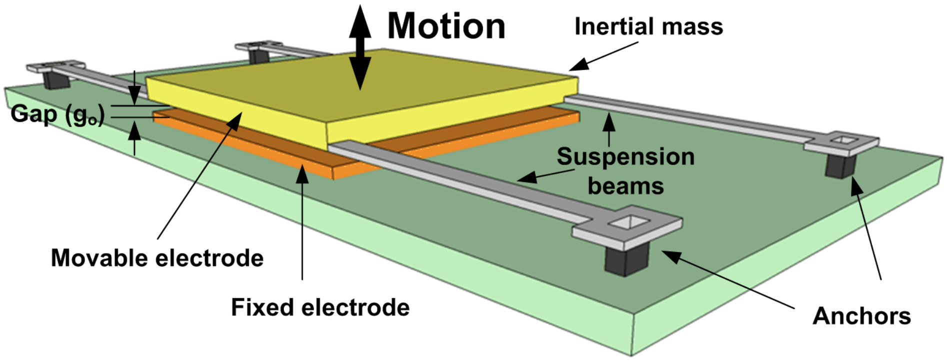

Figure 3.3: A schematic of an out-of-plane variable capacitor.

The choice of a suitable transducer for vibration energy harvesters requires a method to estimate the energy harvesting capacity. The area enclosed by the Q–V curve can be used to determine the amount of electrical energy harvested per conversion cycle. Assuming a sinusoidally moving electrode such that

$$x(t) = x_\circ \sin(\Omega t + \gamma) \tag{3.6}$$

where $x_\circ$, Ω, and γ are the amplitude, frequency, and phase angle of the displacement of the moving electrode, respectively, the resulting Q–V curves for the in-plane and out-of-plane cases are shown in Figures 3.4 and 3.5 for the same amplitude of electrode displacement normalized with respect to $h_\circ$ and $g_\circ$, respectively. The plotted voltage and charge are normalized with respect to V_{dc} and $C_\circ V_{dc}$, respectively. As a result, the harvested energy is equal to the area enclosed by the loci times $C_\circ V_{dc}^2$; the magnitude of electric energy injected into the system initially.

Comparing the two figures, it is clear that, due the singularity in the out-of-plane capacitor as $x_\circ \to g_\circ$, the amount of harvested electrical energy per conversion cycle is much more than that of the in-plane capacitor for the same normalized stroke when the motion becomes comparable to the gap. Moreover, although the in-plane electrode displacement is normalized with respect to the finger length $h_\circ$, which enables the use of larger finger lengths without decreasing the nominal capacitance $C_\circ$, structural instability places an upper bound on the maximum realizable comb-finger length. From this discussion, it is clear that out-of-plane transducers have a good potential as switchless micro-power generators compared to conventional in-plane transducers.

The amount of harvested energy depends on the size of the movable electrode motions $x(t)$. The motion of the movable electrode does not depend only on the external excitation but also on its coupling with the electrical harvesting transducer. Therefore, it is important to study the integrated system dynamics to correctly estimate the harvested energy. In the next section, a complete system model of the out-of-plane energy harvester will be presented.

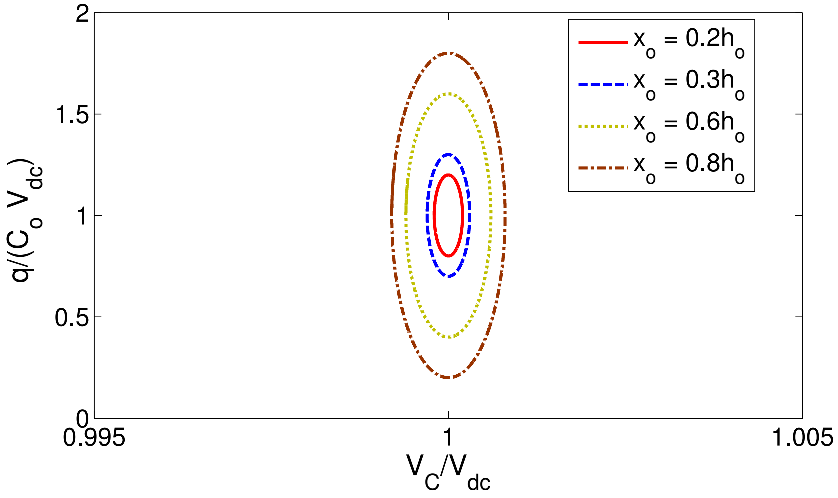

Figure 3.4: Q–V curves for the in-plane transducer for different electrode displacement amplitudes.

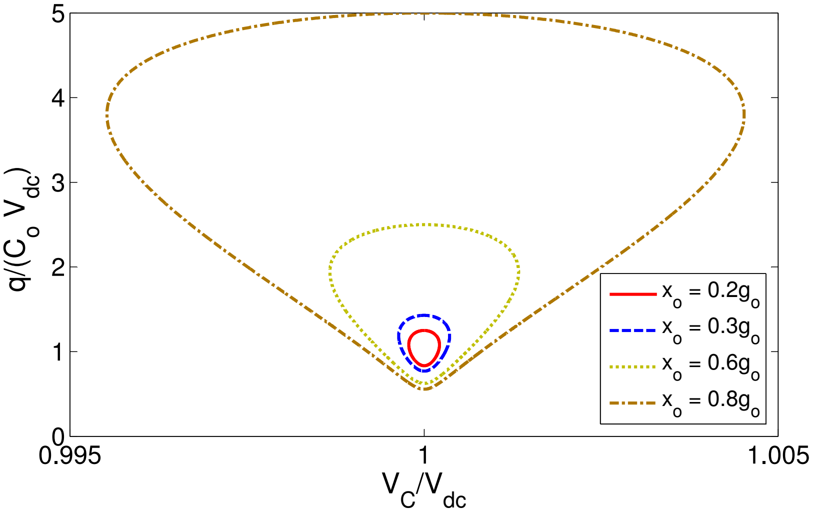

Figure 3.5: Q–V curves for the out-of-plane transducer for different electrode displacement amplitudes.

3.3 System Model

To study the system dynamics, we augmented the electrical model of the transducer with a model to describe the capture of kinetic energy. Typical vibration-energy harvesters capture base excitations, as shown schematically in Figure 3.6 [46]. Base excitations move the frame with a displacement $y(t)$. A spring exerts a force F_s on an inertial mass, m, attached to one of the capacitor's electrodes, to keep it suspended inside the frame. The relative displacement of the mass with respect to the frame is x. The electrostatic field exerts a force F_e to attract the moving electrode to the fixed electrode while a damper opposes the motion of the mass with a damping force F_d. Using the relative displacement as state variable, the equation of motion of the system can be written as

$$m\ddot{x} = F_e - F_s - F_d - ma_y(t) \tag{3.7}$$

where $a_y(t) = \ddot{y} = A_\circ \cos(\Omega t)$ is the base acceleration and $A_\circ$ is the amplitude of base acceleration. The electrostatic force between the electrodes is obtained by differentiating the energy stored in the capacitor with respect to the movable electrode displacement.

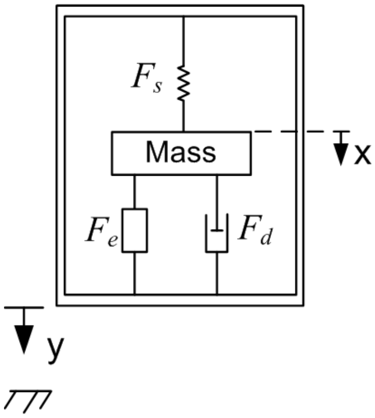

Figure 3.6: Mechanical model of a vibration energy harvester.

Therefore, the electrostatic force of the out-of-plane capacitors is

$$F_e = \frac{q^2}{2g_\circ C_\circ} \tag{3.8}$$

Using (3.8) in (3.7), a linear spring force F_s, and a viscous damping force F_d, we write the equation of motion as

$$m\ddot{x} = \frac{q^2}{2g_\circ C_\circ} - k_1 x - c_m \dot{x} - mA_\circ \cos(\Omega t) \tag{3.9}$$

where k_1 is the linear spring constant and c_m is the mechanical damping coefficient, which can be written as

$$c_m = c_l + c_{sq} \tag{3.10}$$

where c_{sq} accounts for squeeze-film damping and c_l accounts for damping due to other sources. Squeeze-film damping depends on the gap between the electrodes and, therefore, constitutes a nonlinearity in the equation of motion. Following Fedder [47], the squeeze-film coefficient is represented by

$$c_{sq} = \frac{3}{2\pi} \frac{\mu A^2}{(g_\circ - x)^3} \tag{3.11}$$

where μ, A, and $g_\circ$ are the coefficient of viscosity of air, the electrodes surface area, and the nominal gap between the electrodes, respectively.

Substituting (3.10) and (3.11) into (3.9) and using (3.5), we find that the system dynamics are described by the differential equations

$$\begin{aligned} \dot{q} &= \frac{V_{dc}}{R} - q\left[\frac{\big(1 - x/g_\circ\big)}{RC_\circ}\right] \\ m\ddot{x} &= \frac{q^2}{2g_\circ C_\circ} - k_1 x - \left(c_l + \frac{3}{2\pi}\frac{\mu A^2}{(g_\circ - x)^3}\right)\dot{x} - mA_\circ \cos(\Omega t) \end{aligned} \tag{3.12}$$

The quantities

$$\omega_m = \sqrt{\frac{k_1}{m}} \quad , \quad \zeta_l = \frac{c_l}{2\sqrt{k_1 m}} \tag{3.13}$$

are then introduced into (3.12) to represent the mechanical natural frequency ω_m and the damping ratio ζ_l, respectively. As a result, the system differential equations become

$$
\begin{aligned}
\dot{q} &= -\frac{q}{RC_\circ}\big(1-\frac{x}{g_\circ}\big)+\frac{V_{dc}}{R} \\
\ddot{x} &= \frac{q^2}{2mg_\circ C_\circ}-\omega_m^2 x-\Big(2\zeta_l\omega_m+\frac{3}{2\pi}\frac{\mu A^2}{m(g_\circ-x)^3}\Big)\dot{x}-A_\circ\cos(\Omega t)
\end{aligned}
\tag{3.14}
$$

This is a system of nonlinear coupled differential equations in the state variables q and x representing a lumped-mass model of the energy harvester in free-flight. It does not account for the possibility of the inertial mass coming into contact with the fixed electrode which will be addressed using a separate model. In the next section, model validation will be carried out by comparing the numerical solution of (3.14) with the experimental results obtained from testing an out-of-plane implementation of the energy harvester.

3.4 Model Validation

The prototype used to demonstrate the out-of-plane electrostatic energy harvester was fabricated using precision machining. Figure 3.7 shows a picture of the electrostatic harvester prototype. Its dimensions are (9 mm × 2 mm × 1.8 mm). It consists of a bottom fixed electrode and an upper movable electrode attached to the anchors using four guided aluminum beams. The anchors are fixed to the base using screws. The gap between the electrodes is varied by inserting shims between the anchors and the base to obtain the corresponding gap. The inertial mass is made of a steel rectangular cube attached on top of the movable electrode. Table 3.1 summarizes the prototype dimensions.

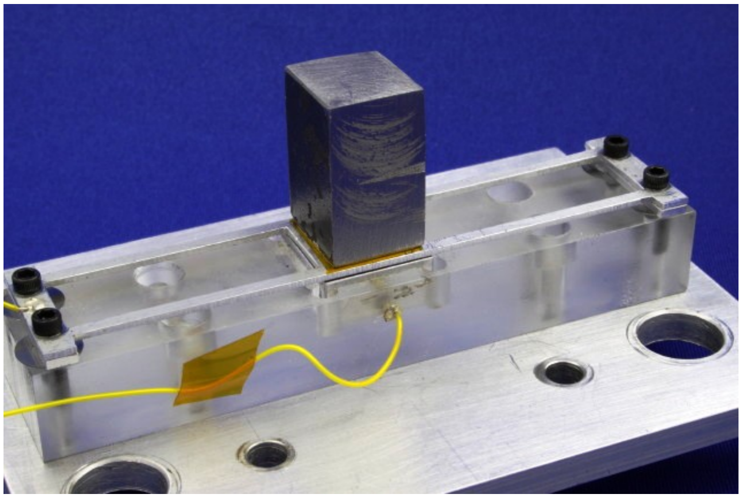

Figure 3.7: Picture of the electrostatic energy harvester prototype.

The linear spring constant of the guided beams can be estimated using the formula [47]

$$k_1 = nE\frac{bh^3}{L^3} \tag{3.15}$$

where n, E, b, h, and L are the number, Young's modulus, width, thickness, and length of the beams, respectively. We used the beam dimensions listed in Table 3.1 into (3.15) to calculate $k_1 = 13361$ N/m. The natural frequency was calculated using (3.13) and the inertial mass m_1 from Table 3.1 as $\omega_b = 673$ rad/s or $f_b = 107$ Hz.

To account for the non-idealized geometry and configuration of the beams, nonlinear finite element analysis (FEA) was carried out on the prototype using the COMSOL software

Table 3.1: Summary of the electrostatic harvester prototype dimensions.

Plate length	15 mm	Plate width	15 mm
Beam length	32 mm	Beam width	2 mm
Beam thickness	0.9 mm	m_1	29.5 gm

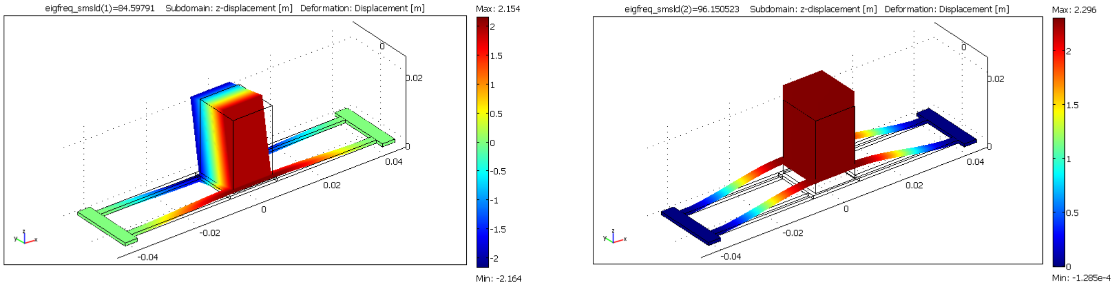

(a) (b)

Figure 3.8: The (a) first (b) second mode shapes of the prototype.

package. The linear spring constant was then extracted from the relationship between the static force and the displacement to be 10987 N/m. The first and second mode shapes of the harvester prototype, shown in Figure 3.8, were also found using COMSOL. The first mode is a torsional mode. It appears at $f_t = 84.6$ Hz. The second mode is a bending mode. It appears at $f_b = 96.1$ Hz. The bending mode is used for energy harvesting, therefore the effective mass of the energy harvester was calculated from the second mode natural frequency and the linear spring constant using (3.13) as $m = 30.1$ gm.

A schematic of the experimental setup is shown in Figure 3.9. The prototype was placed on the base of a pneumatic shaker which is used to supply base excitations. The prototype was connected electrically to a DC power supply, primary load resistor, and test resistor. The test resistor R_{test} was used in series with the load resistor R_{load} to prevent the loading effect of the signal analyzer input impedance. The signal analyzer measures the root mean square (RMS) of the output voltage across the test resistor.

The load resistance is composed of primary and test resistances of 1 MΩ and 100 kΩ, respectively. The gap between the electrodes was initially set to a nominal value of 250 μm, the DC power supply to 300 V, and load resistance to $R = 1.1$ MΩ. The frequency-response curve of the RMS output voltage was obtained by sweeping the frequency of

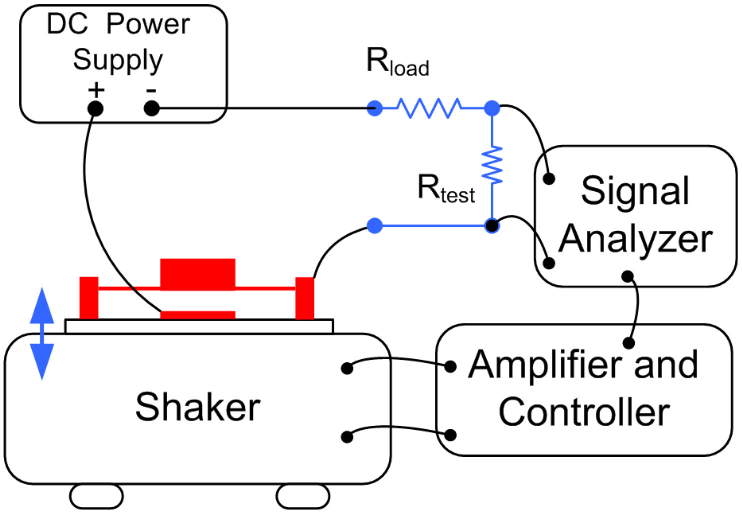

Figure 3.9: The experimental setup of the energy harvester prototype.

base accelerations between 70 Hz and 100 Hz while holding the amplitude constant at $A_\circ = 0.04\,g$ (RMS). Two peaks are observed in the frequency-response curve, Figure 3.10, at $f_t = 81.41$ Hz and $f_b = 94.1$ Hz. The first peak corresponds to the torsional mode while the second peak corresponds to the bending mode. The voltage level of the torsional mode is much smaller than that of the bending mode since torsional motions of the movable electrode do not produce as much variation in the capacitance as up-and-down motions of the bending mode.

The lower natural frequencies obtained experimentally, compared to those obtained with FEA, are due to support flexibility (anchors, screws, and base) unaccounted for in the FE model. Using the effective mass calculated from FEA and the natural frequency of the second mode obtained experimentally, the linear spring constant was adjusted using (3.13) to be $k_1 = 10480$ N/m.

In order to compare the experimental results with the model, the actual gap $g_\circ$ and the damping coefficients need to be estimated. The actual gap differs from the nominal gap by the amount of static deflection that occurs because of settling under the weight of the

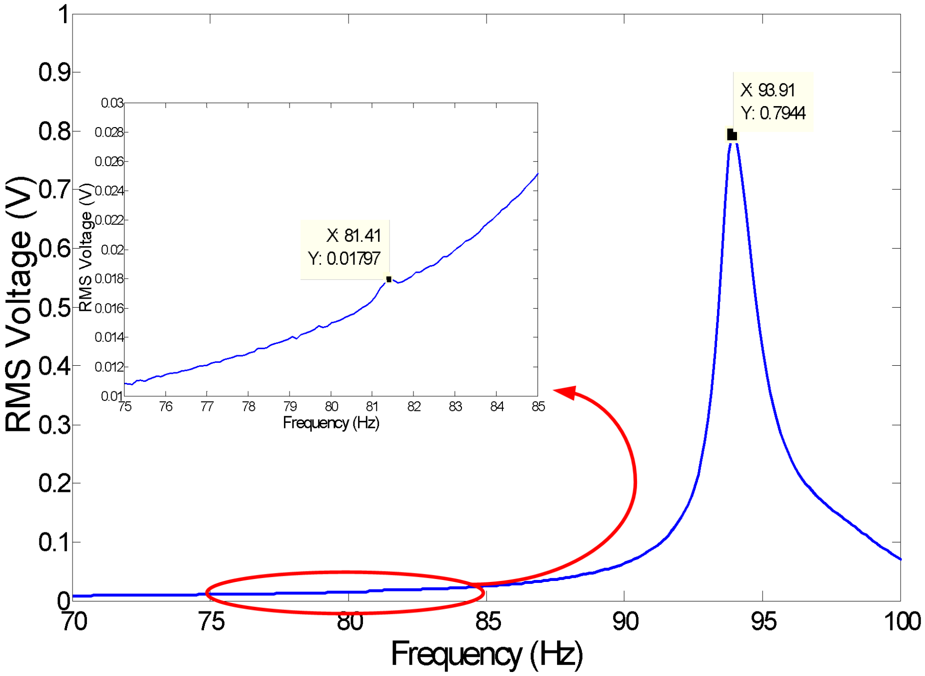

Figure 3.10: RMS of the output voltage obtained experimentally from a frequency sweep of base acceleration at an amplitude of $0.04\,g$ (RMS).

inertial mass. The static deflection is evaluated as

$$x_{static} = \frac{mg}{k_1} \tag{3.16}$$

where g is the acceleration of gravity. The static deflection of the prototype was calculated as 25 μm, therefore, $g_\circ = 225\,\mu$m.

The total damping ratio can be extracted from the experimental results using the half power bandwidth BW and the natural frequency $f_\circ$ using

$$\zeta_m = \frac{BW}{2f_\circ} \tag{3.17}$$

Using the results in Figure 3.10, it was found that $\zeta_m = 0.006$. A parameter estimation procedure was developed to estimate ζ_l based on the fact that squeeze-film damping is minimal for electrode motions away from the fixed electrode. The procedure used the frequency-response curve corresponding to the lowest excitation amplitude available in the data set in this case, the curve corresponding to a base acceleration of $A_\circ = 0.02\,g$(RMS). The total damping coefficient ζ_m was then used as an initial guess for the linear damping coefficient $\zeta_l^i = \zeta_m$. The energy harvester model (3.14) was integrated numerically for the output voltage at resonance and the value of the linear damping coefficient was reduced until the values of the numerical and experimental RMS output voltages match.

Using this procedure, we found the value of the linear damping coefficient to be $\zeta_l = 0.0057$. Figure 3.11 compares the frequency-response curves of the RMS output voltage for base acceleration amplitudes of $A_\circ = 0.02\,g$, $0.03\,g$, $0.035\,g$, and $0.04\,g$(RMS). The curves shown in solid lines were obtained experimentally, while the curves shown in dotted lines were obtained by integrating (3.14) for the parameters estimated above. The results show good qualitative and quantitative agreement between the model and experiment for all four excitation levels.

Finally, the Q–V curve was found experimentally and predicted using the model in (3.14) at the natural frequency of the bending mode $f_b = 94.1$ Hz. The experimental voltage across the variable capacitor was obtained as the difference between the measured supply and load voltages. The charge on the variable capacitor was obtained by integrating the current measured passing through the load. The constant of integration was estimated by shifting the experimental Q–V curve along the Q-axis to fit within the Q–V curve obtained by numerical integration of the model (3.14). Figure 3.12 shows the experimental and numerical Q–V curves for a base acceleration amplitude of $A_\circ = 0.04\,g$ (RMS). The areas enclosed by the two curves are close to each other. The experimental results were moved up along the Q-axis by adding a constant of integration $Q_\circ = 0.72\,C_\circ V_{dc}$. This value correspond to the charge available on the variable capacitor at equilibrium (in the absence of motion).

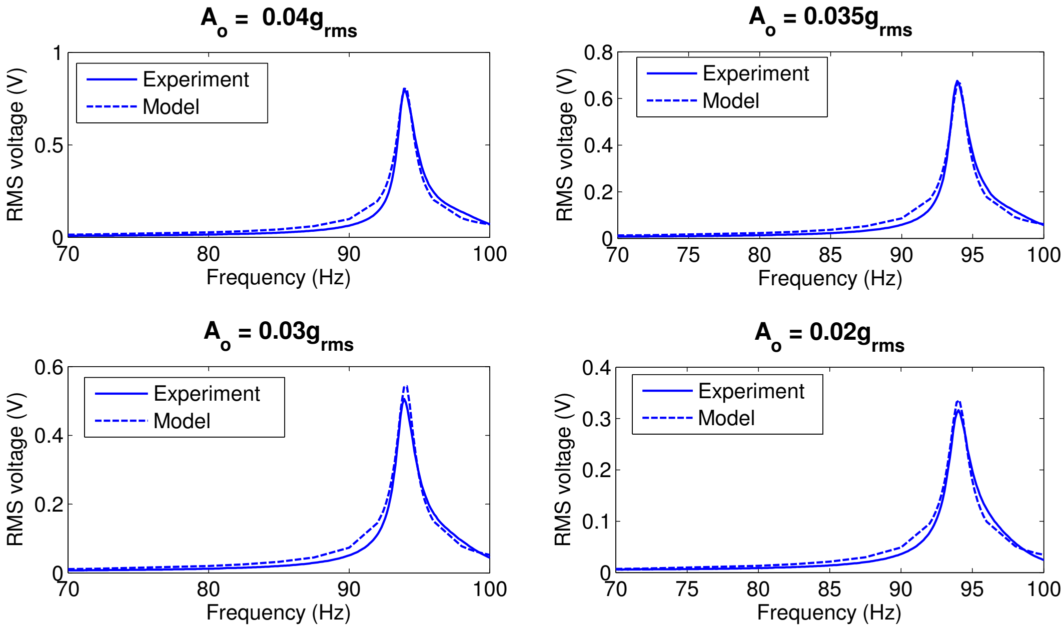

Figure 3.11: The frequency-response curves of the RMS output voltage at four base acceleration amplitudes obtained experimentally (solid lines) and numerically (dotted lines).

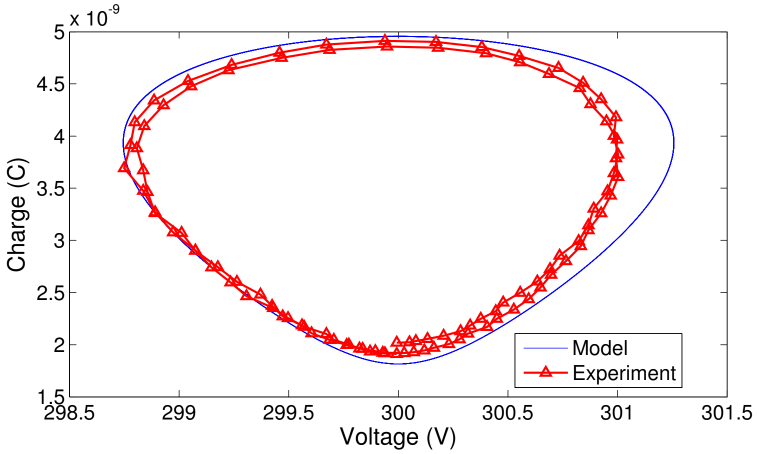

Figure 3.12: Q–V curves for the energy harvester prototype at $A_\circ = 0.04\,g$ (RMS) and $R = 1.1$ MΩ.

The experiment and model predications presented in this section show good agreement, indicating the validity of the model developed in the previous section to describe switchless out-of-plane energy harvesters. In the next section, a practical implementation of an electrostatic micro-power generator (MPG) based on this energy harvester will be introduced and studied.

3.5 MPG Realization

Realization of a practical electrostatic energy harvester requires the substitution of the DC voltage source with a portable charging source. A charged dielectric embedded within the structure of the transducer will be used to induce charges on the capacitor electrodes. A permanently charged dielectric, an electret [36], constitutes an attractive option to satisfy this requirement since it facilitates sustainable operation over several years. Ready-made electrets are used here as a low cost solution to provide V_{dc} that avoids extra fabricating and charging steps.

An electret film was integrated into the energy harvester prototype introduced in Section 3.4 to constitute an Electret-MPG prototype. Figure 3.13 shows an extended 3D schematic of the Electret-MPG prototype where the electret layer is attached to the top surface of the fixed electrode using conductive double-sided copper tape. The electret layer was fashioned from a negatively charged PTFE Teflon sheet (Radelec Inc.). It has a thickness of 50 μm and the surface voltage was measured at $V_{dc} = -410$ V.

Figure 3.14 shows a picture of the assembled MPG prototype. The MPG prototype is identical to the energy harvester prototype except that the inertial mass is initially made of a shorter copper block with $m_2 = 17.5$ gm, resulting in an effective mass of $m = 20.4$ gm. The reduced rotary inertia of the new mass increases the natural frequency of the torsional mode so that it exceeds the natural frequency of the bending mode. FE analysis produced the natural frequency of the bending mode at $f_b = 121$ Hz and the natural frequency of the torsional mode at $f_t = 170$ Hz. The test setup of the MPG prototype, Figure 3.15, is also similar to that of the energy harvester prototype except that the external DC power

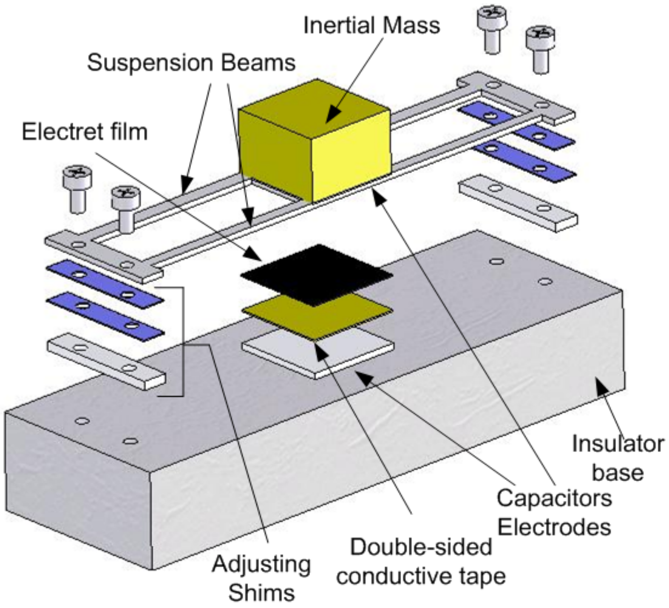

Figure 3.13: Extended 3D schematic of the electret-MPG prototype.

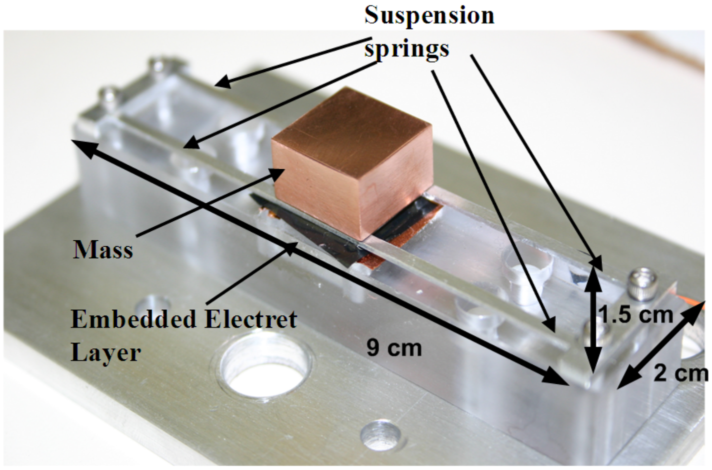

Figure 3.14: Picture of the electret MPG prototype.

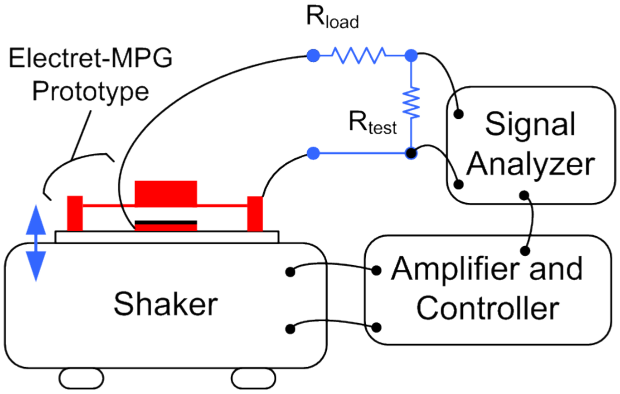

Figure 3.15: The test setup for the electret MPG prototype.

source is eliminated.

The nominal capacitor gap was initially set equal to $g_{\circ 1} = 300\,\mu$m by inserting shims under the anchors. The frequency-response of the system is obtained by sweeping the frequency of the base acceleration while maintaining the amplitude constant. The frequency was swept up and down over the whole frequency range $[110, 124]$ Hz to detect the presence of hysteresis in the system response. Figure 3.16 shows the frequency-response curves of the RMS output voltage for different vibration base acceleration amplitudes of $A_\circ = 0.15\,g$, $0.2\,g$, $0.3\,g$, $0.4g$, and $0.5\,g$ (RMS).

The frequency-response curves in Figure 3.16 show three distinct regions of behavior: linear, soft impact, and hard impact. Linear response is seen at low acceleration amplitudes ($A_\circ = 0.15\,g$) and is characterized by a frequency-response curve centered around the natural frequency of the bending mode $f_b = 116$ Hz. Similar to the case of the energy harvester, the natural frequency obtained experimentally is lower than that obtained with FEA because of the un-modeled effect of support compliance.

Soft impact is seen at an acceleration amplitude of $A_\circ = 0.2\,g$ where the peak of the frequency-response curve appears wider than that of the linear response due to the dominance of the nonlinear damping mechanism, squeeze-film, for large motions (near

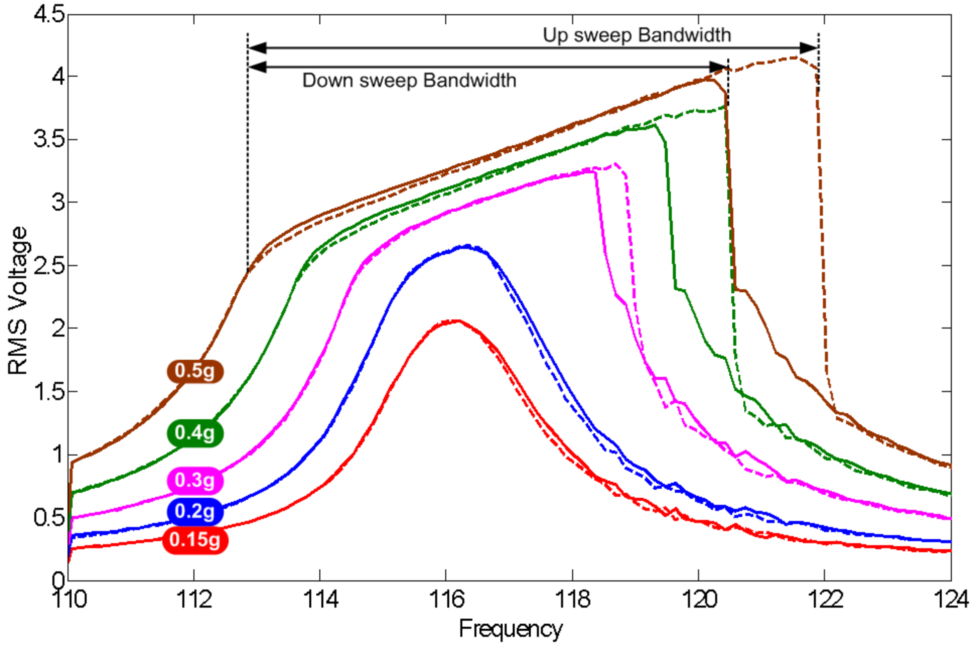

Figure 3.16: Frequency-response curves of the RMS output voltage for inertial mass m_2, gap, $g_{\circ 1} = 300\mu$m, and base acceleration amplitudes in the range $A_\circ = 0.15 - 0.5\,g$ (RMS). Frequency up-sweeps are shown in dashed lines and down-sweeps as shown in solid lines.

resonance) as the moving plate approaches the electret layer. Hard impact responses are seen for base acceleration amplitudes $A_\circ \geq 0.25\,g$. The onset of hard impact is marked by a “knee”, an abrupt change in the curvature of the frequency-response curve.

Defining the MPG bandwidth as the half-power bandwidth for the linear response and the distance between the response knees for soft and hard impact, we observe the following:

- The MPG bandwidth increases as the amplitude of base acceleration increases and the response region changes from linear to soft impact to hard impact
- The up-sweep and down-sweep bandwidths are equal for linear and soft impact, while the up-sweep bandwidth is wider than the down-sweep bandwidth for hard impact, as reported by Soliman et al. [48].

Specifically, Figure 3.16 shows that the MPG bandwidth increases from 2 Hz for the linear response to 9 Hz for hard impact and a base acceleration amplitude of $A_\circ = 0.5\,g$. These results facilitate the use of electrostatic MPGs under hard impact to design wideband MPGs [49] that can harvest more energy by increasing the fraction of time during which random environmental vibrations fall within the MPG bandwidth.

To test the effect of variation in the electrostatic field strength on the MPG performance, we repeated the experiment shown in Figure 3.16 using the MPG prototype with nominal capacitor gaps of $g_{\circ 2} = 425\,\mu$m and $g_{\circ 3} = 750\,\mu$m. The results for the three gap distances are summarized in Figures 3.17, 3.18 and 3.19. The figures show the MPG output power and bandwidth at the prototype's natural frequency $f_b = 116$ Hz in frequency up- and down-sweeps at a constant base acceleration amplitude.

The results show that the MPG output power and bandwidth depend on the interaction

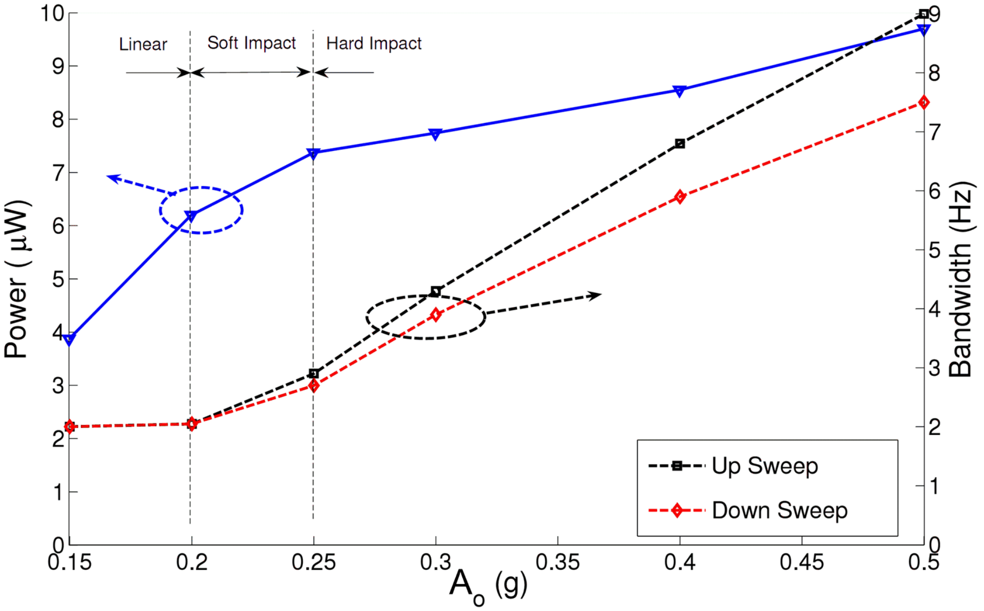

Figure 3.17: Output power and bandwidth of the MPG prototype as functions of the base acceleration amplitude at $g_{\circ 1} = 300\ \mu$m.

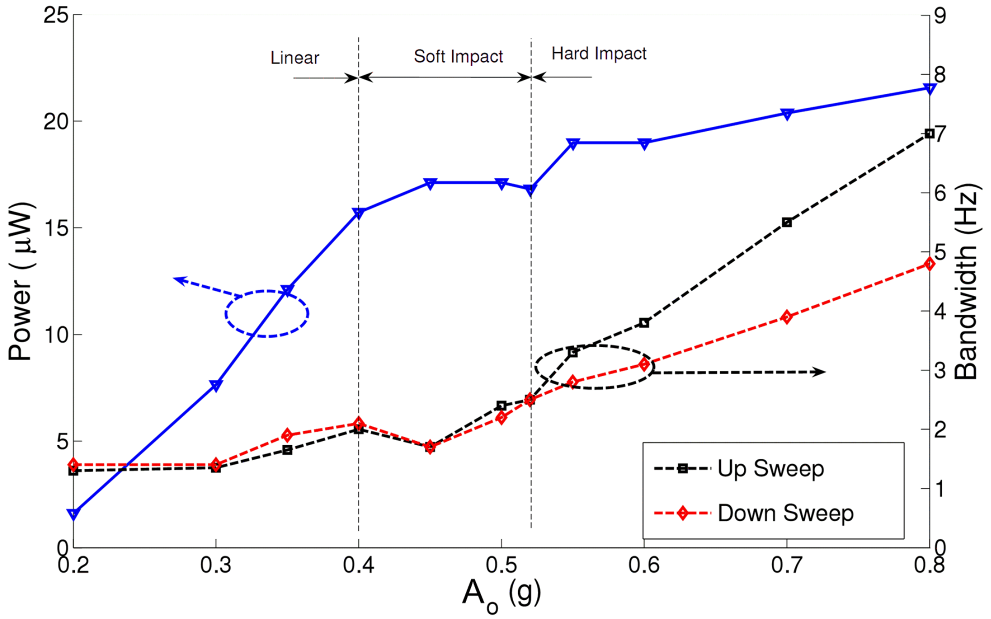

Figure 3.18: Output power and bandwidth of the MPG prototype as functions of the base acceleration amplitude at $g_{\circ 2} = 425\ \mu$m.

among three factors: the strength of the electrostatic field, squeeze-film damping, and hard impact. A small gap and, thus, a stronger electrostatic field for a given electret voltage, allow the MPG to extract more output power from lower excitation levels than MPGs with weaker electrostatic fields. This can be seen by comparing the output power of the MPG at $g_{\circ 1}$ to those at $g_{\circ 2}$ and $g_{\circ 3}$ at low base acceleration amplitudes $A_\circ \leq 0.2\,g$. The output power is more than 6 μW for $g_{\circ 1}$ and less than 10 nW for $g_{\circ 3}$ at a base acceleration amplitude of $A_\circ = 0.2\,g$. That is because the output power is proportional to the nominal capacitance $C_\circ$. Similarly, a smaller gap increases squeeze-film damping, even in the linear region, which increases the mechanical losses in the MPG. This can be seen in the larger bandwidth of the linear region for $g_{\circ 1}$, BW $= 2$ Hz, than those for $g_{\circ 2}$ and $g_{\circ 3}$.

A smaller gap leads to low impact losses since it means that impact will occur at a lower velocity. This can be seen in the figures by comparing the up-sweep bandwidth for $g_{\circ 1}$,

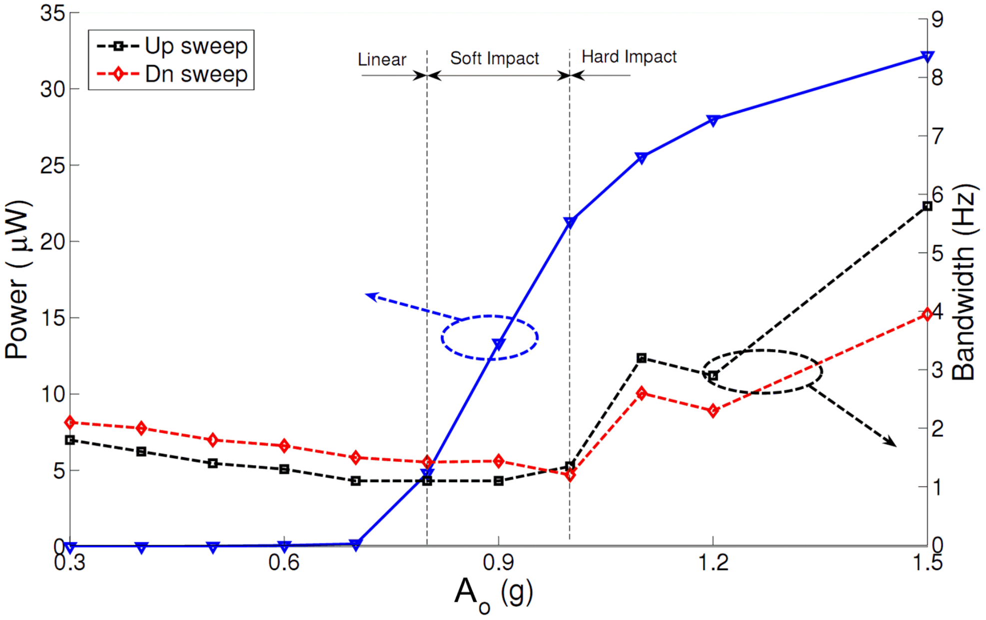

Figure 3.19: Output power and bandwidth of the MPG prototype as functions of the base acceleration amplitude at $g_{\circ 3} = 750\mu$m.

$BW = 9$ Hz at $A_\circ = 0.5\,g$, to that for $g_{\circ 3}$, $BW = 5.75$ Hz at $A_\circ = 1.5\,g$. Soliman et al. [49] show that the MPG up-sweep bandwidth is counter-proportional to impact losses. On the other hand, a larger gap allows for a longer stroke and a higher peak velocity, resulting in higher output power. This can be seen in the value at which the output power saturates with increasing base acceleration amplitude for the three gap distances. The output power saturates at 8 μW, 20 μW, and 30 μW for $g_{\circ 1}$, $g_{\circ 2}$, and $g_{\circ 3}$, respectively.

We conclude that it is crucial to balance these three factors in the design of out-of-plane electrostatic MPGs. The proper balance depends on the harvesting environment:

- For environments where small-amplitude vibrations are available, a small capacitor gap should be used to increase the strength of the electrostatic field and obtain higher nominal capacitance $C_\circ$ while maintaining the response in the linear region, thereby avoiding impact losses and increasing the efficiency of power extraction from low excitation amplitudes.

- For environments where large-amplitude vibrations are available in a narrow frequency band, a large capacitor gap combined with a strong electrostatic field generated by a large source voltage will lead to high efficiency energy extraction by maintaining the response near the linear response region while guaranteeing a larger output power saturation level by allowing for a larger stroke.
- For environments where large-amplitude vibrations are available in a wide frequency band, a large capacitor gap will lead to larger output power and wider MPG bandwidth by operating in the hard impact region.

3.6 Impact Model

Operating the MPG in the hard impact region creates a wideband MPG with up to 9 Hz in the up-sweep and 7 Hz in the down-sweep. Therefore, it is important to modify the model of the MPG to include the hard impact region, so that it can be used in performance prediction and optimization. In this section, a modified system model is developed and verified by comparison to experimental results.

Manual assembly of the electret on the bottom electrode creates bumps on the electret surface. To account for this, the electret film position was elevated by g_e, there by reducing the effective gap to g_i, as shown in Figure 3.20. Further, since the form of squeeze-film damping used in (3.11) has a singularity as $x \rightarrow g_\circ$, two viscous damping coefficients c_m and c_i were used to capture the dissipative processes during the free flight and impact phases of motion. The damping force is thus written as:

$$F_d = \begin{cases} c_m \dot{x} & x < g_i \\ c_i \dot{x} & x \geq g_i \end{cases} \tag{3.18}$$

The restoring force F_s is also re-defined to account for the impact phase of motion as follows:

$$F_s = \begin{cases} k_s x + k_3 x^3 & x < g_i \\ k_i x + (k_s - k_i) g_i + k_3 {g_i}^3 & x \geq g_i \end{cases} \tag{3.19}$$

where k_s and k_3 are the linear and cubic stiffness coefficients of the suspension beams and k_i is the stiffness coefficient of impact with the electret-covered bottom electrode.

Substituting (3.8), (3.19), and (3.18) into (3.7), we obtain a model for the MPG in the hard impact region composed of a system of two differential equations

$$\begin{aligned} \dot{q} &= -\frac{q}{RC_\circ}\left(1 - \frac{x}{g_\circ}\right) + \frac{V_{dc}}{R} \\ m\ddot{x} &= \begin{cases} \frac{1}{2}\frac{q^2}{C_\circ g_\circ} - k_s x + k_3 x^3 - c_m \dot{x} - m a_y & x < g_i \\ \frac{1}{2}\frac{q^2}{C_\circ g_\circ} - k_i x - (k_s - k_i) g_i - k_3 {g_i}^3 - c_i \dot{x} - m a_y & x \geq g_i \end{cases} \end{aligned} \tag{3.20}$$

Realization of the impact model requires estimation of the system parameters that appear in equations (3.20). The linear and cubic stiffness coefficients k_s and k_3 were extracted by fitting a third-order polynomial to the static force-deflection curve obtained from nonlinear FEA of the MPG with inertial mass m_2. The linear stiffness coefficient was then used in conjunction with the natural frequency of the bending mode obtained from FEA ($f_b = 121$ Hz) to extract the effective mass of the MPG ($m = 19.5$ gm). The linear stiffness coefficient was then decreased to match the natural frequency of the bending mode to the experimentally measured value, $f_b = 116$ Hz, thereby accounting for the compliance

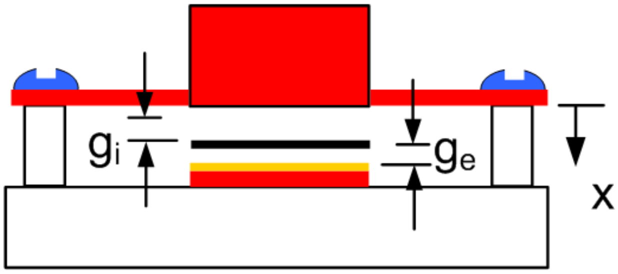

Figure 3.20: Cross-section of the MPG prototype.

in the supports. The damping coefficient of the free flight phase c_m was calculated from ζ_m obtained from the same experiment in (3.17) using the definition of the damping ratio

$$c_m = 2\zeta_m \sqrt{k_s m} \tag{3.21}$$

The effective gap $g_\circ$ was obtained by matching the RMS output voltage of the model to the output from the same experiment at a frequency away from resonance ($f = 110$ Hz).

The linear stiffness k_i of the contact spring was found by matching the slope of the frequency-response curve of the output voltage during impact at a base acceleration of $A_\circ = 0.5\,g$. The damping coefficient during impact c_i was found by matching the predicted and the experimental responses obtained in the up-sweep. The impact height g_i was estimated by matching the left knee in the frequency-response curve predicted by the model to that obtained from the same experiment. The estimated model parameters are listed in Table 3.2.

Figure 3.21 compares the frequency-response curves obtained from the impact model and the experiment in the up- and down -sweeps, respectively, of the MPG prototype with inertial mass m_2 and a gap $g_{\circ 1}$. The figure shows good agreement between model predictions and experimental results.

Table 3.2: Summary of the MPG impact model parameters.

k_s	10443 N/m	k_3	7.1×10^9 N/m
k_i	$8k_s$	$C_\circ$	8.1 pF
c_m	0.337 N.s/m	c_i	78 c_m
g_i	240 μm	$g_\circ$	295 μm

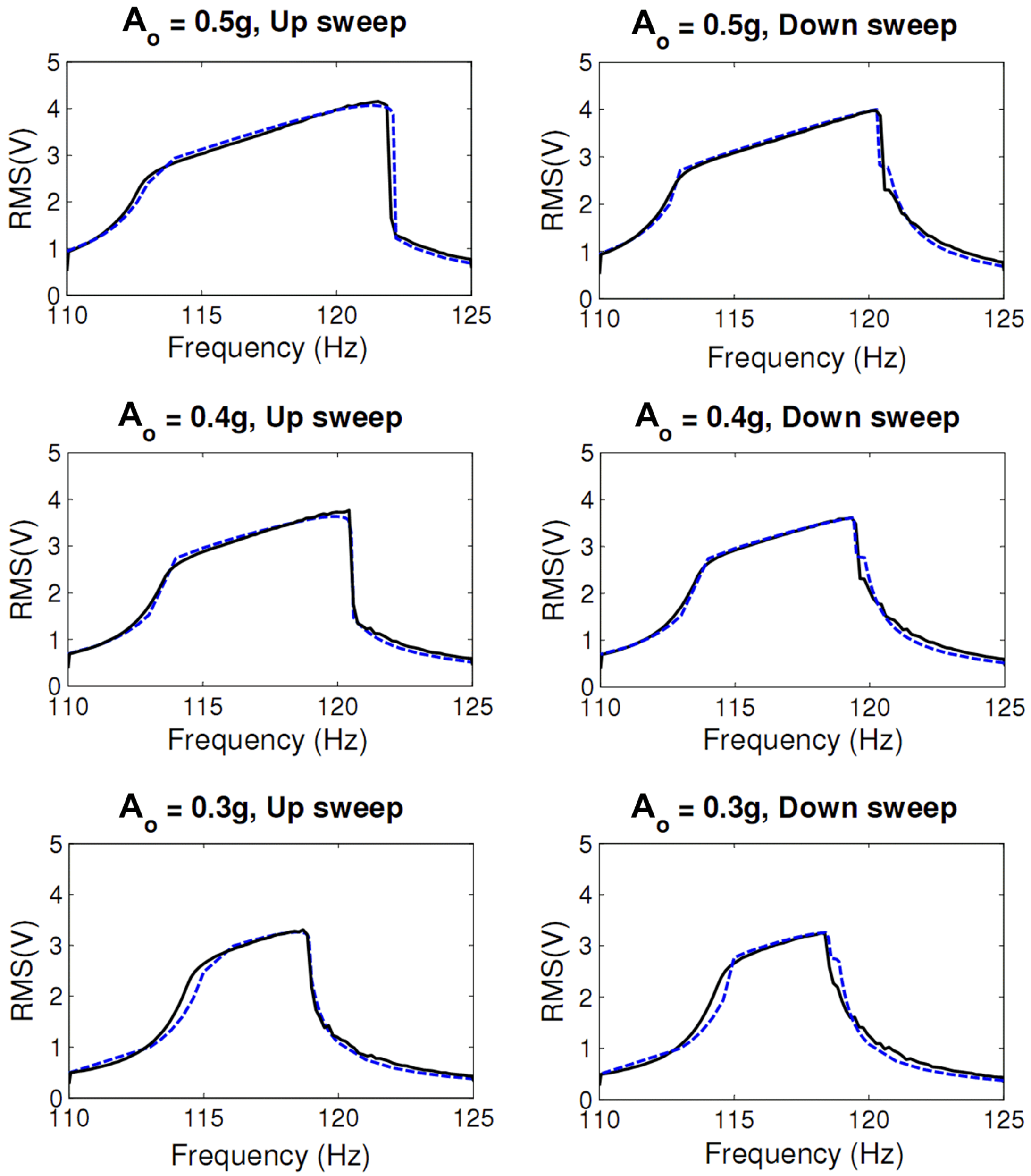

Figure 3.21: Frequency-response curves of the RMS output voltage obtained experimentally (solid lines) and predicted by the impact model (dotted lines) for frequency up-sweeps and down-sweeps of the MPG prototype with inertial mass m_2 and gap $g_{\circ 1}$.

3.7 Improved MPG

We examined the potential to design better MPGs that can capture more kinetic energy from the environment by testing the effect of stronger electrostatic fields and larger inertial mass. The strength of the electrostatic field was increased using a high-voltage electret at a gap similar to that in the previous experiment to minimize the effects of variation in squeeze-film damping and impact losses on the MPG performance. The surface voltage of the charged electret film was measured upon receipt from the manufacturer at -1700 V. At the time of the previous experiment, the surface voltage had degraded and was measured at -410 V. The surface voltage is known to drop in open air due to charge recombination under the influence of humidity [36]. For this experiment, we used an electret that was sealed from air until use in the experiment to preserve the charge within the electret. We also used the tall inertial mass $m_1 = 29.5$ gm. The nominal gap after installing the fresh electret is $g_{o4} = 275\,\mu$m.

Figure 3.22 shows the frequency-response of the RMS output voltage using the fresh electret, the tall inertial mass m_1, and base acceleration amplitudes in the range $A_\circ = 0.05{-}0.2\,g$ (RMS). Comparing Figure 3.22 to Figure 3.16, it can be seen that a higher source voltage and a larger inertial mass increase the output voltage by an order-of-magnitude for the same input base acceleration. They also result in the hard impact region starting at lower excitation levels ($\leq$ 0.1g), thereby producing a wider MPG bandwidth even for low environmental vibration amplitudes. We note that the higher rotary inertia of the tall mass m_1 shifts the natural frequency of the torsional mode $f_t = 76$ Hz below the natural frequency of the bending mode $f_b = 86$ Hz. This configuration has a detrimental effect on the MPG performance in the hard impact region. This can be seen in the initial drop in the output voltage beyond the left "knee" of the frequency-response curve instead of the the gradual increase observed in Figure 3.16. In this initial region, impact couples the closely-spaced bending and torsional modes, thereby channeling some of the kinetic energy

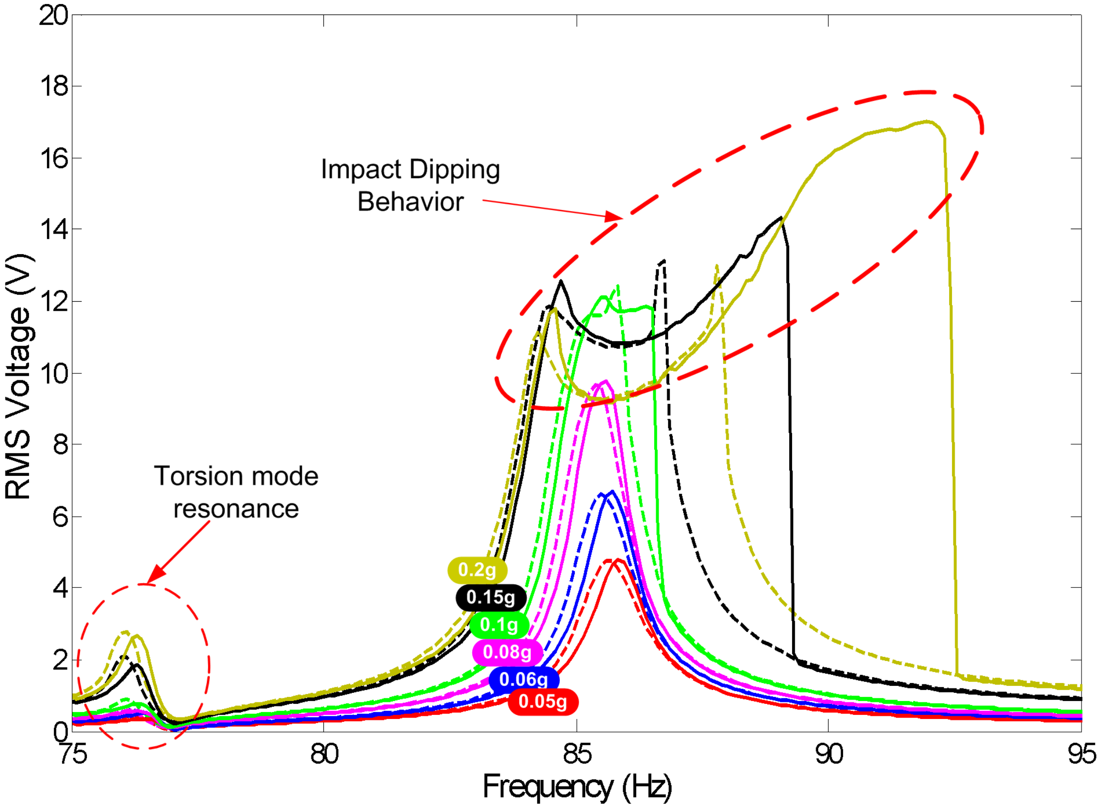

Figure 3.22: Frequency-response curves of the RMS output voltage for inertial mass $m_1 =$ 29.5 gm and base acceleration amplitudes in the range $A_\circ = 0.05 - 0.2\,g$ (RMS). Frequency up-sweeps are shown in solid lines and down-sweeps in dashed lines.

to the torsional mode which is less effective in energy harvesting than the bending mode. In fact, the time-history of the output voltage shows a signal at the forcing frequency Ω modulated by the torsional mode natural frequency f_t.

Figure 3.23 shows the output power and MPG bandwidth at the natural frequency of the bending mode $f_b = 86$ Hz for the fresh electret, inertial mass m_1, and base acceleration amplitudes in the range $A_\circ = 0.05 - 0.2\,g$ (RMS). The bandwidth of the MPG increases linearly with the amplitude of base acceleration in the hard impact region. On the other hand, the output power drops progressively in the hard impact region as higher excitation

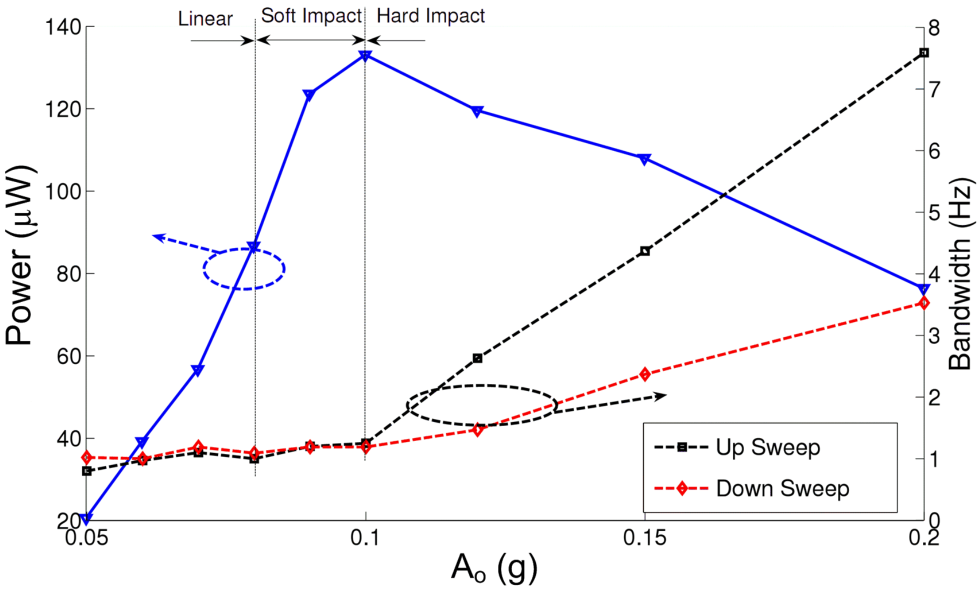

Figure 3.23: MPG prototype's average power and bandwidth at different accelerations for m_1.

amplitudes channel more kinetic energy into the inefficient torsional mode.

We note that, while increasing the inertial mass allows the MPG to capture more kinetic energy, it changes the optimal load resistance, as shown in Figures 3.24 and 3.25. Figure 3.24 shows that changing the load resistance from the nominal value $R = 1.1$ MΩ increases the output power from less than 100 μW to more than 900 μW in the range $R = 30 - 37$ MΩ. Figure 3.25 shows that decreasing the inertial mass to m_2 decreases the maximum output power to 130 μW and the optimal load resistance to the range $R = 10 - 20$ MΩ.

The analysis and results detailed above demonstrate the feasibility and advantages of electret-based out-of-plane switchless MPGs. In fact, the improved MPG demonstrates this potential by realizing almost 1mW of output power in Figure 3.24 at $A_\circ = 0.08\,$g (RMS) base acceleration amplitude. In addition, implementation and fabrication of this MPG are simple and use low-cost components. Table 3.3 compares the performance of

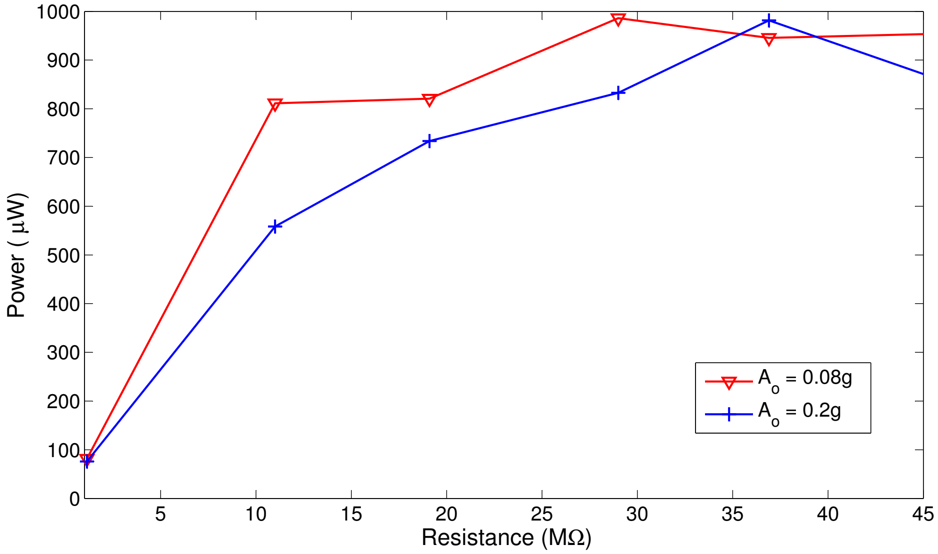

Figure 3.24: Average output power as a function of the load resistance R for the inertial mass m_1 and $g_{\circ 4}$.

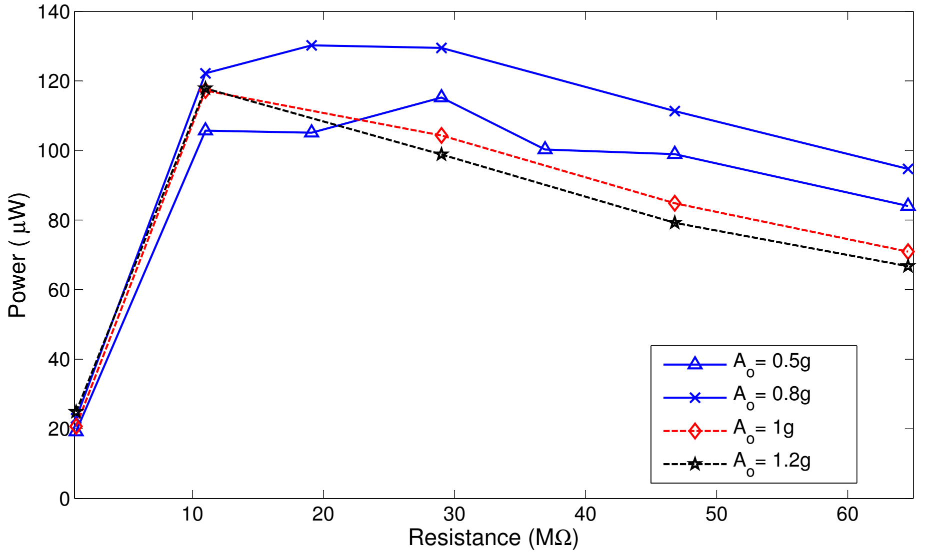

Figure 3.25: Average output power as a function of the load resistance R for the inertial mass m_2 and $g_{\circ 2}$ (solid lines) and $g_{\circ 3}$ (dashed lines).

Table 3.3: Comparison with previously published work.

ES MPG	Source	Size (cm^3)	Acceleration (g)	$f_\circ$ (Hz)	Power density (μW/cm^3)
Bartsch et al.[44]	External	20.3	N/A	90	0.36
Edamoto et al.[18]	Electret	1.22[1]	N/A	21	10.23
Hoffmann et al.[4]	External	0.2	13	1330	17.5
Kloub et al.[50]	External	0.17[1]	1	1740	29.8
This work	Electret	36	0.08	86	27.8

[1] Packaging thickness is assumed to be 0.4 cm

this electrostatic MPG to previously reported electrostatic MPGs. The results show that the improved prototype generates a power density closer to that of Kloub et al.[50] but at a much lower center frequency $f_\circ$ and excitation level. Further, several engineering enhancements can be easily introduced to minimize the volume of the device and increase the power density. For example, using 0.2 mm instead of 0.9 mm thick sheets in the moving structure will cut the beams length by more than one third without changing the MPG center frequency and, thus, more than doubling the power density.

We find that the capacitor gap should be set to match the requirements of the harvesting environment. On the other hand, increasing the electrostatic field strength, by using a high DC voltage source, is always advantageous, leading to more sensitive MPGs that can collect energy at lower excitation levels, have larger optimum output power, and have wider MPG bandwidth. A larger nominal capacitance and, thus, a larger capacitor area and a larger inertial mass allow for a larger optimum output power, however they change the nature of the electromechanical coupling in the MPG and require a search for the optimal load resistance.

Finally, the use of an electret layer as a DC charging source does not only make the MPG portable and low-cost, but also helps to isolate the two capacitive electrodes during impact. However, since charged electrets degrade with exposure to humidity, implementation of a good sealing is a must to preserve the electret charge over the lifetime of the MPG.

Chapter 4

In-plane Switchless Micro-Power Generators

4.1 Introduction

In Chapter 3, switchless electrostatic MPGs were presented with special focus on out-of-plane parallel-plate transducers. Another popular approach to implement energy harvesting transducers is the in-plane comb-finger architecture. Several implementations have been reported using this architecture because of its linearity and low mechanical damping losses [5, 6, 20, 34, 50]. However, implementing electrostatic MPGs using such a transducer has some limitations. These include:

- **Limited capacitance variability**
  The converted energy per cycle depends on the capacitance variability. Achieving large variability in this architecture requires long and/or deep fingers with narrow gaps. This configuration makes the structure susceptible to mismatches in the suspension system and can lead to a short circuit between the fingers [51].

- **Low silicon conductivity**

  The fabrication of in-plane comb-finger transducers uses the Deep Reactive Ion Etching (DRIE) process to etch through the silicon, thereby implementing thick fingers with narrow gaps that repeat over a wide area and achieve large capacitance. However, because of silicon's high sheet resistance, a distributed parasitic resistance appears across the variable capacitor that affects the MPGs performance for large capacitor footprints [2].

- **Difficulties in suspension**

  The movable electrodes require in-plane compliance and out-of-plane stiffness. As a result, high-aspect ratio beams are needed, which undermines the goal of low frequency operation. Moreover, long suspension beams are required to achieve compliance, which decreases the density of the fingers, the overall capacitance and, thus, the harvested energy.

- **Low energy conversion efficiency**

  The Q–V curves shown in Figures 3.4 and 3.5 demonstrate that out-of-plane architecture converts much more energy per vibration cycle than the in-plane comb-finger architecture.

Alternative in-plane MPGs are proposed in this chapter to overcome the limitation of the comb-finger architecture. In terms of the transducer topology, interdigitated planar electrodes are proposed to overcome the limited conductivity of silicon and increase the converted energy per vibration cycle. In Section 4.2, an electrical model of the interdigitated parallel-plate transducer is developed and used to show improved performance over conventional in-plane transducers. In Section 4.3, the performance of the interdigitated parallel-plate architecture is compared to that of the comb-finger architecture. It is shown that the interdigitated architecture increases the amount of harvested energy over that of the comb-finger architecture. New suspension techniques for in-plane energy harvesters are

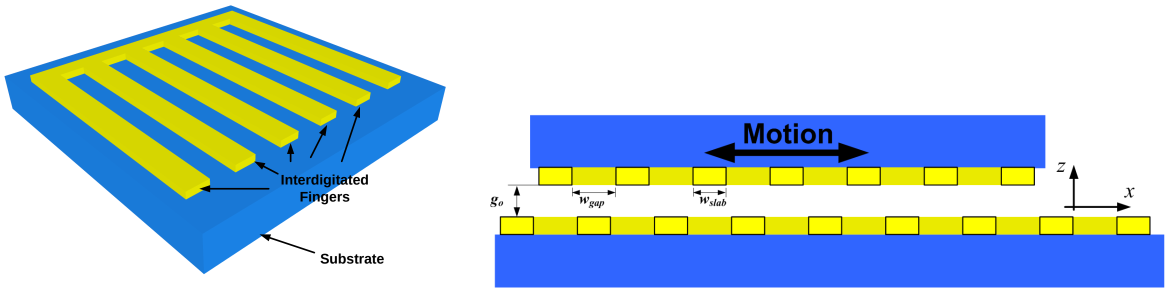

(a) (b)

Figure 4.1: (a) A 3D schematic of an electrode and (b) a cross-section through the interdigitated transducer.

presented in Sections 4.4 and 4.5. In Section 4.4, miniaturized MPGs with planar structure are presented. These MPGs are suitable for fabrication using surface micro-machined MEMS processes. In Section 4.5, a suspension system suitable for very low frequency MPGs is presented.

4.2 Interdigitated Transducer Model

Figure 4.1 shows a 3D schematic for one of the electrodes and a cross-section through the interdigitated parallel-plate capacitor. The transducer consists of n periodic metal slabs each of them is w_{slab} wide with an inter-slab gap of w_{gap} and a slab pitch of

$$p_s = w_{slab} + w_{gap}$$

such that $w_{slab} \leq w_{gap}$. The planar nature of the electrodes allows for the use of metallic slabs as electrodes to reduce parasitic distributed resistance.

The configuration of the interdigitated electrodes allows for full and zero overlap between a top moving electrode and a bottom fixed electrode as a carriage carrying the moving electrode travels along a rail, thereby maximizing the capacitance variation of the transducer. Moreover, the periodicity of the slabs leads to multiple maxima and minima during one vibration cycle. For example, a carriage stroke of $x_\circ$ leads to

$$j = \frac{x_\circ}{p_s}$$

cycles of maximum-to-minimum capacitance variation and j cycles of energy conversion per carriage cycle.

Setting the nominal position of the movable electrode to $x = 0$ where full overlap occurs between the electrodes, assuming a large number of slabs per electrode (thereby justifying neglecting the edge effects at the first and last slabs), and ignoring the fringing field, we use parallel-plate theorem to find the nominal capacitance of the interdigitated capacitor as

$$C_\circ = \frac{n\epsilon_\circ L_c w_{slab}}{g_\circ} \tag{4.1}$$

where n is the number of slabs per electrode, L_c is the slab length, and $g_\circ$ is the gap between the electrodes. The capacitance of the variable capacitors varies with the overlap area between the slabs, and thereby the carriage displacement x, according to the relationship

$$C_v(x) = C_\circ\, s_1\Big(\frac{2\,x}{p_s}\Big) \tag{4.2}$$

where $s_1(u)$ is a periodic triangular function defined as

$$s_1(u) = \begin{cases} 1 - |u| & |u| \le 1 \\ s_1(u \pm 2) & |u| > 1 \end{cases}$$

The Q–V curves of the interdigitated transducer were obtained by substituting the expression of C_v obtained in (4.2) into the KVL equation of the switchless (continuous) transducer (3.4) and solving the resulting differential equation for a harmonic displacement

$$x(t) = x_o \sin(\Omega t + \gamma)$$

Figure 4.2 shows the Q–V curves for transducers with $j = 5$ and 10 conversion cycles and the same nominal capacitance $C_\circ$, where the time is normalized to the vibration period

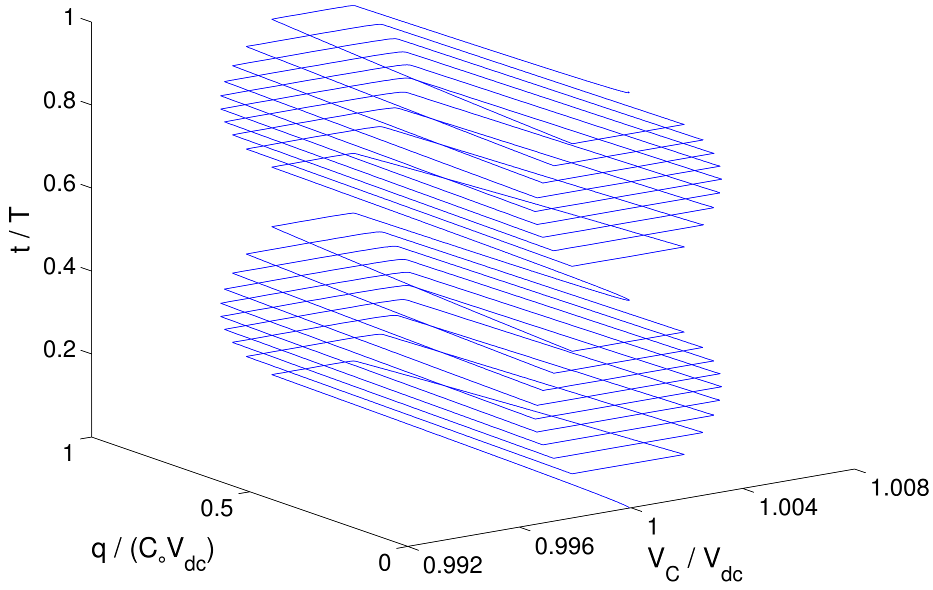

(a)

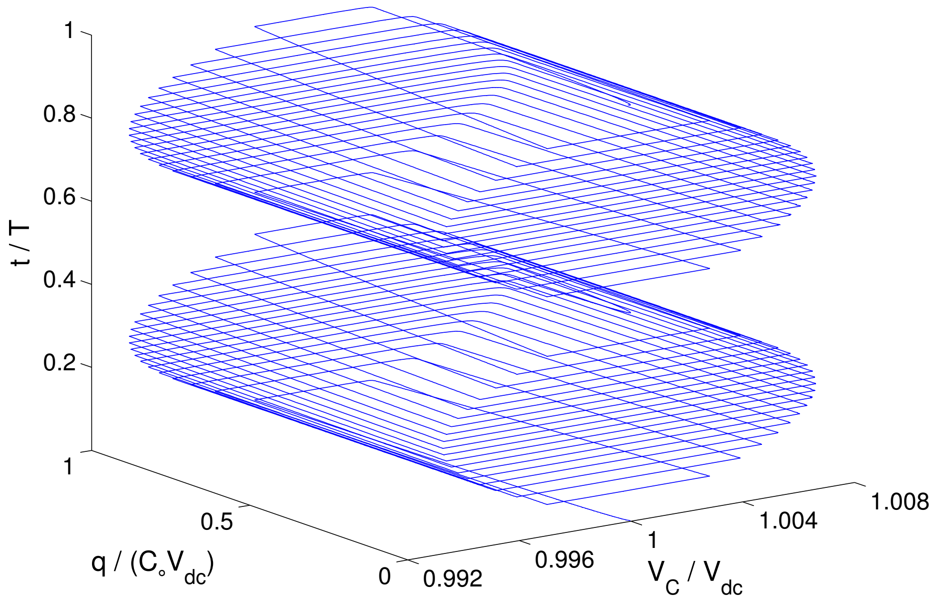

(b)

Figure 4.2: Q–V curves for two interdigitated transducers with the same nominal capacitance and $C_\circ$: (a) $j = 5$ and (b) $j = 10$ conversion cycles.

$T = \frac{2\pi}{\Omega}$. The energy generated per vibration period is equal to the algebraic sum of the areas enclosed in each plane (conversion cycle). The two curves in Figure 4.2 illustrate the effect of changing the slab pitches. Decreasing the slab pitch allows for more conversion cycles per vibration period. Moreover, decreasing the slab pitch increases the rate of change of capacitance, thereby enlarging the area of an individual conversion cycle.

The curves in Figure 4.2 suggest that minimizing the slab pitch allows for more energy generation cycles per vibration cycle. However, as the slab pitch p_s decreases compared to the capacitor gap $g_\circ$, the fringing field increases and it becomes imperative to account for its contribution to the capacitance. The capacitance model in equation (4.2) is, therefore, modified by introducing two constant fitting parameters C_l and C_d to account for the fringing field as follows:

$$C_v(x) = C_\circ \Big[C_l \, s_1\Big(\frac{2x}{p_s}\Big) + C_d \Big] \tag{4.3}$$

Electrostatic finite element analysis (FEA) was carried out using the commercial code COMSOL to extract the capacitance of an interdigitated capacitor with $w_{slab} = 10 g_\circ$ and $w_{gap} = 12 g_\circ$ as a function of the carriage displacement. The results were used to estimate the fitting parameters as $C_l = 0.85$ and $C_d = 0.4$. Figure 4.3 shows the FEA-extracted capacitance and the capacitance calculated using the models (4.3) with, and (4.2) without fringing field effects. The curves show that the fringing field leads to a significant constant shift in the capacitance and a smaller drop in the linear proportionality constant between displacement and capacitance. The modified linear model captures both of these effects well, producing a better estimate of the capacitance variation with the displacement than the original model. Further, the results indicate that a more accurate model can be obtained using a quadratic function to approximate the capacitance variation with the displacement.

In this section, the electrical performance of the interdigitated in-plane transducer was investigated. The results indicate potential of this transducer to improve the energy

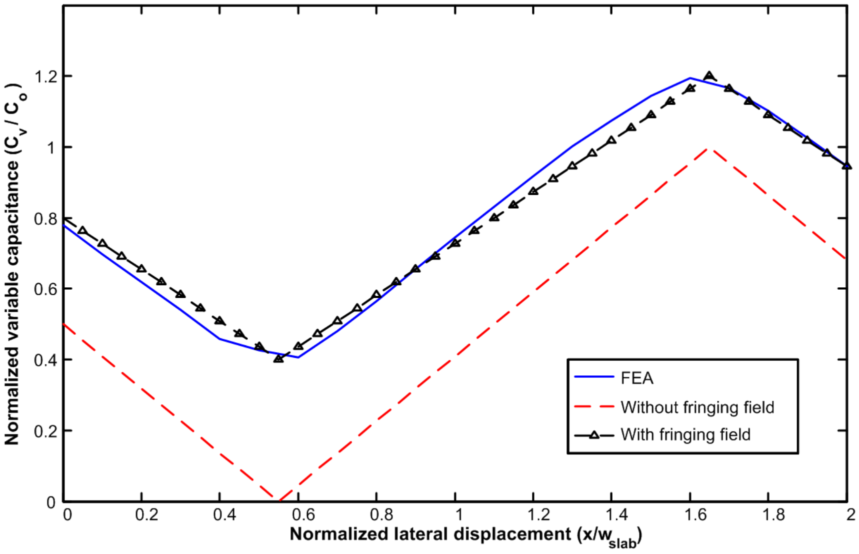

Figure 4.3: Comparison between the finite element simulation and two variable capacitance models.

converted per vibration cycle. Further, the interdigitated in-plane transducer has a planar structure that allows for the realization of smaller harvesters, less parasitic resistance, and lower fabrication cost. In the next section, the interdigitated transducer is employed in an energy harvester and its performance is compared to that of the overlapping comb-finger transducer reported in the literature [5, 20].

4.3 Interdigitated Parallel-Plate Energy Harvester

Several energy harvesters have been reported in the literature using overlapping comb-finger transducers [5, 6, 20, 34, 50]. A typical example of these harvesters is that proposed by Sterken et al. [20]. Figure 4.4 shows a schematic of the circuit topology used in that harvester. External vibrations vary the capacitances of the capacitors C_1 and C_2 in opposite sense. In the presence of identical load resistances, the charge will oscillate back and forth

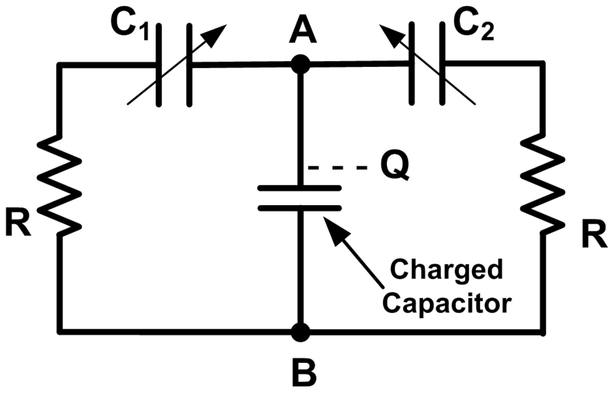

Figure 4.4: Circuit diagram of Sterken et al.'s [20] energy harvester.

due to the opposite capacitance variation in the variable capacitors. As a result, an out-of-phase current will pass through the loads while negligible current will pass through the constant capacitor due to the circuit symmetry.

Sterken et al. proposed an implementation of this harvester using two overlapping comb-finger capacitors. An electret layer is inserted between the fixed and movable electrode of the comb-finger capacitor and used as a charging source [20]. Figure 4.5 shows a cross-section of this harvester implementation. This implementation suffered from the limitations of overlapping comb-finger transducers discussed earlier.

Figure 4.6 shows an alternative implementation of the same harvester using the interdigitated transducer proposed in Section 4.2. The harvester consists of two in-plane parallel-plate variable capacitors C_1 and C_2 each having n metallic slabs with slab width w_{slab} and initial overlap $w_{slab}/2$. The slabs of each capacitor are arranged so that capacitance variation in the two capacitors have opposite sense in a manner similar to that realized by Sterken et al. [20]. The suspension of the moving electrode, electrode A, was designed to allow motion in the x-direction while preventing motion in the z-direction

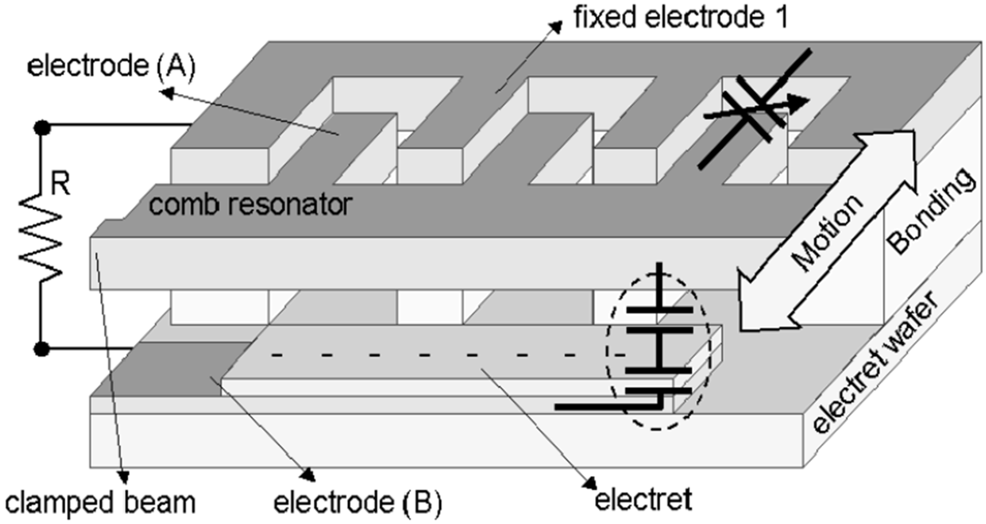

Figure 4.5: Schematic cross-section of Sterken et al.'s [20] comb-finger harvester implementation.

(*i.e.*, $k_x \ll k_z$). The two capacitors are identical with a nominal capacitance at $x = 0$ of

$$C_\circ = \frac{n\epsilon_\circ w_{slab} L_c}{2\, g_\circ} \tag{4.4}$$

The nominal capacitance realized under this configuration is half that realized under the configuration shown in (4.1) due to the initial overlap between the slabs of the fixed and moving electrodes.

The charging source of the variable capacitors is the embedded electret layer shown in Figure 4.6. The electret layer is made of a dielectric sheet with quasi-permanent polarized charges that can last for years [36]. It produces charges on the movable electrodes via charge induction. Using Gauss law, the voltage across the combined capacitor made of the continuous center capacitor and the electret layer embedded in between is [20]

$$\begin{aligned} V_{center} &= \frac{Q}{C_{et}} + \sigma\frac{d}{\epsilon_\circ\epsilon_{et}} \\ &= \frac{Q}{C_{et}} + V_{et} \end{aligned} \tag{4.5}$$

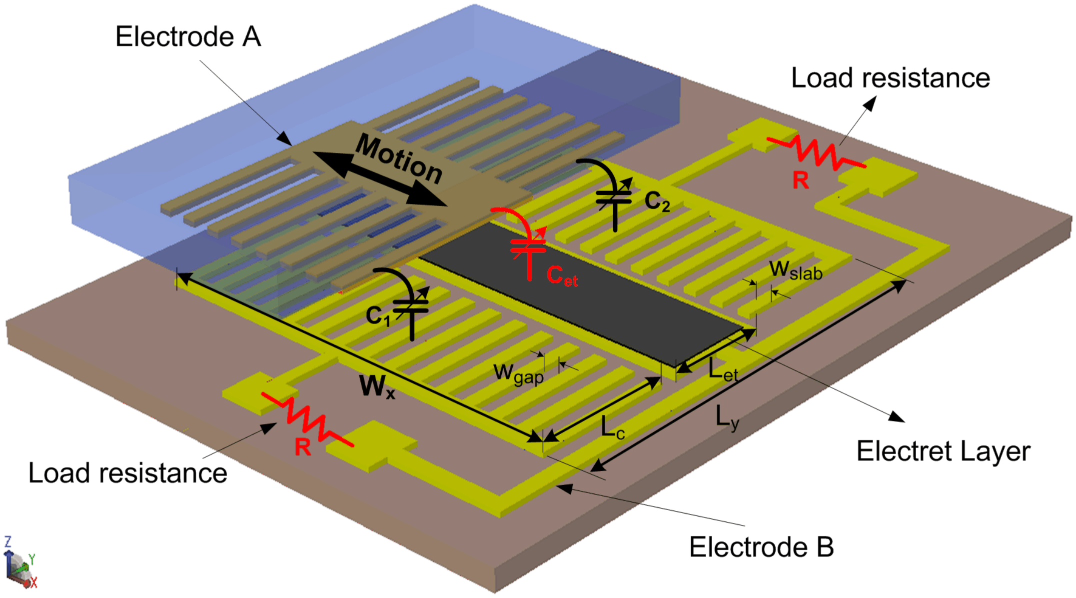

Figure 4.6: Schematic cross-section of the new interdigitated harvester implementation.

where $|Q|$ is the charge on each plate of the center capacitor, σ, d, and ϵ_{et} are the surface charge density, the electret thickness, and the relative permittivity of the electret sheet, and C_{et} is the capacitance of the electret sheet in the absence of surface charge. This capacitance is equal to

$$C_{et} = \frac{\epsilon_\circ w_x L_{et}}{(g_\circ - d) + \frac{d}{\epsilon_{et}}} \tag{4.6}$$

where $w_x L_{et}$ is the electret area. Using (4.5), the center capacitor can be modeled as a voltage source V_{et} in series with a fixed capacitor C_{et}. Finally, to account for the initial overlap and the opposite variation sense of the variable capacitors C_1 and C_2, the capacitance variation model (4.3) is written as

$$C_i(x) = 2\,C_\circ\Big[C_l s_1\big(\frac{2x}{p_s} \pm \frac{1}{2}\big) + C_d\Big] \tag{4.7}$$

where the + sign is used for C_1 and the − sign is used for C_2.

The system model was derived by applying Kirchhoff's voltage law to the electric circuit and writing the equation of motion of the inertial mass. The result is

$$
\begin{aligned}
V_{et} &= R\dot{q}_1 + V_{C_1}(q_1, x) + V_{C_{et}}(q_1, q_2) \\
V_{et} &= R\dot{q}_2 + V_{C_2}(q_2, x) + V_{C_{et}}(q_1, q_2) \\
m\ddot{x} &= F_2(q_2, x) - F_1(q_1, x) - k_1 x - c_m \dot{x} - m a_y(t)
\end{aligned}
\tag{4.8}
$$

where R is the load resistance, c_m is the mechanical damping coefficient, and $a_y(t)$ is the base acceleration. The state variables q_1, q_2, and x correspond to the charge on the variable capacitors C_1 and C_2, respectively, and the displacement of the inertial mass m in the x-direction. The driving efforts are

$$
V_{C_i} = \frac{q_i(t)}{C_i(x)}, \quad F_i = \frac{1}{2}\frac{\partial}{\partial x}\left(\frac{q_i^2(t)}{C_i(x)}\right) \tag{4.9}
$$

Inserting (4.7) into (4.9), we obtain the voltage drops across the variable capacitors as

$$
\begin{aligned}
V_{C_1} &= \frac{q_1}{2\,C_\circ\Big[C_l s_1\big(\frac{2x}{p_s} + \frac{1}{2}\big) + C_d\Big]} \\
V_{C_2} &= \frac{q_2}{2\,C_\circ\Big[C_l s_1\big(\frac{2x}{p_s} - \frac{1}{2}\big) + C_d\Big]}
\end{aligned}
\tag{4.10}
$$

and the electrostatic forces as

$$
\begin{aligned}
F_1 &= \frac{C_l s_2\big(\frac{2x}{p_s} + \frac{1}{2}\big)}{2C_\circ p_s} \frac{q_1^2}{\Big[C_l s_1\big(\frac{2x}{p_s} + \frac{1}{2}\big) + C_d\Big]^2} \\
F_2 &= \frac{C_l s_2\big(\frac{2x}{p_s} - \frac{1}{2}\big)}{2C_\circ p_s} \frac{q_2^2}{\Big[C_l s_1\big(\frac{2x}{p_s} - \frac{1}{2}\big) + C_d\Big]^2}
\end{aligned}
\tag{4.11}
$$

where $s_2(u)$ is a periodic function defined as

$$
s_2(u) = \begin{cases} -sgn(u) & |u| \leq 1 \\ s_2(u \pm 2) & |u| > 1 \end{cases}
$$

The voltage drop across the fixed capacitor C_{et} is

$$
V_{C_{et}} = \frac{q_1 + q_2}{C_{et}} \tag{4.12}
$$

In the absence of motion, the initial charge on each of the variable capacitors is $q_\circ = C_\circ V_\circ$ where $V_\circ$ is the initial voltage drop on the variable capacitor calculated from

$$V_\circ = V_{et}\frac{C_{et}}{2C_\circ + C_{et}} \tag{4.13}$$

We substitute (4.10), (4.11), and (4.12) into (4.8) and introduce the nondimensional variables

$$\hat{t} = t\omega\ ,\quad \hat{q}_1 = \frac{q_1}{q_\circ}\ ,\quad \hat{q}_2 = \frac{q_2}{q_\circ}\ ,\quad \hat{x} = \frac{x}{p_s/2} \tag{4.14}$$

to the resulting system of equations to obtain the nondimensional system equations

$$\begin{aligned}
\dot{\hat{q}}_1 &= -\frac{\omega_e\,\hat{q}_1}{2\left[C_l s_1\left(\hat{x}+\frac{1}{2}\right)+C_d\right]} - \omega_{et}(\hat{q}_1+\hat{q}_2) + I_{et}\\
\dot{\hat{q}}_2 &= -\frac{\omega_e\,\hat{q}_2}{2\left[C_l s_1\left(\hat{x}-\frac{1}{2}\right)+C_d\right]} - \omega_{et}(\hat{q}_1+\hat{q}_2) + I_{et}\\
\ddot{\hat{x}} &= \eta s_2\left(\hat{x}+\tfrac{1}{2}\right)\frac{\hat{q}_1^2}{\left[C_l s_1\left(\hat{x}+\frac{1}{2}\right)+C_d\right]^2}\\
&\quad + \eta s_2\left(\hat{x}-\tfrac{1}{2}\right)\frac{\hat{q}_2^2}{\left[C_l s_1\left(\hat{x}-\frac{1}{2}\right)+C_d\right]^2} - \hat{x} - 2\zeta\dot{\hat{x}} - \hat{A}_\circ\cos(\hat{\Omega}\hat{t})
\end{aligned} \tag{4.15}$$

where $\omega = \sqrt{k_1/m}$ is the natural frequency of the uncoupled mechanical oscillator. The following parameters were introduced to simplify writing the system of equations

$$\begin{aligned}
\omega_e &= \frac{1}{\omega R C_\circ}, & \omega_{et} &= \frac{1}{\omega R C_{et}}, & I_{et} &= \frac{V_{et}}{\omega R C_\circ V_\circ}\\
\eta &= \frac{C_\circ {V_\circ}^2 C_l}{m {p_s}^2\omega^2}, & \zeta &= \frac{c_m}{2m\omega}, & \hat{\Omega} &= \frac{\Omega}{\omega}, & \hat{A}_\circ &= \frac{2\,A_\circ}{\omega^2 p_s}
\end{aligned} \tag{4.16}$$

The system of equations (4.15 is a coupled nonlinear differential system whose analytical solution is not available. While linearization of the system equations is useful in understanding the system behavior, Peano et al. [5] showed that optimization of the linear system leads to erroneous results. Therefore, the system of equations (4.15) were solved numerically.

The dimensions and parameters of the energy harvester under study are listed in Table 4.1. The amplitude $A_\circ$ and frequency Ω of the base acceleration used in the calculations

Table 4.1: The system parameters of the interdigitated energy harvester.

W_x	2.4 mm	L_y	4.7 mm
w_{slab}	40 μm	w_{gap}	48 μm
n	27 slabs	w_{et}	48 μm
$g_\circ$	4 μm	L_c	2.3 mm
V_{et}	150 V	c_m	25.5 μNs/m
$A_\circ$	163.8 m/s^2	Ω	5724 rad/s^2

are the same as those used by Sterken et al. [20] and Peano et al. [5]. The average output power was obtained by averaging the instantaneous output power $P(t)$ calculated from [5]

$$P(t) = \frac{q_\circ V_\circ \omega}{\omega_e} \left[\left(\frac{d\hat{q}_1}{d\hat{t}} \right)^2 + \left(\frac{d\hat{q}_2}{d\hat{t}} \right)^2 \right] \tag{4.17}$$

over a period of excitation $T = 2\pi/\Omega$.

The load resistance and natural frequency of the mechanical oscillator were varied to optimize the harvester output power. Figure 4.7 shows the average output power of the energy harvester for a range of natural frequencies and load resistances. The output power saturates to a maximum in the natural frequency range of 5600 to 5700 rad/s since a limiter was used to limit the carriage motions.

The parameters of the optimal operating point of the interdigitated harvester are shown in Table 4.2. The optimized harvester was predicted to produce 89 μW output power at 6 MΩ load resistance using a mechanical oscillator with a natural frequency of 5620 rad/s. This is more than 78% improvement in the output power over that predicted for the comb-finger harvester [5] achieved in conjunction with a one-order of magnitude reduction in the optimal load resistance over that of Peano et al. [5]. Figure 4.8 shows the nondimensional charge, current, displacement, and capacitance for the optimal interdigitated energy harvester.

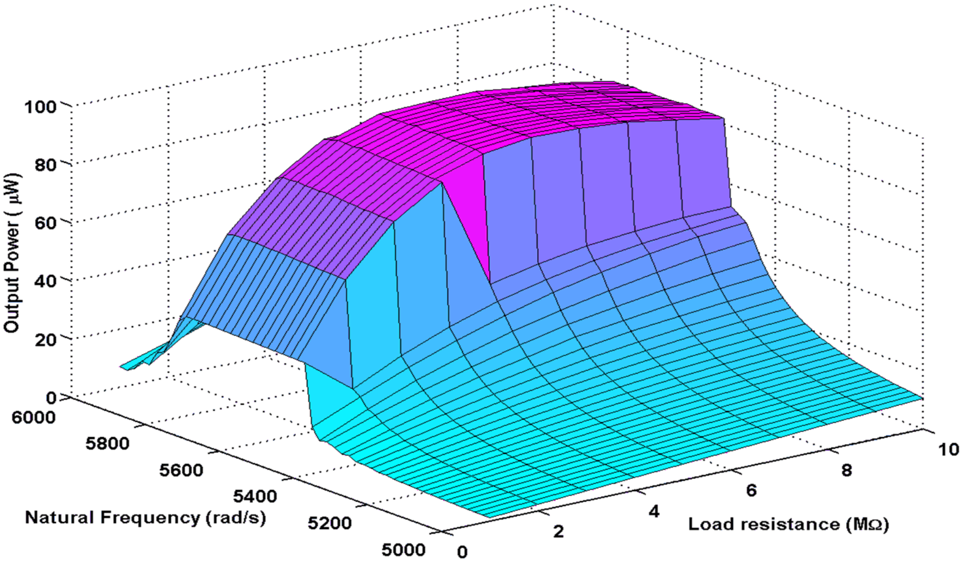

Figure 4.7: The average output power of the interdigitated energy harvester for a range of load resistances and natural frequencies.

Table 4.2: Optimal performance of the interdigitated energy harvester.

	This work	[5]
Size	4.7 mm × 2.4 mm	5 mm × 2.3 mm
Output Power	89 μW	50 μW
Natural Frequency	5620 rad/s	5080 rad/s
Load resistance	6 MΩ	70 MΩ

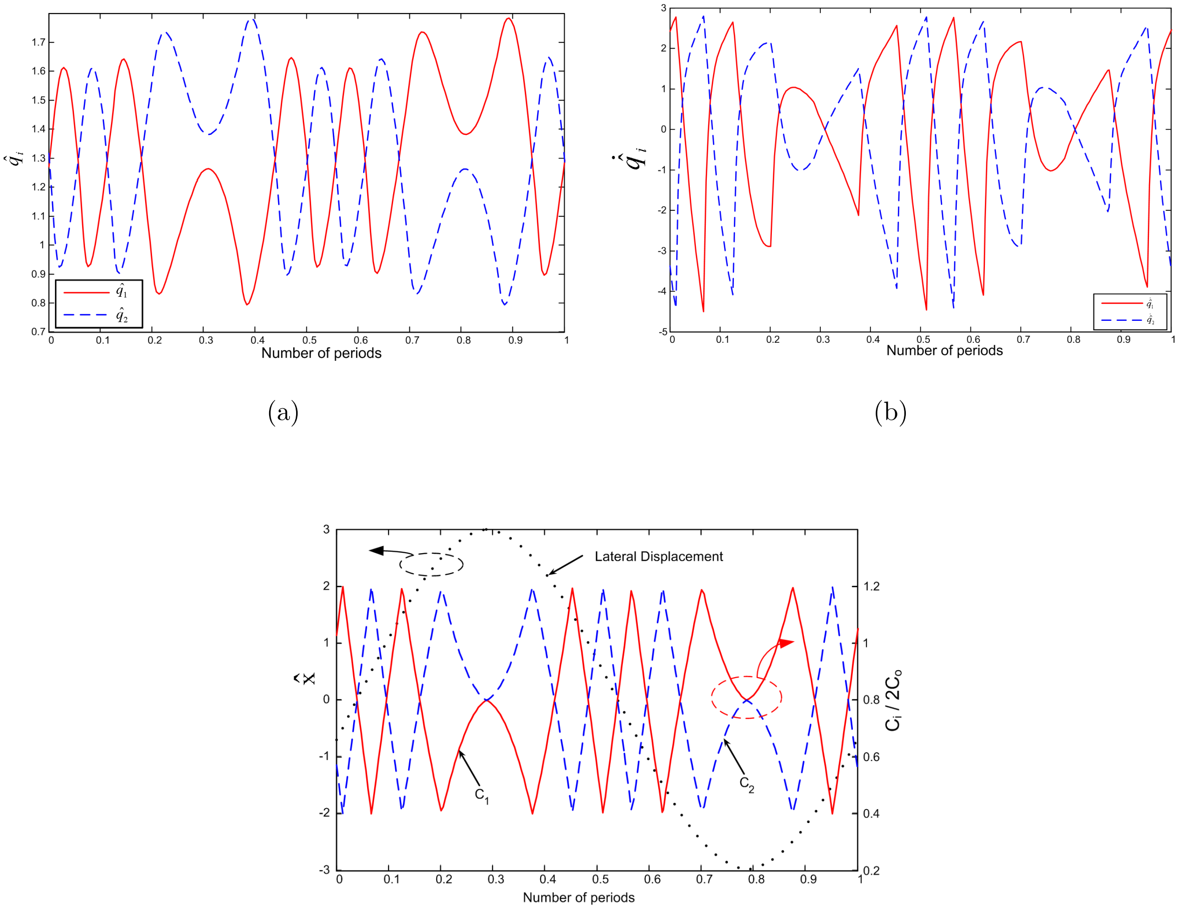

(a) (b)

(c)

Figure 4.8: The nondimensional (a) charge $\hat{q}_i$, (b) current $\dot{\hat{q}}_i$, (c) displacement $\hat{x}$ and capacitance $\frac{C_i}{2C_\circ}$ of the interdigitated energy harvester at the optimal operating point

In this section, the use of the in-plane interdigitated transducer to realize a new energy harvester was investigated. The results show superior performance, namely more output power and lower optimal load resistance, over that of the previous implementation using overlapping comb-finger transducers. In the next section, we investigate the realization of this energy harvester and possible approaches to improve the suspension systems of in-plane energy harvesters.

4.4 Miniaturized Surface Micromachined MPGs

In the preceding two sections, we demonstrated the advantage of the use of interdigitated transducers in energy harvesting. However, practical realization of this harvester depends on the development of a compatible fabrication process. For small form factor devices, like wireless sensors and embedded systems, successful integration of vibration energy harvesters within these systems requires miniaturization while maintaining efficient generation and operation [52]. Scaling down of electromagnetic forces with length ranges between L^3 and L^4, while the scaling down of electrostatic forces with length ranges somewhere between L^1 and L^2 [53]. As a result, electrostatic energy harvesters are better candidates for miniaturization. Moreover, electrostatic energy harvesters are more compatible with surface micro-fabrication processes.

Efficient harvesting requires the center frequency of the energy harvesters to be close to the fundamental frequency of environmental vibrations. The natural frequency of a linear mechanical oscillator is

$$\omega = \sqrt{\frac{k_1}{m}} \tag{4.18}$$

where k_1 is the linear stiffness of the support structure and m is the effective mass. The fundamental frequency in most vibration sources is below 200 Hz [2]. Fabricating miniaturized harvesters with a center frequency in this range is quite challenging. In the next subsection, miniaturization challenges for electrostatic energy harvesters are presented.

4.4.1 Miniaturization Challenges

The ultimate goal in miniaturization is to scale down the device without affecting its generated power. Therefore, it is important to study the factors affecting the amount of harvested energy during miniaturization. There are four important parameters that affect the amount of harvested energy by capacitive transducers. The first is the kinetic energy content in the system, which is mainly driven by the inertia of the inertial mass and the amount of mechanical damping present in the system. Increasing the inertial mass m and decreasing the damping ratio ζ_m lead to a larger stroke and, therefore, more vibration energy available to harvest.

The second parameter is the strength of the electrostatic field. Energy harvesting occurs through electrical damping of the mechanical oscillator. Electrical damping increases with the strength of the field, which is a function of the applied voltage and the nominal capacitance value. Therefore, maximizing the operating voltage and the nominal capacitance are requirements for strong electrical damping and more harvested energy.

The third parameter is realization of the optimal operation point by matching the electrical and mechanical damping forces [46, 54]. Therefore, the electrical damping in the capacitive transducer should be optimized to maximize the power flow to the electrical system.

The fourth parameter is the ability of the electrical subsystem to store the captured kinetic energy as electrical potential energy by changing the capacitance value [34]. Therefore, it is necessary to realize variable capacitors with a wide variation range to improve the transduction capacity of the harvester.

In conclusion, the miniaturized electrostatic energy harvesters should aim to increase their inertial mass, lower their mechanical damping, operate at high voltage, and use variable capacitors with a large nominal capacitance and a wide capacitance variation range. As a result, in-plane capacitive transducers are widely used in miniaturized MPGs because of their low mechanical damping and wider capacitance variation range compared to capacitive out-of-plane transducers [2, 5, 6, 20, 34, 50].

However, miniaturization of in-plane transducers adds additional constraints on the harvester suspension system. In-plane motions require suspension beams that are compliant in-plane and highly stiff out-of-plane, such as high aspect ratio beams. Figure 4.9 shows

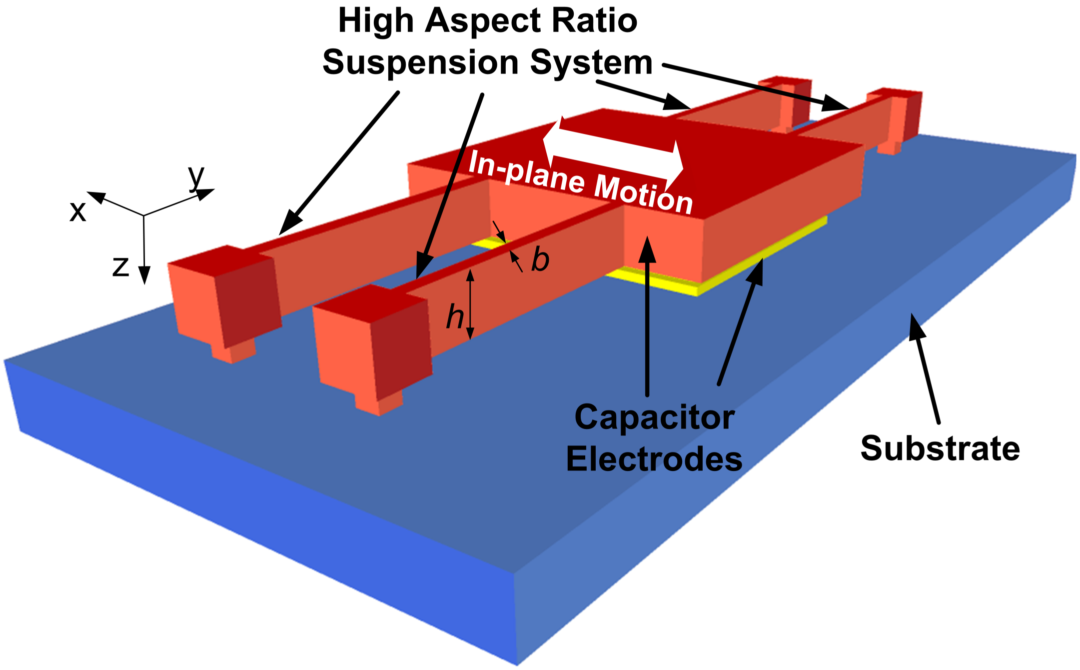

Figure 4.9: The conventional suspension system.

a conventional suspension system for in-plane transducers. The ratio between the beam stiffness in the x- and z-directions depends on the beam cross-section. For a rectangular cross-section, this ratio is given by

$$\frac{k_x}{k_z} = \left(\frac{b}{h}\right)^2 = \frac{1}{r^2} \tag{4.19}$$

where b, h, and r are the beam width, thickness, and aspect ratio, respectively.

Similarly, miniaturizing of capacitive transducers requires minimization of the gap between the capacitor electrodes to ensure a large nominal capacitance [34]. Decreasing the gap between the fingers in overlapping comb-finger transducers makes the suspended structure very sensitive to any mismatch between the suspension beams, leading to a short circuit between the fingers [51]. Decreasing the capacitor gap in interdigitated parallel-plate transducers makes the suspended structure liable to pull-in by electrostatic forces. The deflection of the transducer electrodes due to the electrostatic force between the electrodes depends on the value of the applied voltage. The maximum voltage that can be applied without collapse is the pull-in voltage of the capacitor. The static pull-in voltage is [55]

$$V_{pull-in} = V_{max} = \sqrt{\frac{8}{27}\frac{k_z g_\circ^3}{\epsilon_\circ A}} \tag{4.20}$$

where A and $g_\circ$ are the capacitor area and nominal gap. Using a substrate and inertial mass made of silicon, solving for k_z in terms of r and m from (4.18) and (4.19), and substituting the result into (4.20), we obtain an estimate of the maximum voltage in the form

$$V_{max} = \omega\sqrt{\frac{8}{27}\frac{h\rho_{Si} r^2 g_\circ^3}{\epsilon_\circ}} \tag{4.21}$$

where ρ_{Si} is the density of silicon.

We use (4.21) to plot the maximum voltage that can be applied to interdigitated parallel-plate transducers as a function of the natural frequency of the mechanical oscillator in Figure 4.10. The results show that the oscillator low natural frequency required to realize low MPG center frequency sets a significant constraint on the maximum stable

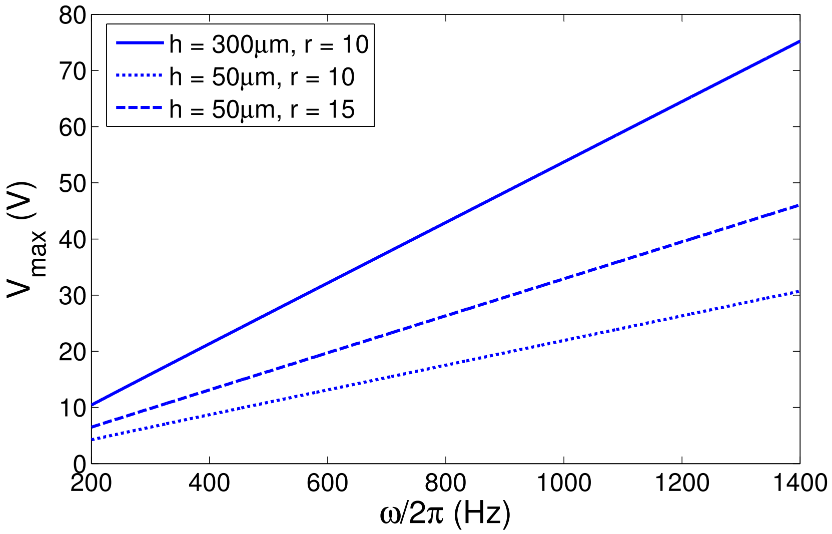

Figure 4.10: Maximum applied voltage for different natural frequency.

voltage that can be applied to the transducer, especially for small capacitor gaps. As a result, miniaturizing in-plane parallel-plate transducers lowers the strength of the electrostatic field and, therefore, significantly decreases the amount of electrical energy harvested. Table 4.3 summarizes miniaturization challenges of capacitive transducers discussed above.

In the next subsection, a novel suspension system is presented that overcomes the pull-in instability by decoupling the natural frequency of the oscillator from the maximum stable transducer voltage.

Table 4.3: Miniaturization challenges of capacitive transducers.

Transducer Architectures	**Miniaturization Challenges**
Out-of-plane parallel-plate	• Pull-in instability • High squeeze-film damping
In-plane overlapping comb-finger	• High aspect ratio beams for motion isolation • Mismatch instability for long fingers and small gaps
In-plane parallel-plate	• High aspect ratio beams for motion isolation • Pull-in instability

4.4.2 Dimple-Based Suspension System

A novel suspension system was developed to decouple the relation between the maximum applied voltage and the natural frequency and alleviate the need for high aspect ratio beams. The new suspension system uses dimples for suspension similar to those used in electrostatic motors. In addition, compliant beams are used to guide the lateral motion rather than to support the inertial mass.

Figure 4.11 illustrates the new suspension system. The beams are fabricated using

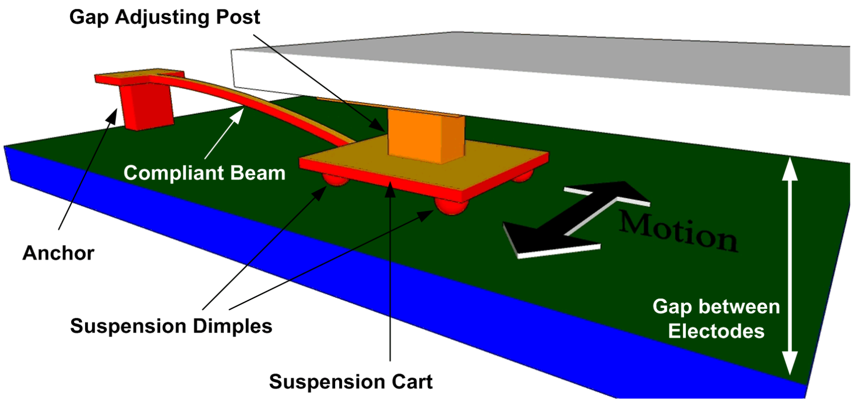

Figure 4.11: A novel suspension system for in-plane energy harvesters.

surface micro-machining to ensure their compliance. The beams are connected to a carriage supported by dimples to decrease friction and prevent stiction. The two electrodes are fabricated in two different substrates with one of the substrates containing the suspension system and one set of electrodes while the other substrate contains the second set of electrodes. The two substrates are bonded together to form the transducer. The gap is defined using a gap adjusting post to support the moving electrode, prevent pull-in, and ensure uniform gap. The suspension system provided in this transducer is a compromise between the use of thick beams with high stiffness to support the inertial mass and lower damping and the use of thin beams to lower the center frequency of the harvester.

A 3D schematic of the energy harvester is shown in Figure 4.12. The energy harvester has two variable capacitors with interdigitated slabs. The orientation of the slabs determines the harvester operation mode. When the slabs of the two capacitors are configured to provide for out-of-phase capacitance variation between the two capacitors, the harvester operates in a balanced mode similar to that of Sterken et al.'s [20]. When the slabs are configured to provide for in-phase capacitance variation for the two capacitors, the harvester operates as a simple interdigitated transducer. This mode is useful for single load operation. Figure 4.13 shows the connections of the two configurations where the electrodes colored in orange are placed in the top substrate of the schematic shown in Figure 4.12 while the electrodes in the bottom substrate are colored in red.

In the next section, a prototype of the interdigitated energy harvester using the dimple suspension was fabricated using surface micro-machining and used to demonstrate the new transducer and suspension system.

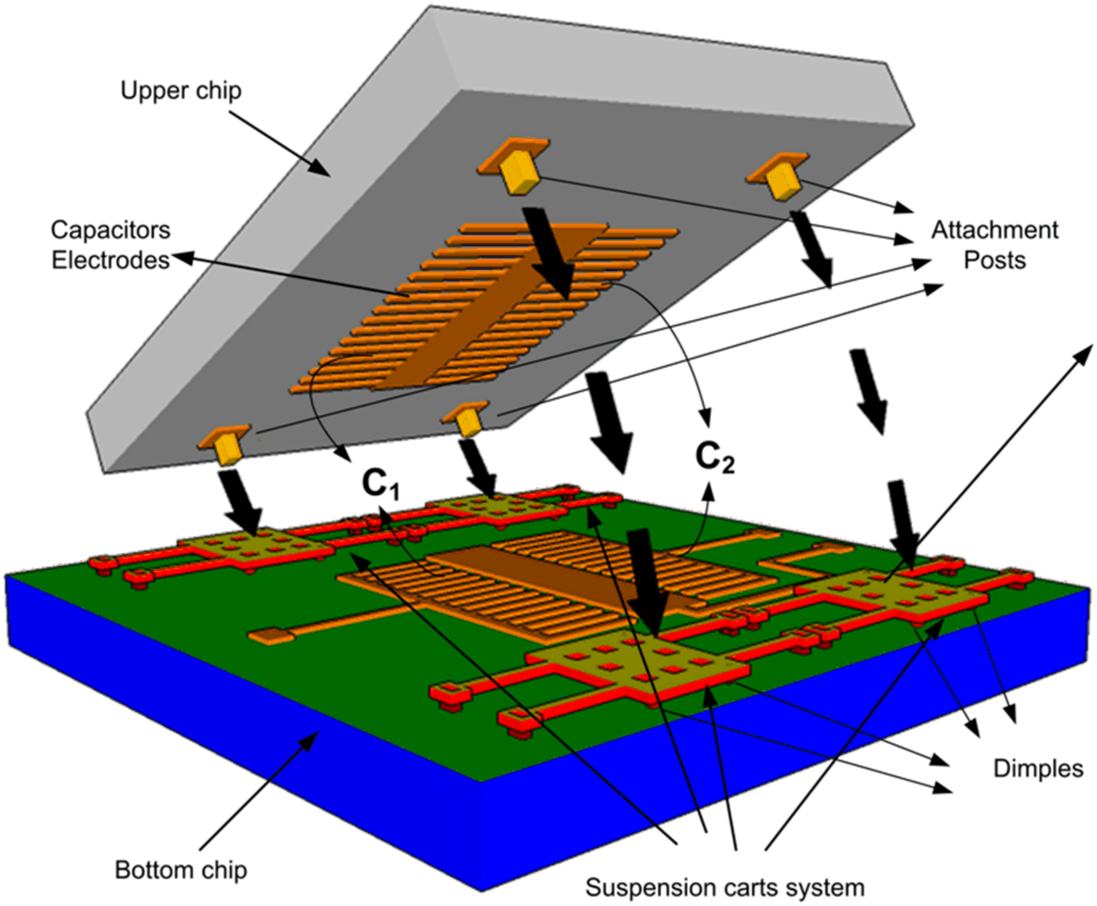

Figure 4.12: A 3D schematic of the capacitive transducer.

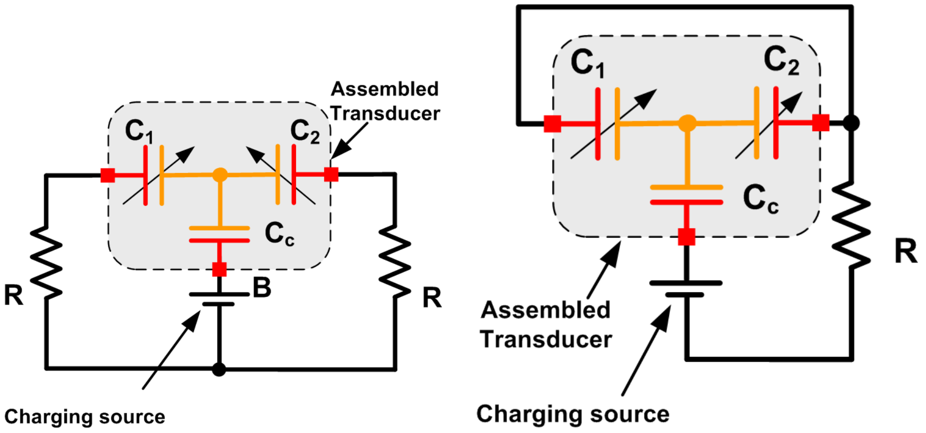

(a) (b)

Figure 4.13: Two configurations of the interdigitated energy harvester: (a) The double load harvester where C_1 and C_2 vary out-of-phase and (b) the single load harvester where C_1 and C_2 vary in-phase.

4.4.3 Prototype Fabrication and Postprocessing

A prototype employing the new suspension was fabricated using hybrid integration of two chips. The two chips were fabricated using surface micro-machining processes. The first chip carrying the bottom substrate in Figure 4.12 was fabricated using PolyMUMPs process. This is a commercial fabrication process offered by MEMSCAP, Inc. It has three structural layers and two sacrificial layers on a silicon substrate coated with silicon nitride for isolation [56]. The fabricated chip was postprocessed in the CIRFE (Center of Integrated RF Engineering) laboratory to minimize the parasitic capacitance of the silicon substrate.

The other chip carrying the top substrate was fabricated in the CIRFE lab. The fabrication process has one structural layer and no sacrificial layers. The assembly process of the two chips consists of flip-chip bonding of the two chips followed by sacrificial layer etch using Hydrofluoric acid for release. In the next paragraphs, fabrication considerations and results of the two-chip fabrication process are presented.

- **PolyMUMPs chip**

This chip carries the bottom substrate of the energy harvester, which contains one of the capacitive electrodes and the suspension system. The silicon nitride layer covering the substrate is used as an electret by electrically charging it after fabrication and assembly.

The substrate used in PolyMUMPs process is a highly doped crystalline silicon substrate with low resistivity covered with a layer of silicon nitride as an insulator. To understand the effect of the substrate type on the interdigitated harvester performance, consider the transducer cross-section shown in Figure 4.14(a). The capacitance of each of the variable capacitors is

$$C_i = C_{par} + \frac{C_{vi} C_b}{C_{vi} + C_b} \tag{4.22}$$

where C_{vi}, C_{par}, and C_b are the capacitance between the variable capacitor slabs, the capacitance between the top electrode and the silicon substrate, and the capacitance between the bottom electrode and the silicon substrate, respectively. Since the silicon nitride layer is very thin, C_b is much larger than C_v and we can approximate the capacitance of the variable capacitor as

$$C_i \approx C_{par} + C_{vi} \tag{4.23}$$

Further, C_{par} and $C_{vi_{max}}$ are of the same order-of-magnitude and are much larger than $C_{vi_{min}}$. As a result, we can write the ratio of maximum to minimum variable capacitance ΔC_i as

$$\Delta C_i = \frac{C_{par} + C_{vi_{max}}}{C_{par}} \tag{4.24}$$

Since the amount of harvested energy is proportional to ΔC_i [34], it is important to minimize C_{par} in order to increase ΔC_i and the amount of harvested energy. Accordingly, a

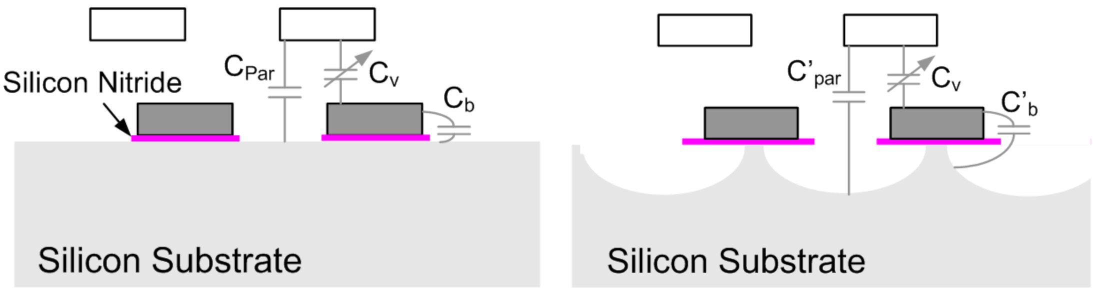

(a) (b)

Figure 4.14: Transducer cross-sections (a) without and (b) with substrate etching.

post processing technique was adopted [57] to wet etch the inter-slab areas on the bottom substrate, as shown in Figure 4.14(b), using 5% tetramethylammonium hydroxide (TMAH).

TMAH etching is an anisotropic process where the etching rate is dependent on the orientation of the holes through the nitride with the (1 1 1) planes having a slower etching rate. Different configurations of the slabs were used including 90°, 45°, and zigzag-like structures. Figure 4.15 shows SEM pictures of the PolyMUMPs chip before and after processing for the different slab configurations. Figure 4.16 shows a profile obtained using Veeco White Light Profilometer of a PolyMUMPs chip with 45° slabs after 90mins of etching using TMAH at 75°C. The results show approximately 43μm of substrate etching between the fingers which is close to the 0.5μm/min etch rate reported by Fouladi et al. [57].

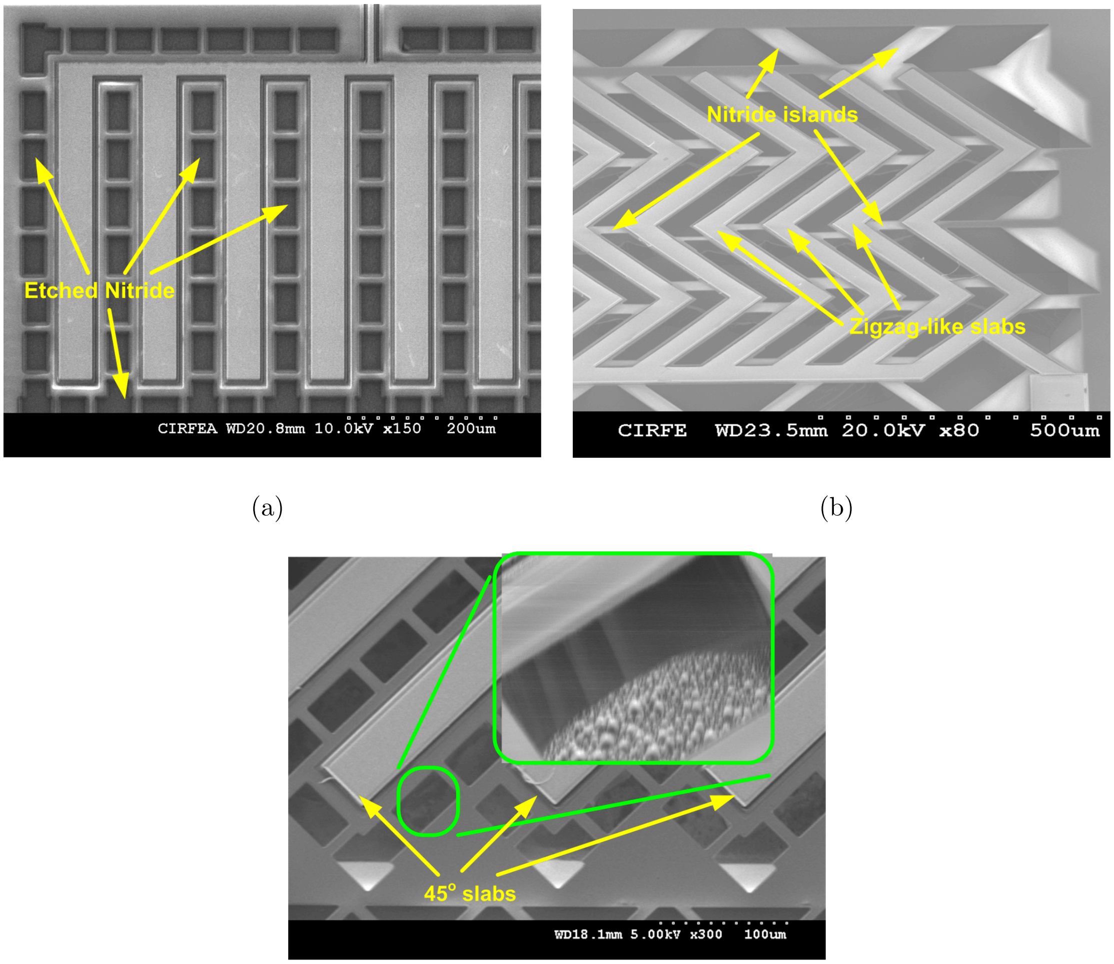

(a) (b)

(c)

Figure 4.15: SEM pictures of TMAH substrate etching: (a) 90° slabs before etching, (b) Zig-zag slabs after etching (c) 45° slabs after etching.

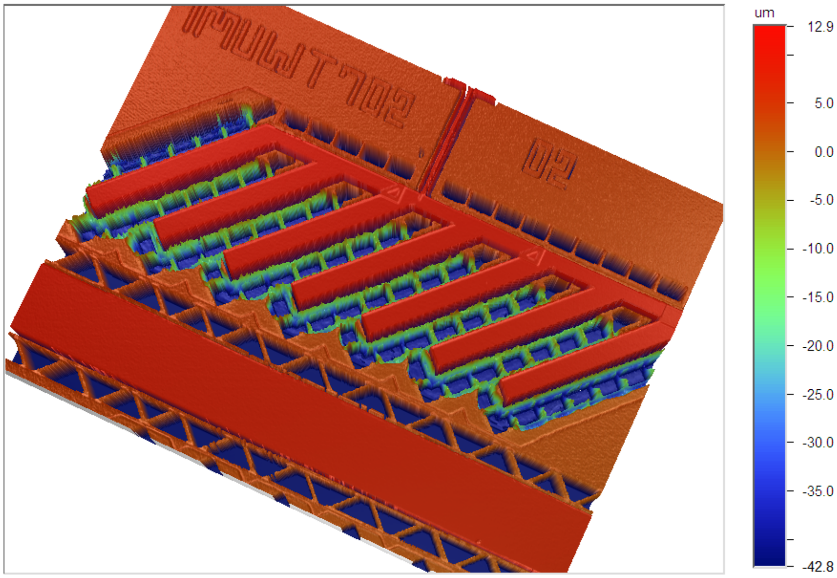

Figure 4.16: Optical profile of the PolyMUMPs chip after 90 mins. etching time.

TMAH etching of silicon produces large amounts of hydrogen bubbles as a reaction byproduct, which causes turbulent motion of the chips during processing. These bubbles led to the frequent destruction of the fine features on the processed chips. We identified a need to redesign the etch holes in the silicon nitride layer and glue the chips to a bigger substrate to control the reaction and protect the fine structures from the flow of hydrogen bubbles, thereby increasing the postprocessing yield.

The PolyMUMPS chip supports the top substrate on four suspension carts. The carts move over the substrate supported by dimples to prevent stiction and guided by guide beams to maintain alignment. Compliant folded-beams were used as guide beams to allow for motion in the x-direction. A layer of trapped silicon oxide was embedded within the beams to alleviate the residual stresses arising from deposition of gold and to in increase the beams thickness, thereby increasing their structural strength. Figure 4.17 shows an SEM of a released suspension cart. The flatness of the beams shown in the figure indicates minimal residual stresses.

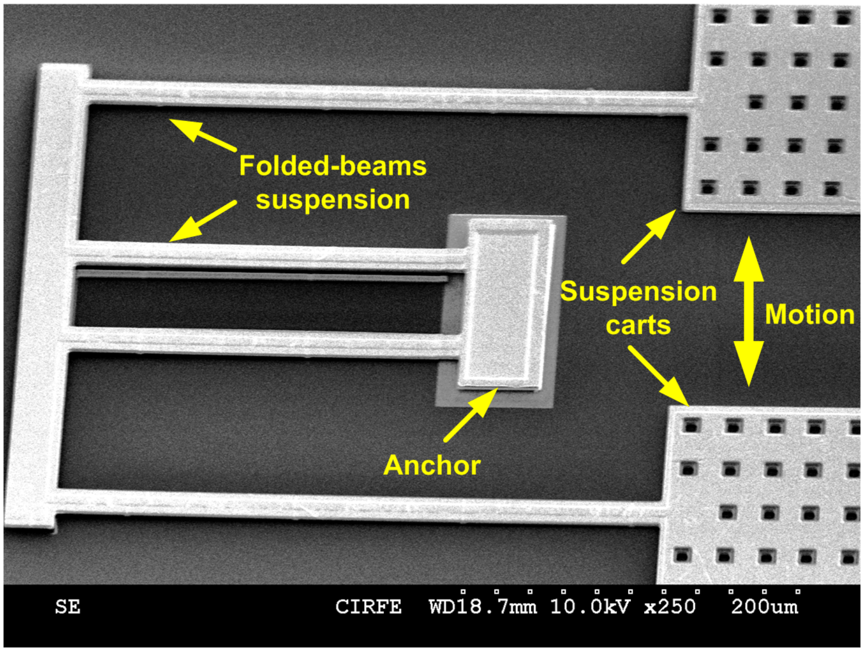

Figure 4.17: Released suspension cart (Half structure).

- **Alumina chip**

This chip contains the top substrate of the harvester. The chip was fabricated using a 2-mask process on an alumina substrate. The alumina substrate was chosen because it is not affected by HF acid during release as well as it has high resistivity, which is suitable for the capacitive electrodes.

Figure 4.18 shows the process flow. The process starts with a RCA cleaned alumina substrate. A 50 nm of chromium is evaporated on the substrate followed by DC sputtering of a 1 μm of gold to have a gold seed-layer for electroplating. The first mask defines the electroplating mold for the harvester support posts. A 5 μm thick negative photoresist layer was patterned using this mask under 1000 rpm spinning and 110 °C soft and hard baking. Gold electroplating of the resulting pattern was done using the Technic 5-Tank Electroplating System. The height of the electroplated post was around 4 μm. Figure 4.19(a)

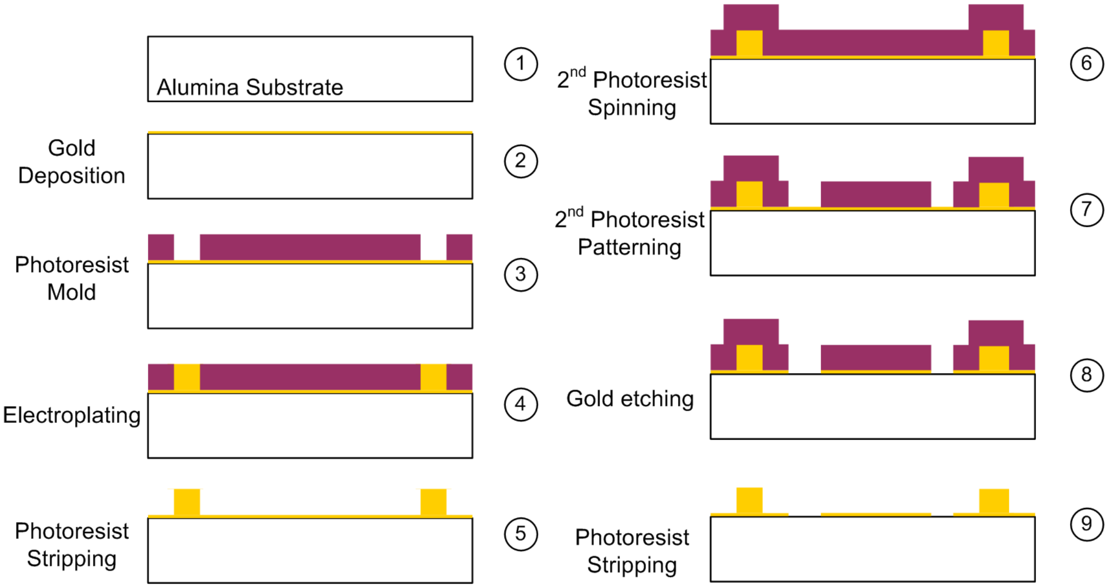

Figure 4.18: Alumina chip fabrication process flow.

shows an SEM picture of the posts after electroplating. The second mask defines the capacitive electrode slabs and bonding pads for bonding with the suspension carts on the PolyMUMPs chip. The photoresist layer patterned using this mask is used as an etch-mask for gold and chromium to obtain the needed pattern.

The PolyMUMPs chip was glued to an assembly substrate using 1 minute Epoxy glue. The two chips were bonded together using the flip-chip technique to insure alignment between the electrodes of the two chips. The bonded system was released using 49% HF acid for 4 minutes followed by CO_2 drying using Tousimis critical point CO_2 dryer. The MPG final size is (2.5 mm × 1.5 mm). Figure 4.19(b) shows a picture of the assembled MPG.

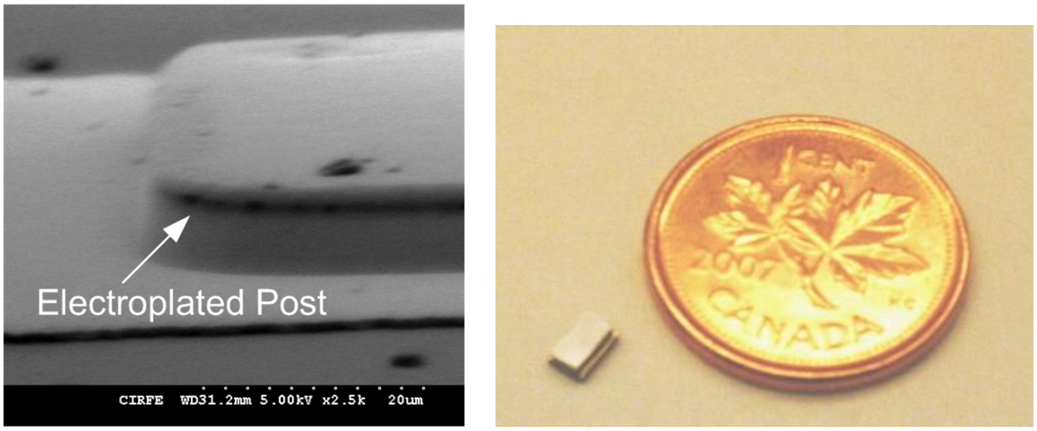

(a) (b)

Figure 4.19: MPG assembly: (a) electroplated posts and (b) assembled MPG.

4.4.4 Test Setup and Experimental Results

A PolyMUMPs chip with 45° slab electrodes was assembled with an alumina chip in the single load configuration, Figure 4.13(b), with C_1 and C_2 varying in-phase. The load resistance was set to 50 MΩ. The silicon nitride layer on the PolyMUMPs chip was charged using a 300V voltage supply. The nitride layer was found to retain the charge for several days and was used as a charge source for the variable capacitors.

The test setup was built on an L-shaped platform. A piezoactuator was used to actuate the platform and an accelerometer was used to measure the acceleration of the platform. Figure 4.20 shows the setup used in testing.

The frequency-response curve of the output voltage was obtained by sweeping the frequency of the platform accelerations between 400 Hz and 2.2 kHz while holding the amplitude constant at $A_\circ = 2\,g$. Figure 4.21 shows the experimental results with one peak observed at 1.1 kHz. The peak (amplitude) of output voltage at this frequency was found to be 65 mV. Table 4.4 compares the test results of the MPG prototype to the most recent comb-finger implementation of the Sterken et al. topology [4]. The results

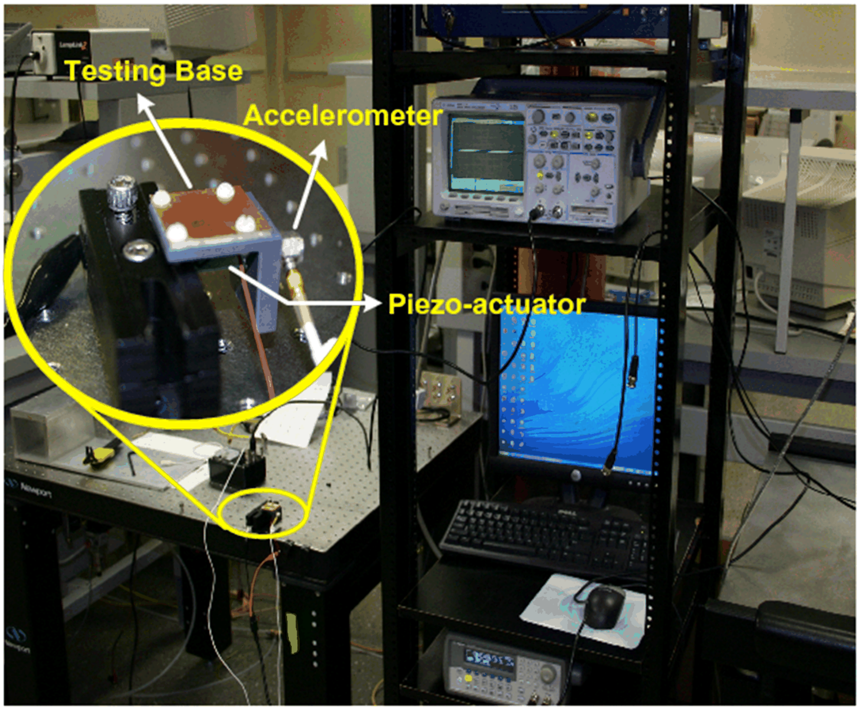

Figure 4.20: Test setup of the MPG prototype.

show that the center frequency of our MPG is 25% lower than that of standard suspension implementation, yet its size is only 12.5% of the comb-finger MPG implemented using standard suspension, therefore, the proposed MPG architecture and suspension technique demonstrate the ability to simultaneously miniaturize and lower the center frequency of electrostatic MPGs.

The output voltage of the MPG prototype is lower than that of the comb-finger MPG. This difference is due to the smaller variable capacitor area, center frequency, and the lower base acceleration used in the experiment. Further improvements in the output voltage can be obtained by deploying arrays of the MPG to increase the capacitance and thus the output voltage and generated power.

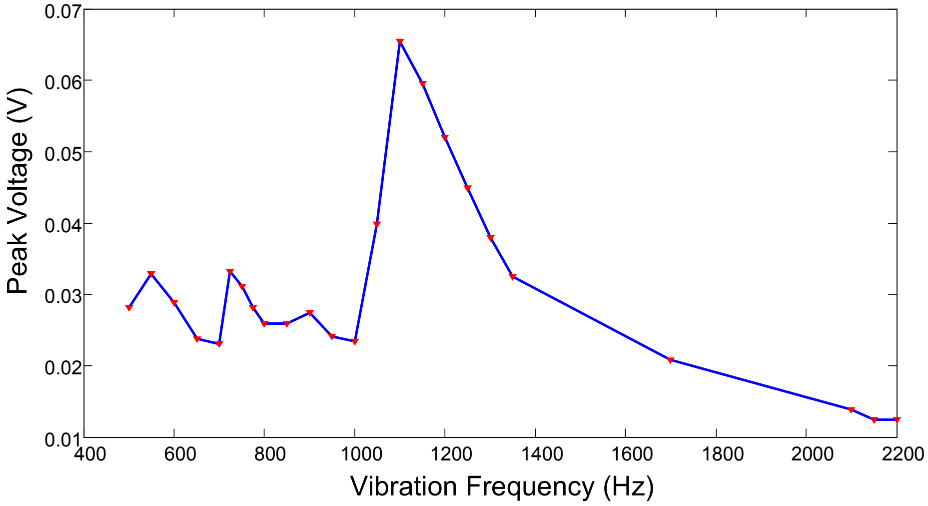

Figure 4.21: Frequency-response curve of the prototype peak output voltage when the base acceleration amplitude was held constant at $A_{\circ} = 2\text{g}$.

Table 4.4: Performance of the interdigitated energy harvester compared to that of Hoffmann et al. [4].

	This work	**Hoffmann et al. [4]**
Size	2.5 mm × 1.5 mm	5 mm × 6 mm
Center frequency	1100 Hz	1460 Hz
Base acceleration	2 g	13 g
Charging source	Charged nitride	50V DC supply
Peak voltage	0.065 V	1.4 V
Load resistance	50 MΩ	560 kΩ

4.5 Springless Vibration Energy Harvesters

Vibration-based energy harvesters (VEHs) collect kinetic energy from the environment through mechanical oscillators. Figure 3.6 illustrated a generic block diagram of a mechanical oscillator. These oscillators can be linear [46], piecewise-linear [48], or nonlinear [58, 59], depending on the restoring force-displacement (stiffness) characteristics of the system. The oscillators achieve maximum displacement and velocity in a frequency band around their natural frequencies.

The natural frequency of the mechanical oscillator, listed in (3.13), was determined from the linear stiffness k_1 and the effective mass of the oscillator m. The natural frequency of the oscillator was matched to the fundamental frequency of environmental vibrations in order to maximize the efficiency of the harvester. Therefore, the mechanical restoring force plays a dual role in VEHs. It provides the dominant component of the stiffness k_1 required to tune the VEH center frequency. It also provides the support/suspension system that the oscillator needs to keep an inertial mass in alignment and function properly.

These roles run into conflict in the design of low-frequency harvesters. In fact, these harvesters are not useful in environments where the fundamental frequency of environmental vibrations is low (<10 Hz). The realization of a mechanical oscillator with a low natural frequency requires a very compliant suspension system and, as a result, experiences a large static deflection x_s due to the inertial mass. At rest, the spring restoring force balances the weight of the mass

$$mg = k_1 x_s \tag{4.25}$$

where g is the acceleration of gravity. The static deflection was obtained from (4.25) by dividing the suspension weight with the linear stiffness k_1. Using (3.13), one can write the static deflection in terms of the system natural frequency $\omega_\circ$ as

$$x_s = \frac{g}{\omega_\circ} \tag{4.26}$$

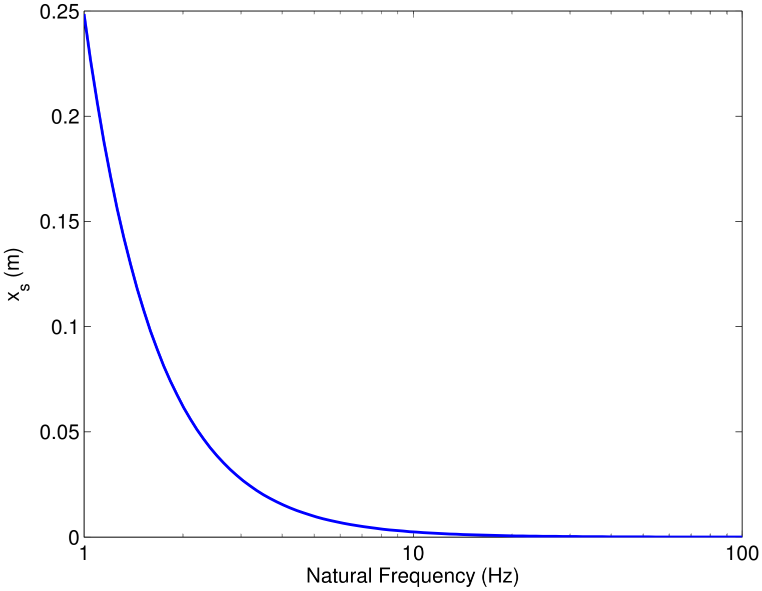

Figure 4.22: Variation of static deflection with the natural frequency.

Figure 4.22 shows the static deflection of the suspension system as a function of the natural frequency. It is clear that below 10 Hz, a highly compliant support/suspension system leads to large static deflection, which makes the harvester impractical due to size and reliability constraints as well as the support system inability to maintain alignment. These limitations set a design floor on the center frequency of the harvesters.

On the other hand, it is impractical to use a harvester with a center frequency ($\geq$ 10 Hz) to harvest energy from low-frequency (<10 Hz) environmental vibrations. The mechanical oscillator in the harvester acts as a bandpass filter. The oscillator response to external excitations (output motion) is large and resonant around the center frequency but small (attenuated/forced) away from the center frequency. While, in theory, it is feasible to collect kinetic energy and convert it to electric energy away from the center frequency of the VEH, in practice the process is highly inefficient, thereby leaving room for improvement. To summarize, there is a need to develop 'springless' harvesters where the support system does not contribute towards the linear stiffness that sets the resonance of the oscillator and therefore the center frequency of the VEH.

4.5.1 Alternate Suspension Approach

The new approach to achieve low-frequency, low-excitation-amplitude VEHs is to eliminate the use of resorting force components (springs) in the support/suspension system. We propose to use a support system made of a guide to support the inertial mass of the VEH. The support system presents no restoring force opposing the carriage motion along the rail and prevents motion in all other directions. The main feature of the new approach is that no mechanical restoring force is allowed to interact with the oscillator throughout its motion. At most, when limiters are used to limit the stroke size, the oscillator comes into contact with mechanical restoring force elements for a brief and intermittent interval during the excitation cycle. Even where it might be desirable to tether the carriage to a particular location along the rail to reduce uncertainty in the oscillator response due to stiction and chaos, the tether stiffness will be negligible since it is not meant to provide support, suspension, or alignment to the VEH mass. Although the last two cases will create a linear stiffness coefficient k_1 in the oscillator, it can be minimized to approach a 0 Hz oscillator natural frequency or to meet a target VEH's center frequency.

The support guide can be straight or circular leading to linear and rotary guide configurations. The linear guide configuration is made up of a carriage and a rail. It allows the carriage to move along the rail while baring any motion in the other directions. The carriage carries the inertial mass and part or all of the electric transducer along the guide. The linear guide system can be implemented and integrated with the VEH using standard off-the-shelf components, custom-built components, or micro-electro-mechanical-systems (MEMS). Various mechanisms can be used to reduce the friction between the carriage and guide including, but not limited to,

- rolling-element bearing,
- lubricated rail, or
- low friction un-lubricated rail.

In all cases, the stroke size will depend on the friction level, excitation level, and the rail length. This arrangement provides support and alignment for the inertial mass and the transducer without contributing to the restoring force of the system.

The new suspension system can be used with any of the transduction mechanisms (piezoelectric, electromagnetic, and electrostatic). Figure 4.23 shows a mechanical model of the new VEH where the restoring spring force was replaced with a friction force. The friction force along the movement direction is approximately constant, and therefore does not contribute to the linear stiffness k_1 of the oscillator, has no effect on the natural frequency of the oscillator, and has no effect on the VEHs' center frequency unlike the ES VEH proposed by Naruse et al. [19] where a linear guide was used to extend the travel range only. Therefore, the center frequency of this VEH can be set arbitrarily low including 0 Hz. As a result, the proposed VEH can harvest energy from environments where vibrations are regular with a low frequency, irregular and chaotic, stochastic, or single event motions, such as impacts and triggered motions occurring at low frequencies. In the next section, the mechanical model of the linear guided VEH is derived for different orientations.

4.5.2 Linear Guide Model

The orientation of linear guided VEHs with respect to gravity affects their operation and thus their mechanical model. Therefore, we make a distinction between planar and vertical (or inclined) implementations of VEHs.

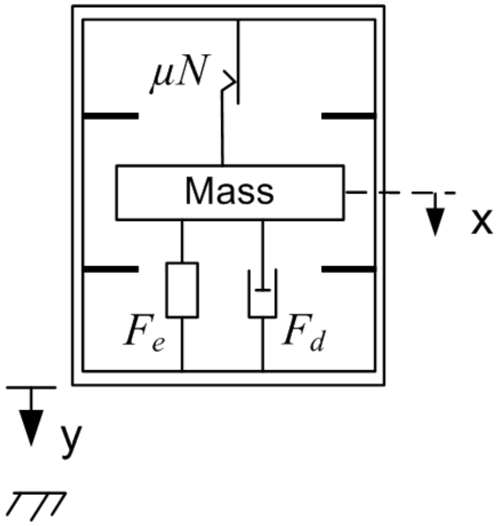

Figure 4.23: Modified VEH mechanical model.

- **Planar Implementation**

The linear guide shown in Figure 4.24 is placed in this case in the horizontal plan. As a result, it will allow the carriage to move along the rail (longitudinal motion along the x-axis) while baring any motion in the other two directions (y and z axes). The equation of motion of the harvester is

$$m\ddot{x} \;=\; F_e - c_m\dot{x} - \mu N\,\mathrm{sgn}(\dot{x}) - ma_y(t) \tag{4.27}$$

where F_e, c_m, μ, N, x, and $a_y(t)$ are the force the electric transducer applies to the inertial mass, viscous damping coefficient, friction coefficient, normal reaction force distributed over the contact surface, the carriage displacement, and the base acceleration, respectively. Since the normal reaction force is $N = mg$, we can divide by the effective mass of the oscillator m to simplify (4.27) to

$$\ddot{x} \;=\; \frac{F_e}{m} - \frac{c_m}{m}\dot{x} - \mu g\,\mathrm{sgn}(\dot{x}) - a_y \tag{4.28}$$

The harvester equation of motion, (4.28), does not contain any mechanical restoring forces. It describes a true free-body motion with a fundamental natural frequency of 0 Hz.

Equation (4.28) also shows that motion occurs, and thereby energy harvesting, as soon as the external excitation level exceeds the summation of the friction force and electric transducer force (for electrostatic and electromagnetic transducers only). So, we can write that the threshold of harvestable base accelerations is

$$a_y \geq \frac{F_e}{m} + \mu g \tag{4.29}$$

Reducing the friction coefficient μ and electric transducer force F_e or increasing the effective mass of the oscillator m will lower the minimum excitation level that will produce carriage motion along the rail and, hence, harvest electric energy. Since we design the mechanical oscillator to minimize friction to very low levels and maximize the inertial mass and since F_e is either unavailable (piezoelectric transducers) or can be set to low values, this configuration allows us to harvest energy from very low amplitude environmental vibrations.

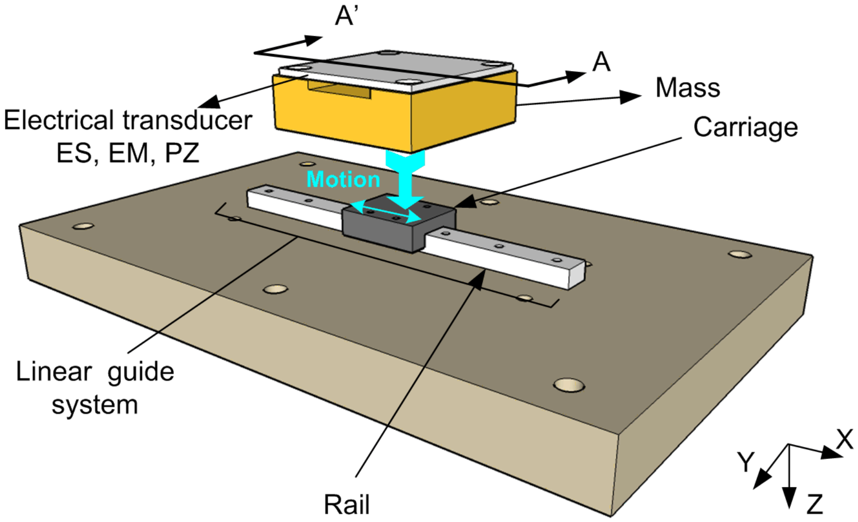

Figure 4.24: Springless planar linear support system.

- **Vertical Implementation**

The linear guide in this case, shown in Figure 4.25, is aligned with the direction of gravity. It allows the carriage to move along the rail (the z-axis) while baring any motion in the other two (x and y) directions. The carriage carries the inertial mass and part or all of the transducer along the guide. The equation of motion of a vertical-aligned harvester is

$$m\ddot{z} \,=\, F_e + mg - c_m\dot{z} - \mu N\,\mathrm{sgn}(\dot{z}) - ma_y(t) \tag{4.30}$$

where z and a_y are the carriage displacement and base acceleration, respectively. The normal force N is equal to the pre-loading force N_c of the carriage $N \,=\, N_c$

Dividing (4.30) by the effective mass of the oscillator m, we obtain

$$\ddot{z} \,=\, \frac{F_e}{m} + g - \frac{c_m}{m}\dot{z} - \frac{\mu N_c}{m}\,\mathrm{sgn}(\dot{z}) - a_y \tag{4.31}$$

Equation (4.31) shows that, in this configuration, the excitation amplitude must exceed the friction, electric transducer forces, and the weight of the oscillator $W \,=\, mg$ before motion occurs and energy is harvested. We can write the threshold of harvestable base accelerations as

$$a_y \geq g \,+\, \frac{F_e}{m} + \frac{\mu N_c}{m} \tag{4.32}$$

While it is possible to minimize the friction coefficient μ and the transducer force F_e and to increase the effective mass m, the gravitational acceleration is essentially constant. So, the base accelerations will have to exceed at least $1\,g$ before we can start harvesting electric energy. Also, because the initial position of this harvester (rest position) is always in contact with the limiter at the bottom of the rail, it is not possible to realize a 0 Hz oscillator natural frequency. As a result, this configuration cannot realize as low “minimum threshold of excitation amplitude” or “center frequency” as the planar configuration. On the other hand, the vertical implementation of the VEH is more suitable for environments where motions are predominantly in the vertical direction.

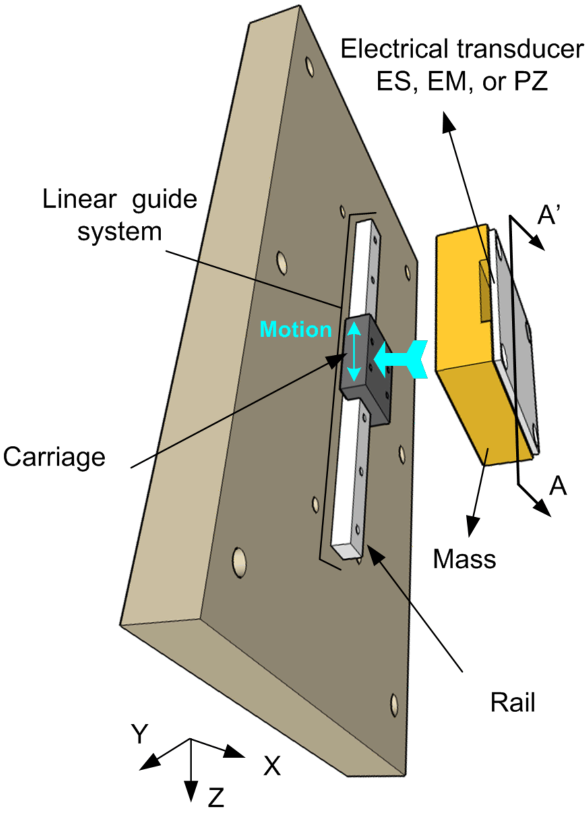

Figure 4.25: Springless vertical linear support system.

- **Inclined Implementation**

The linear guide can also be inclined such that the angle between the rail and the direction of the gravitational acceleration is less than 90°. In this case, the weight of the oscillator is distributed between a constant component that opposes motion directly ($mg\cos\theta$) and a component that opposes motion in proportion to the friction coefficient ($N_w = mg\sin\theta$). We can write the threshold of harvestable base accelerations as

$$a_y \geq g\cos\theta + \frac{F_e}{m} + \frac{\mu N_c}{m} + \mu g\sin\theta \tag{4.33}$$

where N_c is the carriage pre-load. This implementation places a lower threshold of base accelerations though still larger than that of the planar implementation. It also allows for the realization of lower VEH center frequency although it does not allow for true free-body motion or a 0 Hz oscillator natural frequency.

Regardless of the VEH implementation (planar, vertical or inclined), large stroke excitations will cause this system to run off the rail without the use of limiters. To limit the size of motions and keep the harvester size under control, limiters are placed at one or both ends of the rail. The limiters can be

- **Impact-type** a wall, screw, or a protrusion in a wall placed at the end of the rail.
- **Spring-type**
  - a helical spring attached to the wall at the end of the rail and aligned with the longitudinal direction of motion
  - a solid beam or a plate attached on one side or both side of the rail and stretching across the rail at the end point
  - an elastica (highly complaint structure such as a rubber band) supported on both sides of the rail and stretching across the rail at the end point

Figure 4.26 shows schematics of impact, spring-limited, and elastica-limited or beam-limited VEHs. The spring-type limiter has a big advantage in the vertical implementation as they will cancel the effect of the inertial mass weight in (4.31) by compressing the spring at impact and releasing it as kinetic energy at take-off from the limiter. Such a configuration allows low-excitation levels for the vertical operation. In the next subsection, the focus will be given to the planar implementation rather than the vertical and the inclined versions as it works at lower excitation levels.

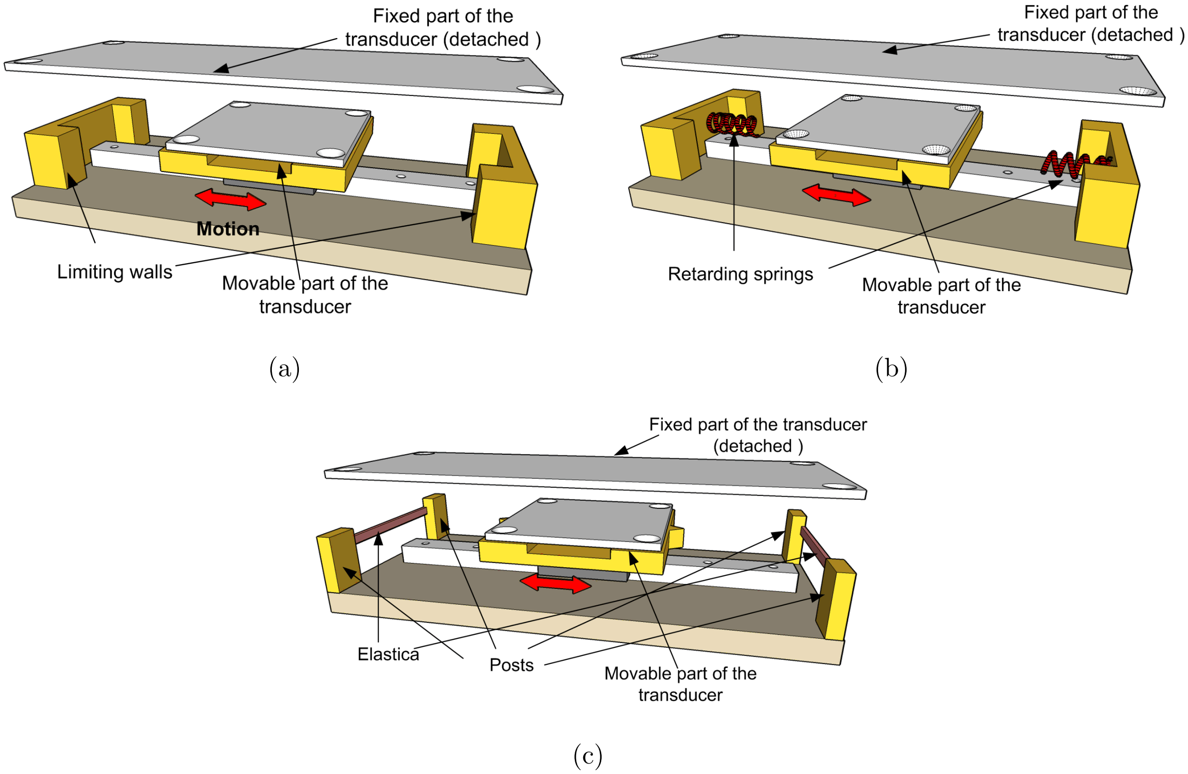

Figure 4.26: Schematics of (a) impact-limited VEHs, (b) spring-limited VEH and (c) elastica-limited VEH.

4.5.3 Springless VEH System Model

The system model of the springless VEHs is derived by combining the model of the transducer with those of the mechanical oscillator and the limiters. An electrostatic interdigitated transducer is suitable for this VEH where a long travel distance is expected. Figure 4.27 shows a cross-section of a planar implementation of the VEH with the interdigitated transducer.

The electrical model for the transducer is obtained from the interdigitated transducer model derived in Section 4.2. Using (4.3), (4.9) and (4.28), we rewrite the system model

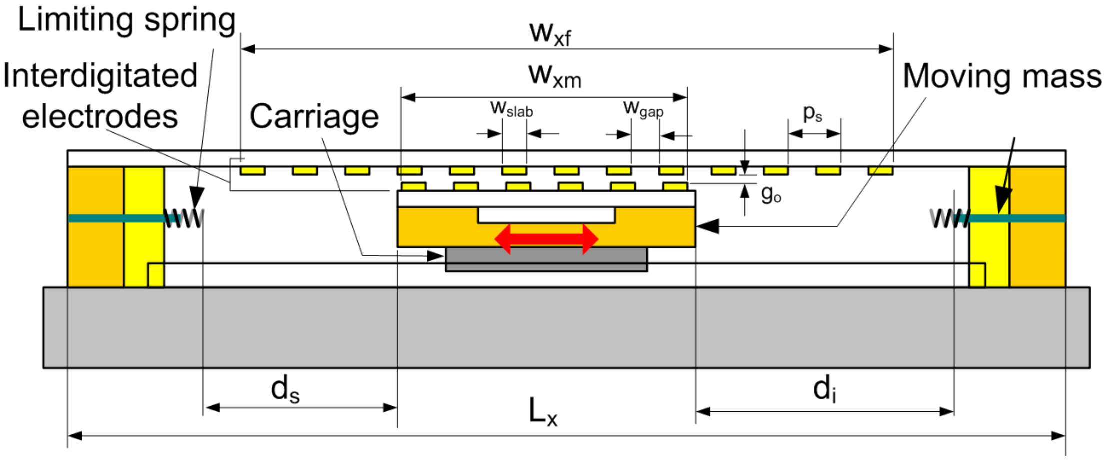

Figure 4.27: Springless VEH's cross-section.

of the springless VEH as

$$\begin{aligned}\dot{q} &= -\frac{q}{RC_\circ\left[C_l s_1\left(\frac{2x}{p_s}\right) + C_d\right]} + \frac{V_{dc}}{R} \\ \ddot{x} &= \frac{C_l s_2\left(\frac{2x}{p_s}\right)}{m\,C_\circ p_s}\,\frac{q^2}{\left[C_l s_1\left(\frac{2x}{p_s}\right) + C_d\right]^2} \\ &\quad - \frac{c_m}{m}\dot{x} - \frac{F_s}{m} - \mu g\,\mathrm{sgn}(\dot{x}) - A_\circ\cos(\Omega t)\end{aligned} \tag{4.34}$$

where R is the external load and V_{dc} is the DC voltage used to charge the transducer. The piecewise functions c_m and F_s describe the damping coefficient and restoring force of the end limiters. For a spring-type limiter installed at the tip of an end-post, the damping coefficient can be written as

$$c_m(x) = \begin{cases} c_f & |x| \le d_s \\ c_s & d_s < |x| \le d_i \\ c_i & |x| \ge d_i \end{cases} \tag{4.35}$$

where c_f, c_s, and c_i are the damping coefficients of the system while the carriage is sliding freely, in contact with the end-spring-limited, and in contact with the end-post, respectively. The restoring force is an odd function $F_s(-x) = -F_s(x)$ defined as

$$F_s(x) = \begin{cases} 0 & 0 < x \leq \ d_s \\ k_s(x - d_s) & \ d_s < x \leq d_i \\ k_i(x - d_i) + k_s(d_i - d_s) & x \geq d_i \end{cases} \tag{4.36}$$

where k_s and k_i are the linear stiffness coefficients of the end-spring and end-post, respectively. The damping coefficient and restoring force are plotted in Figure 4.29 as functions of the carriage displacement.

Equations (4.34) represent a system of nonlinearly coupled differential equations in the variables q and x describing the state of the VEH as the carriage travels along the rail. Numerical solutions of the system equations will be obtained to evaluate the VEH performance. Due to the presence of impact and friction in the system, convergence of these solutions will depend on selection of a proper time step. In the next subsection, a fabricated prototype of the new VEH will be presented.

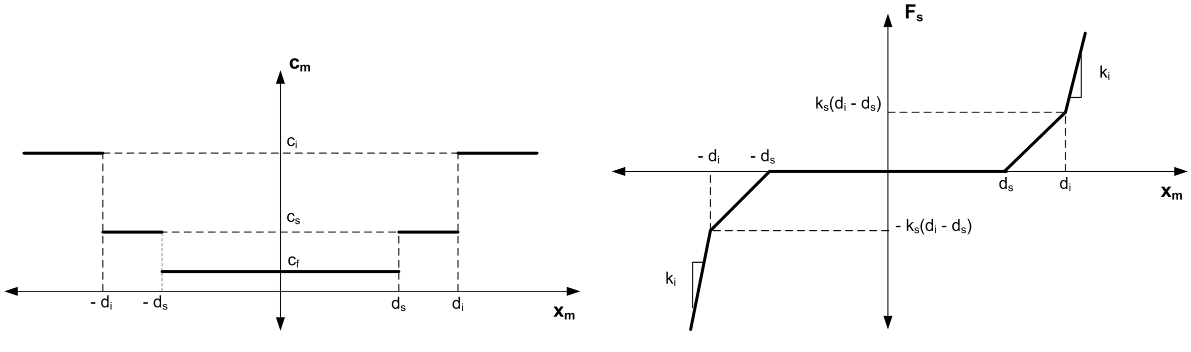

(a) (b)

Figure 4.28: Piecewise function of (a) damping coefficient, and (b) limiting–spring restoring force.

4.5.4 Planar VEH Model Validation

We designed and fabricated a prototype of the planar electrostatic VEH to test the feasibility of the new architecture. The support system was made of a Chieftek Precision Co. (CPC) high-accuracy class linear guide with a 7 mm wide and 10 cm long rail. The carriage was lightly preloaded to minimize friction with the rail and had dimensions of (17 mm × 21.7 mm). The reported coefficient of friction for this linear guide series is $\mu = 0.002 \sim 0.003$. The carriage was loaded with a 266 gm inertial mass. A helical spring was attached, at either end of the rail, to a screw protruding from the wall to limit the carriage motion. Figure 4.29 shows an exploded schematic of an electrostatic VEH prototype.

The gap between the electrodes was not optimized for maximum output power to minimize the possibility of the electrodes coming into contact due to height variation across the electrode surfaces. The nominal gap between the electrodes was set to $g_\circ = 150 \sim 200\,\mu$m. The transducer electrodes were made of PCB boards. The moving electrode width w_m was set to approximately half the fixed electrode width w_f. Figure 4.30 shows a picture of the prototype after assembly. Table 4.5 lists the prototype system parameters.

A schematic of the experimental setup is shown in Figure 4.31. The prototype was placed on the base of the linear motor used to supply base accelerations. It was connected

Table 4.5: Summary of interdigitated harvester's parameters for power optimization.

L_x	114 mm	L_y	50.8 mm
d_i	12.4 mm	d_s	6.5 mm
w_{gap}	0.375 mm	w_{slab}	0.25 mm
$g_\circ$	200 μm	n	59 slabs
w_{xm}	36.6 mm	w_{xf}	74.35 mm

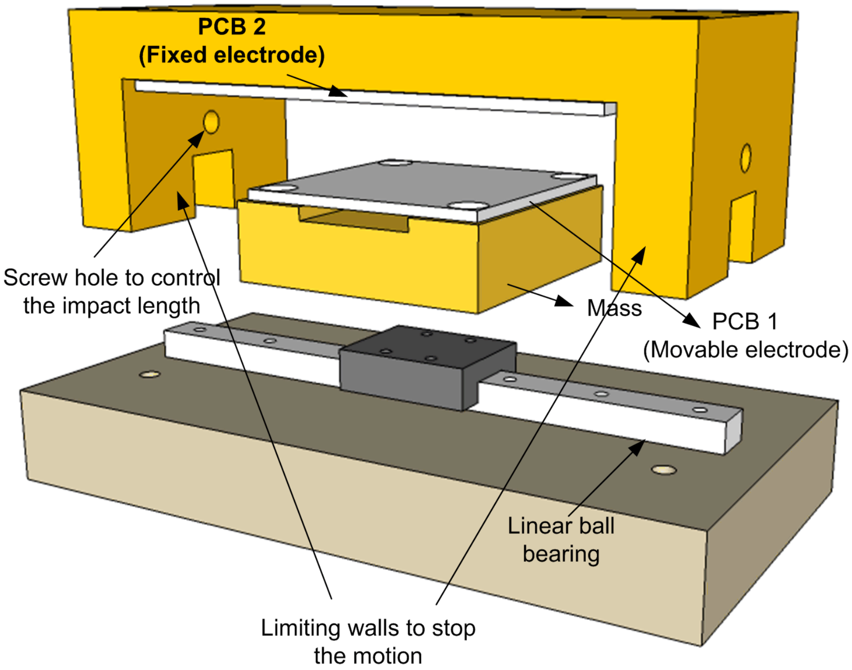

Figure 4.29: Exploded schematic of the prototype.

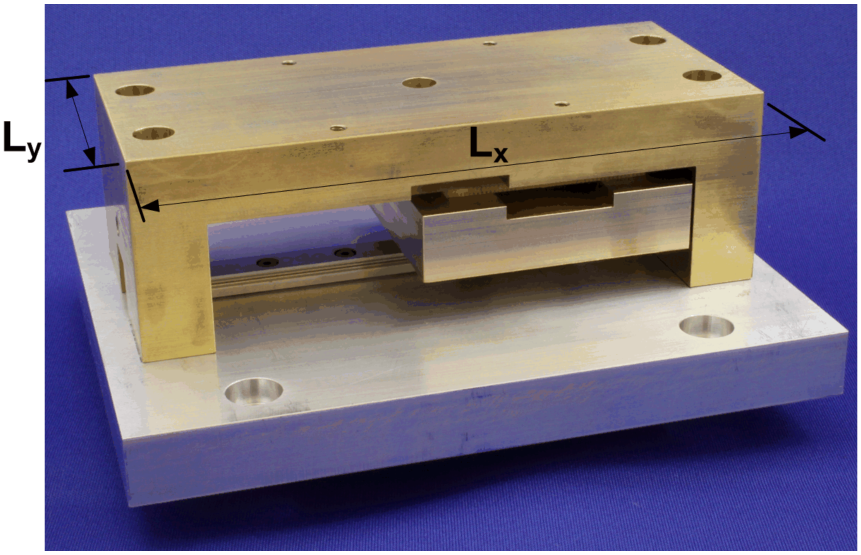

Figure 4.30: Picture of the assembled prototype.

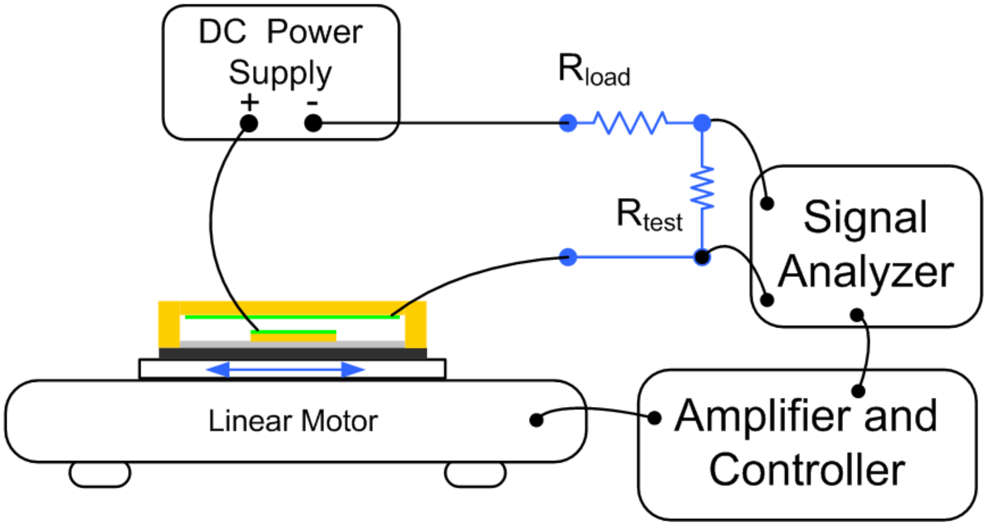

Figure 4.31: The experimental setup for the springless VEH.

electrically to a DC power supply and primary load and test resistors. The test resistor R_{test} was connected in series with the load resistor R_{load} to prevent the loading effect of the signal analyzer input impedance. The signal analyzer was used to measure the root mean square (RMS) of the output voltage across the test resistor.

The DC power supply was set to 300 V and the load resistance was set to $R = 1.1$ MΩ, divided into primary load and test resistances of 1 MΩ and 100 kΩ, respectively. The frequency-response curve of the RMS output voltage was obtained by sweeping the frequency of base accelerations between 1 Hz and 8 Hz while holding the amplitude constant at $A_\circ = 0.2\,g$. One peak was observed in the frequency-response curve, Figure 4.32, at 2 Hz.

The effect of the end-limiters on the frequency-response curve was observed by changing the acceleration amplitude used in the frequency sweep. Figure 4.33 shows the frequency-response curves of the RMS output voltage for $A_\circ = 0.1\,g$, $0.4\,g$, $0.5\,g$, and $1g$. At low excitation levels, $A_\circ = 0.1\,g$, the frequency-response curve has a distinct peak at 2 Hz. As the excitation level is increased, the bandwidth of the VEH becomes wider, 5 Hz, at $A_\circ =$

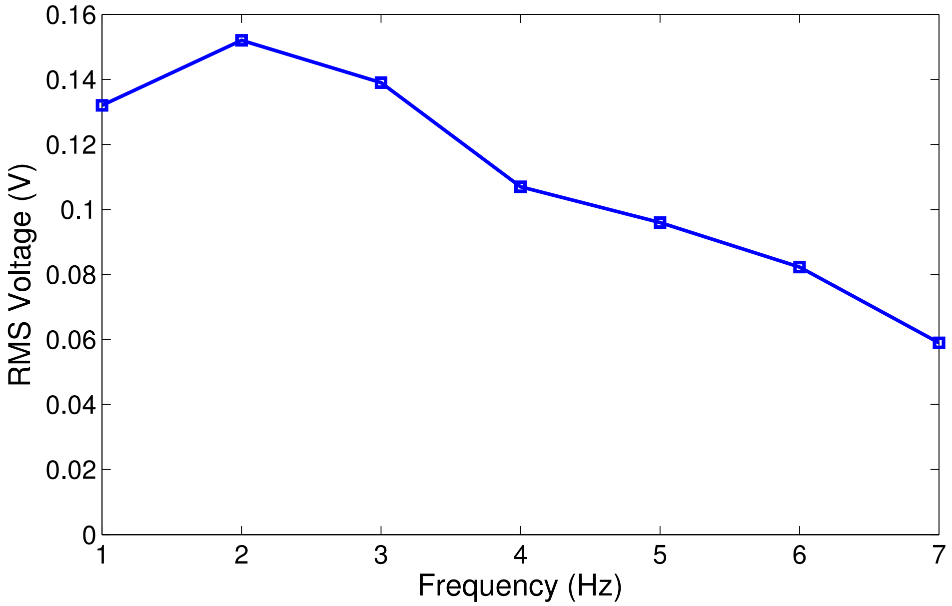

Figure 4.32: The frequency-response curves of the RMS output voltage at 0.2g base acceleration.

$0.2\,g$, and multiple peaks appear at $A_\circ = 0.4\,g$. As the excitation level is increased further, the center frequency shifts to higher values at $A_\circ = 0.5\,g$ and $1\,g$. These results indicate that the carriage contact with the spring had a positive effect on the VEH performance since it increases the bandwidth of the VEH in a manner similar to that encountered in the piecewise-linear MPGs reported by Soliman et al. [48]. However more violent impacts, which can bring the carriage into contact with the screw, reduced the output power, due to larger impact losses, and significantly increases the center frequency of the VEH.

The obtained output voltage was low because of the relatively large capacitor gap and misalignment between the electrodes during the assembly. To operate at smaller gaps, one need the electrodes to be covered with an insulator to guard against the possibility of a short circuit between the electrodes upon impact. Thin film fabrication can also be used to gain better control over the electrode thickness and minimize height variations across the electrode surface. Alignment of the capacitor electrodes can be improved using precision

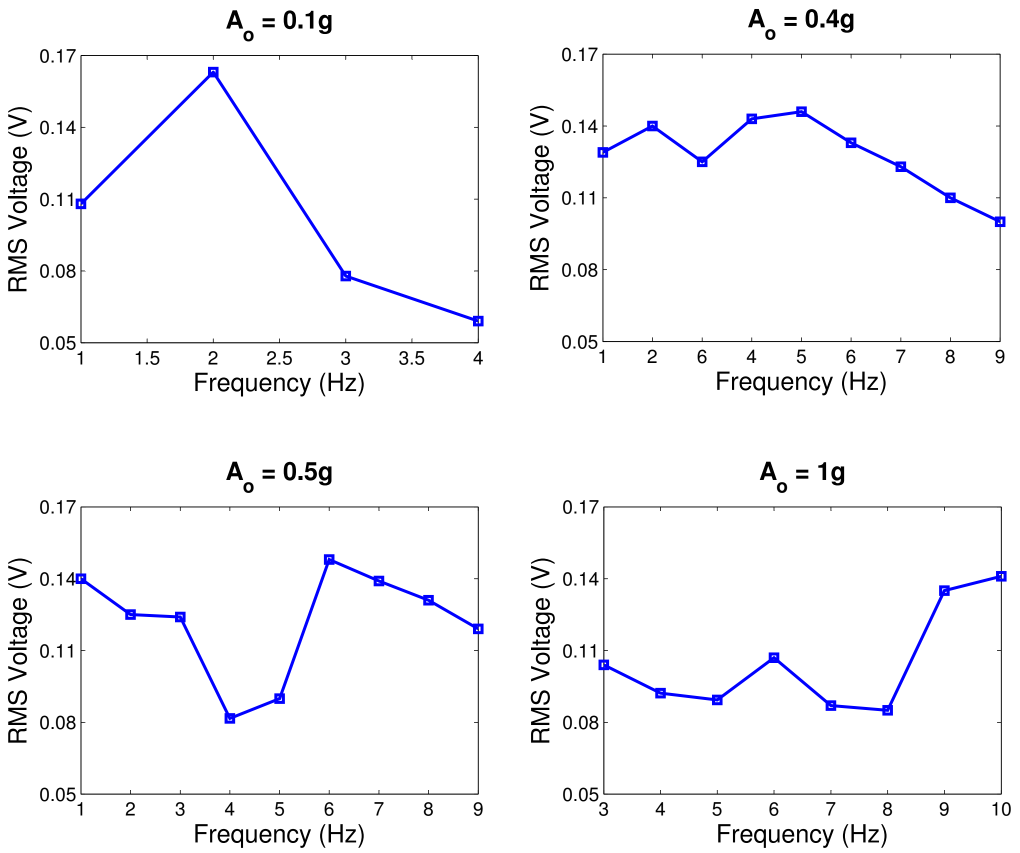

Figure 4.33: The frequency-response curves of the RMS output voltage at four base acceleration amplitudes.

machine design techniques to maximize the capacitance variation with carriage travel.

As a result, a second generation of the springless MPG was implemented in a smaller footprint prototype. Figure 4.34(a) shows a picture of the new prototype in comparison to a 9 V battery. The new prototype size is 5.5 cm × 3 cm × 1.2 cm. The support system was made using Chieftek Precision Co. (CPC) precision class linear guide with a 3 mm wide and 5 cm long rail. The carriage is lightly preloaded to minimize friction with the rail and has dimensions of (11.7 mm × 8 mm).

Precision machine design was used to ensure proper alignment of the bottom and upper electrodes. Dowel pins were used to align the rail of the linear guide with the prototype base. The two end stops were made from Lexan and were similarly aligned using dowel pins. An inertial mass is inserted on the carriage to hold the movable electrode on the carriage. Helical springs were used for spring-limited operation and were installed at both end of the inertial mass. Dowel pins were used to occupy the middle of these springs to prevent their tilt on impact as shown in Figure 4.34(b).

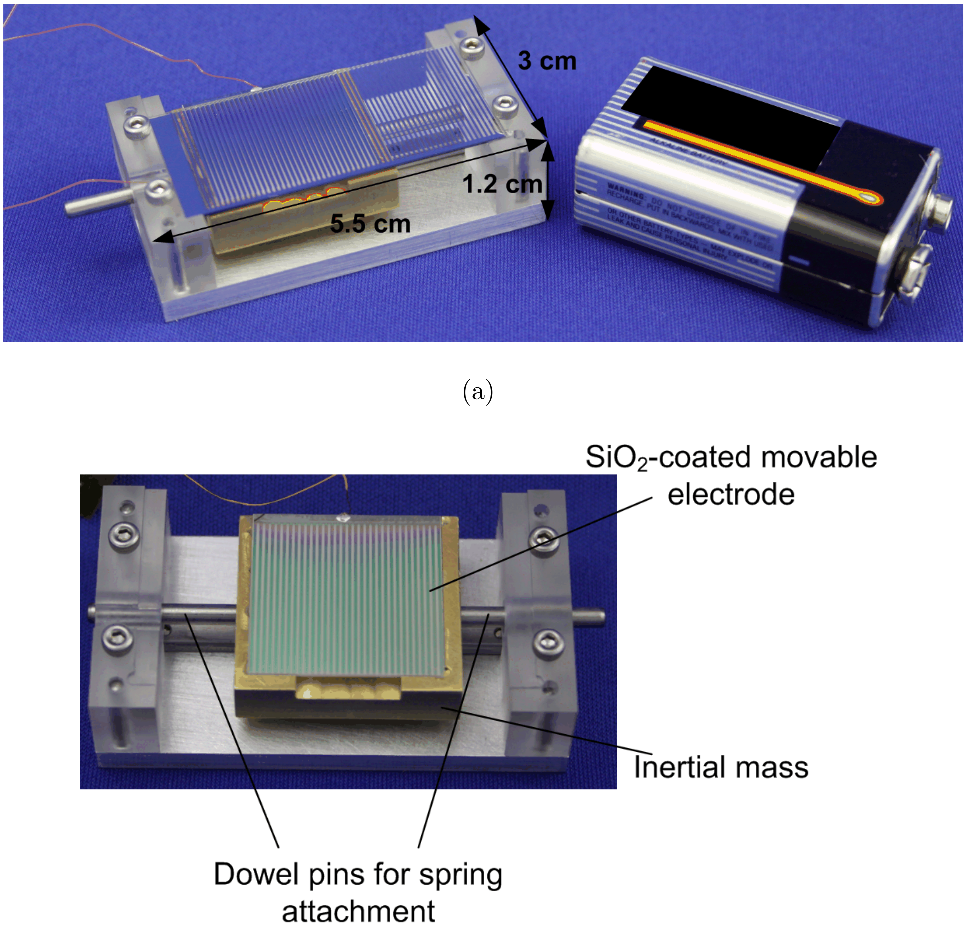

(a)

(b)

Figure 4.34: 2$^{\text{nd}}$ generation springless MPG (a) assembled prototype (b) prototype without top electrode.

The capacitive electrodes were fabricated using thin-film fabrication to ensure good control on the gap. An alumina substrate was used for the bottom (movable) electrode, Figure 4.35(a), whereas a glass substrate was used for the top electrode, Figure 4.35(b). The choice of the glass substrate for the top electrode provides transparent view to ensure the proper alignment of the top and bottom electrodes during assembly. An additional SiO_2 layer was added to the bottom electrode to ensure the electrical isolation between the two electrodes during motion. This layer can be used in the future as an electret-layer.

The testing and validation of the assembled prototype will be carried out in the future work of this dissertation.

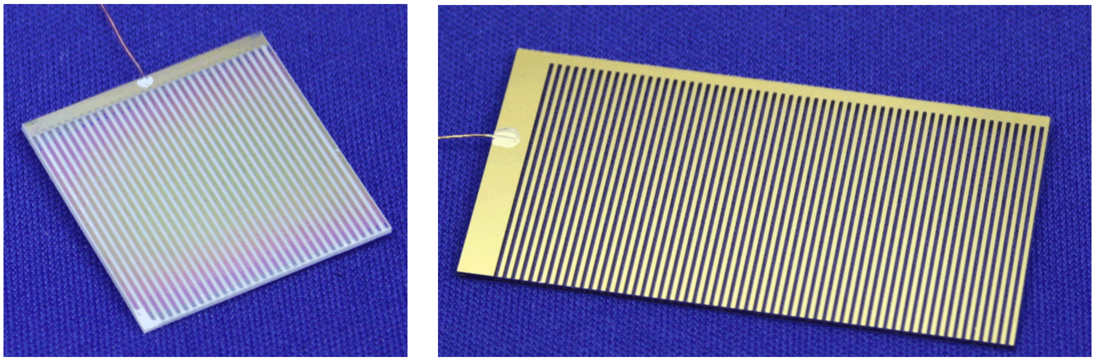

(a) (b)

Figure 4.35: Prototype's electrodes: (a) bottom alumina substrate (b) top glass substrate.

Chapter 5

Electromechanical Coupling in Electrostatic MPGs

5.1 Introduction

Vibration based MPGs are electromechanical systems with a mechanical oscillator that captures and amplifies environmental vibrations and a transducer that transforms these motions into electric energy. The transduction mechanisms can be: electromagnetic, piezoelectric, or electrostatic, as discussed earlier in Chapter 2.

The time constant of the electric subsystem, $\tau_e = RC$ for electrostatic and piezoelectric MPGs and $\tau_e = L/R$ for electromagnetic MPGs, is much smaller than that of the mechanical subsystem $\tau_m \propto 1/\omega$. As a result, the electric subsystem dynamically decouples from the mechanical subsystem, thereby reducing its impact on the mechanical subsystem to a damping force F_e representing the energy extracted by the electric subsystem. Therefore, we assume a linear mechanical oscillator and use the MPG block diagram shown in

Figure 3.6 to write the equation of motion of the MPG as

$$\ddot{x} + 2\zeta_m \omega \dot{x} + \omega^2 x = \frac{F_e}{m} - a_y(t) \tag{5.1}$$

where $x(t)$ is the relative displacement of the inertial mass m with respect to the frame, $\zeta_m = c_m/2m\omega$ is the mechanical damping ratio, $\omega = \sqrt{k_1/m}$ is the natural frequency of the oscillator, and $a_y(t) = A_\circ \cos(\Omega t)$ is the base acceleration.

The nature of electric damping depends on the topology and transduction mechanism of the MPG. In electromagnetic MPGs, the extracted energy is proportional to velocity of the inertial mass and the electric damping behaves as a viscous damping force $\zeta_e = c_e/2m\omega$ [46]. In other MPGs, the electric damping can be constant over a range of motion, thereby acting like Coulomb damping [15]. Electrostatic and piezoelectric MPGs can exhibit either type of damping, depending on the system architecture [39, 60].

The strength of the dynamic coupling between the electrical and mechanical subsystems is not always negligible, rather it depends on the MPG architecture. At one end are electromagnetic MPGs where the dynamics of each subsystem are normally uncoupled, since the MPG inductance is small leading to an electrical time constant much larger than the mechanical time constant ($\tau_e \gg \tau_m$). At the other end are many electrostatic and piezoelectric MPGs where ($\tau_e \approx \tau_m$), the dynamics in this case are tightly coupled, and the subsystems can not be decoupled to study each one alone.

This is particularly the case in switchless (continuous) electrostatic MPGs, which have large load resistance by design to maximize the power output. These MPGs are designed to eliminate the need for switched circuits. Many of them, also, use electrets, quasi-permanently charged dielectrics, to induce charges on the capacitor plates and eliminate the need for initial charge sources. Due to these advantages, significant efforts, including this thesis, have been devoted to developing electret-based electrostatic MPGs in the last five years [16–18, 20, 39, 44, 61]. As a result, it has become important to study the impact of the electromechanical coupling on the dynamics of these MPGs.

In this chapter, we investigate the dynamics of switchless MPGs, identify their optimal operating conditions, and formulate design rules for these MPGs. In Section 5.2, we describe a model of nonlinearly coupled electrostatic MPGs. In Sections 5.3 and 5.4, we develop simplified linear and weakly nonlinear analytical solutions of the system response, compare the results of the analytical solutions, and identify the optimal operating regions of the MPG. In Section 5.5, we validate the obtained nonlinear analytical solution against previously published experimental results and summarizes the chapter.

5.2 System Model

Switchless electrostatic MPGs vary in the number, arrangement, and type of capacitors employed. Sterken et al.'s architecture was one of the early implementations of these MPGs [20]. The circuit topology and original implementation of this MPG were presented earlier in Figures 4.4 and 4.5, respectively. It employs two identical out-of-phase (right and left) variable comb-finger capacitors. The electret layer is embedded below a central capacitor located under the inertial mass m to form the electric equivalent circuit shown in Figure 5.1 and A and B are modeled as two series capacitors. The electret layer and the center capacitor are modeled as a battery of voltage V_{et} and capacitor C_{et}.

The system dynamics are derived by applying Kirchhoff's voltage law to the electric circuit and writing the equation of motion of the inertial mass. The result is

$$\begin{aligned} V_{et} &= R\dot{q}_1 + V_{C_1}(q_1, x) + \frac{q_1 + q_2}{C_{et}} \\ V_{et} &= R\dot{q}_2 + V_{C_2}(q_2, x) + \frac{q_1 + q_2}{C_{et}} \\ m\ddot{x} &= F_2(q_2, x) - F_1(q_1, x) - k_1 x - k_3 x^3 - c_m \dot{x} - m a_y(t) \end{aligned} \tag{5.2}$$

where R is the load resistance, k_1 is the linear spring constant, k_3 is the coefficient of the cubic nonlinearity representing the springs mid-plane stretching, and $a_y(t)$ is a sinusoidal

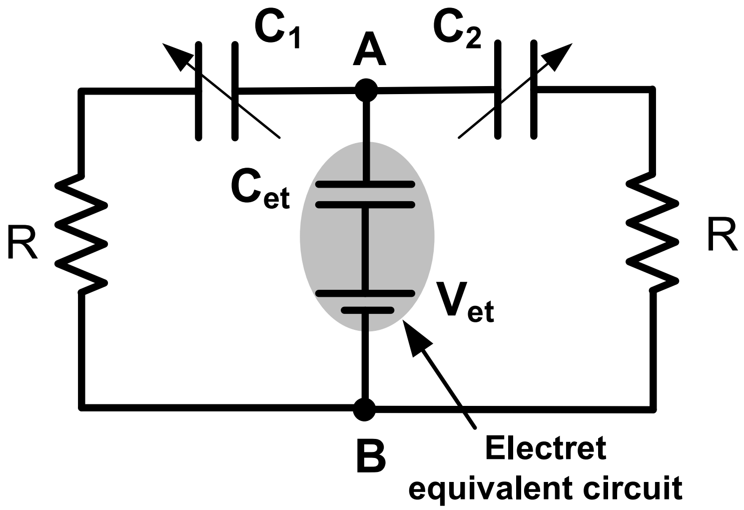

Figure 5.1: An equivalent circuit for Sterken et al. electrostatic MPG taking into consideration the embedded electret.

base acceleration with amplitude $A_\circ$ and frequency Ω. The state variables q_1, q_2, and x correspond to the charge on the right and left variable capacitors $C_1(x)$ and $C_2(x)$, respectively, and the displacement of the inertial mass. The driving efforts are

$$V_{C_i}(q,x) = \frac{q_i(t)}{C_i(x)}\,, \quad F_i(q,x) = \frac{1}{2}\frac{\partial}{\partial x}\Big(\frac{q_i^2(t)}{C_i(x)}\Big) \tag{5.3}$$

The capacitances of the variable capacitors are

$$C_1(x) = C_\circ\Big(1-\frac{x}{h}\Big)\,, \quad C_2(x) = C_\circ\Big(1+\frac{x}{h}\Big) \tag{5.4}$$

where $C_\circ$ is the capacitance of the variable capacitors and h is the finger overlap distance of the unactuated MPG. The initial voltage $V_{C_i}(0) = V_\circ$ is related to the initial charge $q_i(0) = q_\circ$ by $V_\circ = q_\circ/C_\circ$. The voltage across the central capacitor is $V_{C_{et}} = (q_1+q_2)/C_{et}$. Applying Kirchhoff's voltage law to the circuit of the unactuated MPG, we obtain

$$V_\circ \;=\; V_{et}\Big(\frac{C_{et}}{2C_\circ + C_{et}}\Big) \tag{5.5}$$

We introduce the nondimensional variables

$$\hat{t} = t\omega\,,\ \ \hat{q}_1 = \frac{q_1}{q_\circ}\,,\ \ \hat{q}_2 = \frac{q_2}{q_\circ}\,,\ \ \hat{x} = \frac{x}{h} \tag{5.6}$$

into (5.2) and using (5.3)-(5.5), we obtain the nondimensional system of differential equations

$$\begin{aligned}
\dot{\hat{q}}_1 &= -\frac{\omega_e \hat{q}_1}{1-\hat{x}} - \tfrac{1}{2}(I_{et}-\omega_e)(\hat{q}_1+\hat{q}_2) + I_{et} \\
\dot{\hat{q}}_2 &= -\frac{\omega_e \hat{q}_2}{1+\hat{x}} - \tfrac{1}{2}(I_{et}-\omega_e)(\hat{q}_1+\hat{q}_2) + I_{et} \\
\ddot{\hat{x}} &= \tfrac{1}{2}\eta\Big(\frac{\hat{q}_2}{1+\hat{x}}\Big)^2 - \tfrac{1}{2}\eta\Big(\frac{\hat{q}_1}{1-\hat{x}}\Big)^2 - \hat{x} - \kappa\hat{x}^3 - 2\zeta_m\dot{\hat{x}} - \hat{A}_\circ\cos(\hat{\Omega}\hat{t})
\end{aligned} \tag{5.7}$$

where $1/\omega_e$ is the electrical time constant, I_{et} is the decay time constant for the induced charge on the variable capacitors, η is an electrostatic transduction coefficient, $\hat{\Omega}$ is the nondimensional excitation frequency, and κ is the nondimensional coefficient of the cubic nonlinearity. The nondimensional parameters are defined as

$$\begin{gathered}
\omega_e = \frac{1}{RC_\circ\omega}\,,\ \ I_{et} = \frac{V_{et}}{Rq_\circ\omega}\,,\ \ \zeta_m = \frac{c_m}{2m\omega}\,,\ \ \eta = \frac{q_\circ^2}{C_\circ m\omega^2 h^2}\,, \\
\kappa = \frac{k_3 h^2}{k_1}\,,\ \ \hat{A}_\circ = \frac{A_\circ}{h\omega^2}\,,\ \ \hat{\Omega} = \frac{\Omega}{\omega}
\end{gathered} \tag{5.8}$$

We note that the coupling between the electric loops is linear, whereas the electromechanical coupling is nonlinear. Since an analytical solution of this system is not available, we seek an approximate analytical solution using the method of multiple scales. Towards this end, we introduce the linear transformation

$$u_1 = \frac{1}{2}(\hat{q}_1+\hat{q}_2) - 1\,,\quad u_2 = \frac{1}{2}(\hat{q}_1-\hat{q}_2)\,,\quad u_3 = \hat{x}\,,\quad u_4 = \dot{\hat{x}} \tag{5.9}$$

to shift the equilibrium point of the unactuated system from $(q_\circ, q_\circ, 0)$ to the origin. Introducing this transformation into (5.7), expanding the nonlinear terms in Taylor series, and retaining terms up to third-order, we obtain

$$\begin{aligned}
&\dot{u}_1 + I_{et}u_1 = -\omega_e u_2 u_3 - \omega_e {u_3}^2 - \omega_e u_1 {u_3}^2 \\
&\dot{u}_2 + \omega_e u_2 + \omega_e u_3 = -\omega_e u_1 u_3 - \omega_e u_2 {u_3}^2 - \omega_e {u_3}^3 \\
&\dot{u}_3 - u_4 = 0 \\
&\dot{u}_4 + 2\eta u_2 + 2\zeta_m u_4 + (1+2\eta)u_3 = -2\eta u_1 u_2 - 4\eta u_1 u_3 \\
&\quad - 2\eta {u_1}^2 u_3 - 2\eta {u_2}^2 u_3 - 6\eta u_2 u_3^2 - (\kappa + 4\eta){u_3}^3 - \hat{A}_\circ \cos(\hat{\Omega}\hat{t})
\end{aligned} \tag{5.10}$$

Once the velocity u_4 of the inertial mass is found, the nondimensional average electrical power P_e of the MPG can be obtained using the relationship [5]

$$P_e = \frac{1}{T}\int_T \Big(- \frac{\hat{a}_y(\hat{t})}{\eta} u_4 - 2\frac{\zeta_m}{\eta} u_4^2 \Big) d\hat{t} \tag{5.11}$$

where the first and second terms of the integrand are the input power and the dissipated power in the mechanical subsystem, respectively, and $T = 2\pi/\hat{\Omega}$ is the period of base excitations.

5.3 Linear Analysis

The linearized system is obtained from (5.10) by dropping the nonlinear terms. The resulting linear system is

$$\begin{aligned}
\dot{u}_1 &= -I_{et}u_1 \\
\dot{u}_2 &= -\omega_e(u_2 + u_3) \\
\dot{u}_3 &= u_4 \\
\dot{u}_4 &= -2\eta u_2 - (1+2\eta)u_3 - 2\zeta_m u_4 - \hat{A}_\circ \cos(\hat{\Omega}\hat{t})
\end{aligned} \tag{5.12}$$

The first equation in (5.12) is uncoupled from the other equations, indicating that the mean charge on the left and right capacitors $(u_1 + 1)$ will decay exponentially with a decay constant I_{et} towards a constant value $q_\circ$ over long time. As a result, the electromechanical system reduces to the last three equations of (5.12). Solving the reduced linear system in (5.12) for the forced response and substituting the results into equation (5.11), we obtain an expression for the extracted power [5] in the form

$$P_e = \frac{\omega_e \hat{\Omega}^2 \hat{A}_\circ^2}{[\omega_e - (\omega_e + 2\zeta_m)\hat{\Omega}^2]^2 + \hat{\Omega}^2(2\zeta_m\omega_e + \omega_c^2 - \hat{\Omega}^2)^2} \tag{5.13}$$

where $\omega_c = \sqrt{1+2\eta}$. Equation (5.13) was used to plot the peak power $(P_e)_{peak}$ and corresponding nondimensional excitation frequency $\hat{\Omega}_{peak}$ as functions of the electrical frequency ω_e for MPG #1. The MPG parameters are listed in Table 5.1, the mechanical damping was set to $\zeta_m = 0.01$, and the base excitation amplitude was set to $\hat{A}_\circ = 0.01$.

The plots in Figure 5.2 show two distinct domains for the MPG response separated

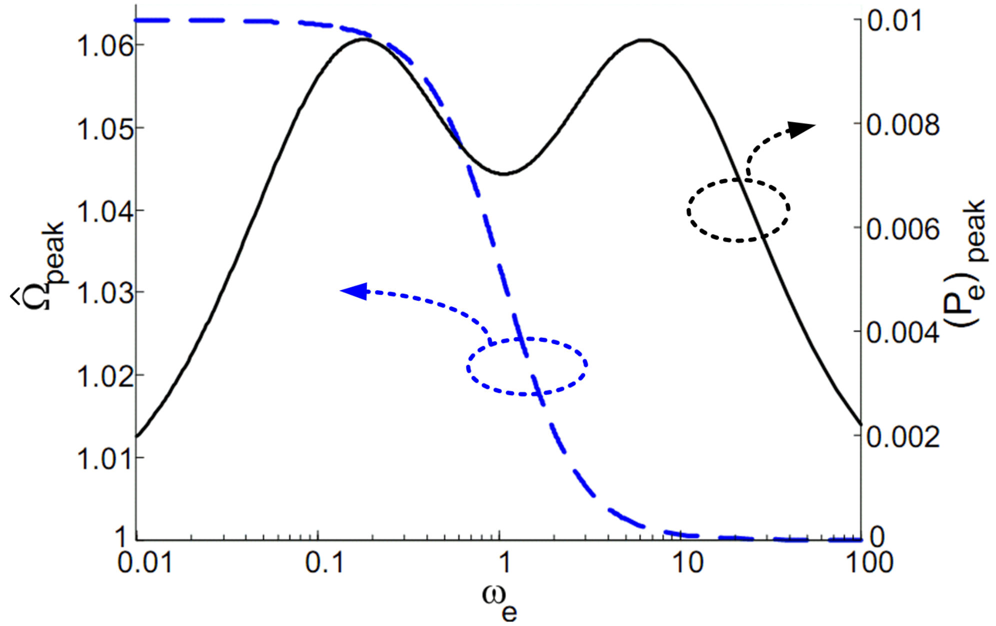

Figure 5.2: Peak output power $(P_e)_{peak}$ (solid black line) and the corresponding nondimensional excitation frequency $\hat{\Omega}_{peak}$ (dashed blue line) as functions of the electrical frequency ω_e.

Table 5.1: Dimensions and Properties of MPG #1 [5].

m	$1.212\,\mu$kg	h	140.0μm
$C_\circ$	19.37 pF	C_{et}	16.80 pF
V_{et}	150 V	η	0.065
k_1	31.27 N/m	k_3	0

by $\omega_e = 1$ where the electrical frequency is perfectly tuned with the uncoupled oscillator natural frequency. In the fast domain ($\omega_e > 1$), the optimal peak power occurs as the excitation frequency approaches the natural frequency of the uncoupled oscillator $\hat{\Omega} \to 1$. In the slow domain ($\omega_e < 1$), the optimal peak power occurs as $\hat{\Omega} \to \omega_c$ where ω_c is the nondimensional natural frequency of the coupled oscillator. The existence of two optimal operating points was observed by Sterken et al. [20] in switchless electrostatic MPGs and by DuToit et al. [1] in piezoelectric MPGs. In the following, we present an overarching system dynamics framework to explain and optimize the two peaks simultaneously and to use them to design wideband MPGs.

5.3.1 Fast MPG

In the fast domain ($\omega_e > 1$), the electrical subsystem approaches a short circuit as $\omega_e \to \infty$. The second of equations (5.12) can, therefore, be used to write

$$u_2 = -\frac{\dot{u}_2}{\omega_e} - u_3 \quad \text{and} \quad \dot{u}_2 \approx -\dot{u}_3$$

These relations can then be used to eliminate u_2 from the fourth equation in (5.12) and the system dynamics reduce to

$$\ddot{u}_3 = -u_3 - 2\big(\zeta_m + \frac{\eta}{\omega_e}\big)\dot{u}_3 - \hat{A}_\circ \cos(\hat{\Omega}\hat{t}) \tag{5.14}$$

Therefore, the MPG reduces in this case to an uncoupled viscous-damped MPG with the current in the electric subsystem enslaved to the velocity of the inertial mass. The center frequency of the MPG is identical to that of the uncoupled mechanical oscillator $\omega = 1$ and the additional electrical damping ratio is

$$\zeta_e = \frac{\eta}{\omega_e} \tag{5.15}$$

Solving (5.14) and substituting the solution into (5.11), we express the extracted power as

$$P_e = \frac{\frac{\hat{\Omega}^2}{\omega_e}\hat{A}_\circ^2}{(1-\hat{\Omega}^2)^2 + 4\hat{\Omega}^2\left(\zeta_m + \frac{\eta}{\omega_e}\right)^2} \tag{5.16}$$

For a given MPG, the peak extracted power occurs when the excitation frequency is equal to the natural frequency of the MPG ($\hat{\Omega} = 1$) and hence

$$(P_e)_{peak} = \frac{\hat{A}_\circ^2}{4\omega_e\left(\zeta_m + \frac{\eta}{\omega_e}\right)^2} \tag{5.17}$$

The same expression can be obtained from (5.13) by noting that for a fast MPG, $\frac{\zeta_m}{\omega_e} \to 0$. The electrical frequency ω_e corresponding to optimal peak power (i.e., the load resistance R required to obtain maximum $(P_e)_{peak}$ for a fast MPG) can be obtained by setting the derivative of the peak power with respect to ω_e equal to zero and obtaining

$$(\omega_e)_{opt} = \frac{\eta}{\zeta_m} \tag{5.18}$$

Comparing (5.18) to (5.17), we conclude that the optimal peak power is extracted when the electrical damping and the mechanical damping are equal ($\zeta_m = \zeta_e$). This is the traditionally studied optimal operating point. Similar results to those obtained here were reported by Williams and Yates [46] and others [5].

5.3.2 Slow MPG

In the slow domain ($\omega_e < 1$), the electrical subsystem approaches an open circuit as $\omega_e \to 0$ and the second equation in (5.12) can be used to write

$$\dot{u}_2 \approx 0 \quad \Rightarrow \quad u_2 \approx q_c$$

where q_c is a constant charge difference between the left and right variable capacitors. As a result, the system dynamics reduce to

$$\ddot{u}_3 = -2\eta q_c - \omega_c^2 u_3 - 2\zeta_m \dot{u}_3 - \hat{A}_\circ \cos(\hat{\Omega}\hat{t}) \tag{5.19}$$

As the MPG moves towards one of the variable capacitors, it builds charge on it and drains charge from the opposite capacitor. The difference between their electrostatic fields produces a net quasi-static (Coulomb damping) force and a hardening linear spring effect on the oscillator, thereby shifting its coupled natural frequency to ω_c.

For a given MPG, the peak extracted power occurs when the excitation frequency is equal to the natural frequency of the MPG ($\hat{\Omega} = \omega_c$). Substituting this value into (5.13), scaling the electrical frequency and mechanical damping at $\epsilon\omega_e$ and $\epsilon\zeta_m$, and dropping terms of order $O(\epsilon^4)$ and higher, we obtain the following expression for the peak extracted power for a slow MPG in the form:

$$(P_e)_{peak} = \frac{\omega_e \omega_c^2 \hat{A}_\circ^2}{4\left(\zeta_m \omega_c^2 + \eta\omega_e\right)^2} \tag{5.20}$$

The electrical frequency ω_e corresponding to the optimal peak power for a slow MPG can be found from (5.20) as

$$(\omega_e)_{opt} = \frac{\zeta_m}{\eta}\omega_c^2 \tag{5.21}$$

Figure 5.3 compares the peak power found using the linear model, (5.13), with those calculated using the simplified linear models, (5.17) and (5.20), for MPG #1. Each of the simplified models approximates the system response well in its own domain but they both fail in the mixed domain ($\omega_e \approx 1$).

Comparing (5.18) and (5.21), we conclude that as $\frac{\eta}{\zeta_m} \to 1$, the locations of optimal peak power in the slow and fast domain approach each other. Figure 5.4 shows the peak output power for MPG #2 which was obtained from MPG #1 by reducing the electromechanical coupling coefficient to $\eta = 0.02$, thereby setting $\frac{\eta}{\zeta_m} = 2$. The locations of the optimal

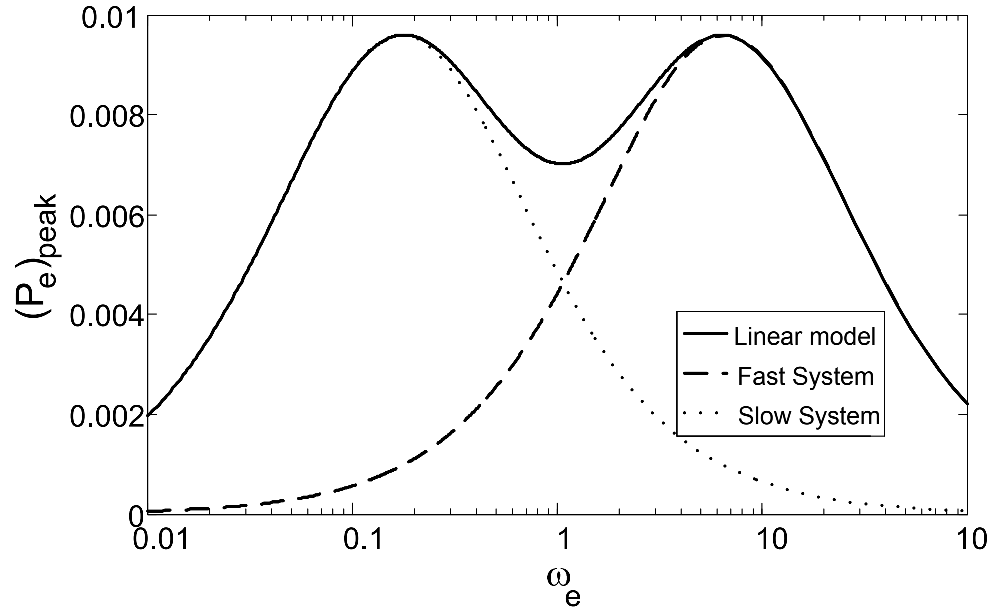

Figure 5.3: Peak output power obtained using the linear model and the simplified models.

peak output power approach each other and merge into a single peak centered at $\omega_e = 1$ and stretching over a wider band of excitation frequencies $\hat{\Omega} = [1, \omega_c]$. We conclude that it is necessary to maintain $\frac{\eta}{\zeta_m} \approx 1$ to optimally tune switchless electrostatic MPGs to harvest energy over a wideband of excitation frequencies. The power output can be further enhanced by setting the load resistance such that $\omega_e \in [\frac{\eta}{\zeta_m}, \frac{\zeta_m}{\eta}\omega_c^2]$

Although the linear model offers significant insights into the MPG response, it breaks down in the slow and mixed domains. Figure 5.5 shows the peak output power $(P_e)_{peak}$ and the corresponding excitation frequency $\hat{\Omega}_{peak}$ for MPG #2 and a base excitation of $\hat{A}_\circ = 0.02$. The figure compares two sets of results obtained using numerical integration of the full model, (5.7), and analytical solution of the linear model, (5.12). The numerical solution verifies the wideband operation for MPG behavior, and it also shows that the linear model underestimates the excitation frequency corresponding to peak power $\hat{\Omega}_{peak}$ in the slow domain. We found that, for excitation amplitudes $\hat{A}_\circ \geq 0.01$, frequency errors were

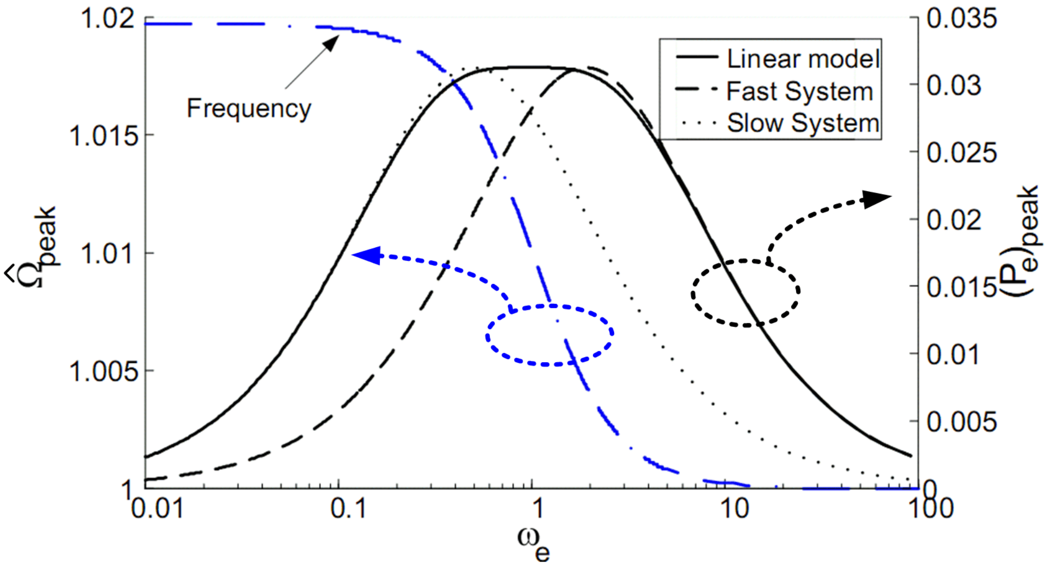

Figure 5.4: Peak output power and the corresponding excitation frequency for a wideband MPG.

$\geq 2\%$ in the slow and mixed domains. As a result, the error in the peak excitation frequency $\hat{\Omega}_{peak}$ calculated using the linear model was large enough for the excitations to completely miss out the energy harvesting bandwidth even for a wideband MPG. These results are in agreement with the findings of Peano and co-workers [5, 62] and our observation above that the simplifying assumption used to uncouple the electric and mechanical subsystems leads to erroneous conclusions about the optimal operating conditions when ($\tau_e \approx \tau_m$). These results make the need for a nonlinear model of electrostatic MPGs evident.

5.4 Nonlinear Analysis

A uniformly consistent second-order approximation of the MPG response is developed using the method of multiple scales [63]. We assume a solution of the form

$$u_i(t) = \epsilon u_{i,1}(T_\circ, T_1, T_2) + \epsilon^2 u_{i,2}(T_\circ, T_1, T_2) + \epsilon^3 u_{i,3}(T_\circ, T_1, T_2) + \cdots \qquad i = 1, 2, 3, 4 \quad (5.22)$$

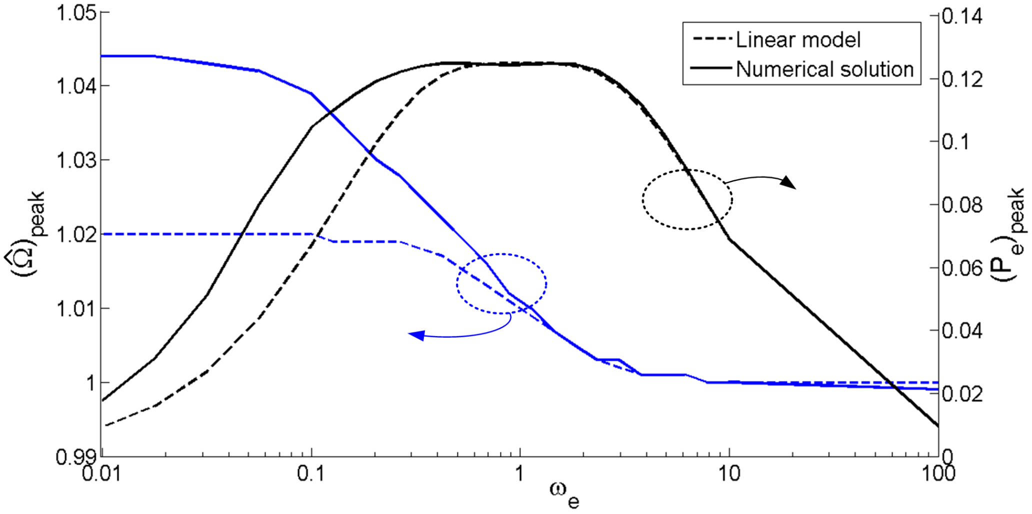

Figure 5.5: Peak output power $(P_e)_{peak}$ (black lines) and the corresponding excitation frequency $\hat{\Omega}_{peak}$ (blue lines) obtained from the full and linear models for $\hat{A}_\circ = 0.02$.

where ϵ is a small bookkeeping parameter and the time scales are $T_\circ = t$, $T_1 = \epsilon t$, and $T_2 = \epsilon^2 t$. In order to balance the effects of the nonlinearity, damping, and base excitation, we scale the electric damping as $\epsilon^2 \eta u_2$, the mechanical damping as $\epsilon^2 \zeta_m u_3$, the forcing as $\epsilon^3 \hat{A}_\circ$, and drop the higher-order squeeze-film damping terms. Restricting our interest to the mixed domain region, we write the nondimensional excitation frequency as

$$\hat{\Omega} = \omega_c + \epsilon^2 \sigma$$

where σ is the detuning between the excitation frequency and the natural frequency of the coupled oscillator. Substituting (5.22) into (5.10) and equating coefficients of like powers of ϵ, we obtain the following hierarchy of problems:

Order ϵ

$$\begin{aligned}
&D_\circ u_{1,1} + I_{et} u_{1,1} = 0 \\
&D_\circ u_{2,1} + \omega_e u_{2,1} + \omega_e u_{3,1} = 0 \\
&D_\circ u_{3,1} - u_{4,1} = 0 \\
&D_\circ u_{4,1} + \omega_c^2 u_{3,1} = 0
\end{aligned} \tag{5.23}$$

Order ϵ^2

$$\begin{aligned}
&D_\circ u_{1,2} + I_{et} u_{1,2} = -D_1 u_{1,1} - \omega_e u_{2,1} u_{3,1} - \omega_e u_{3,1}^2 \\
&D_\circ u_{2,2} + \omega_e u_{2,2} + \omega_e u_{3,2} = -D_1 u_{2,1} - \omega_e u_{1,1} u_{3,1} \\
&D_\circ u_{3,2} - u_{4,2} = -D_1 u_{3,1} \\
&D_\circ u_{4,2} + \omega_c^2 u_{3,2} = -D_1 u_{4,1} - 2\eta u_{1,1} u_{2,1} - 4\eta u_{1,1} u_{3,1}
\end{aligned} \tag{5.24}$$

Order ϵ^3

$$\begin{aligned}
&D_\circ u_{1,3} + I_{et} u_{1,3} = - D_1 u_{1,2} - D_2 u_{1,1} - \omega_e u_{2,2} u_{3,1} - \omega_e u_{1,1} u_{3,1}^2 - \omega_e u_{2,1} u_{3,2} - 2\omega_e u_{3,1} u_{3,2} \\
&D_\circ u_{2,3} + \omega_e u_{2,3} + \omega_e u_{3,3} = -D_1 u_{2,2} - D_2 u_{2,1} \omega_e u_{1,2} u_{3,1} - \omega_e u_{2,1} u_{3,1}^2 - \omega_e u_{3,1}^3 - \omega_e u_{1,1} u_{3,2} \\
&D_\circ u_{3,3} - u_{4,3} = -D_1 u_{3,2} - D_2 u_{3,1} \\
&D_\circ u_{4,3} + \omega_c^2 u_{3,3} = -\hat{A}_\circ \cos(\omega_c T_\circ + \sigma T_2) - 2\eta u_{2,1} - 2\zeta_m u_{4,1} - D_1 u_{4,2} - D_2 u_{4,1} - 2\eta u_{1,1} u_{2,2} - 2\eta u_{1,2} u_{2,1} \\
&\qquad - 4\eta u_{1,1} u_{3,2} - 4\eta u_{1,2} u_{3,1} - 2\eta u_{1,1}^2 u_{3,1} - 2\eta u_{2,1}^2 u_{3,1} - 6\eta u_{2,1} u_{3,1}^2 - (4\eta + \kappa) u_{3,1}^3
\end{aligned} \tag{5.25}$$

where $D_i = \frac{\partial}{\partial T_i}$.

The first-order system is a homogeneous linear system. The eigenvalues of this system were found to be

$$\lambda_1 = -I_{et}\,, \quad \lambda_2 = -\omega_e\,, \quad \lambda_{3,4} = \pm i\sqrt{1 + 2\eta} \tag{5.26}$$

Therefore, the first-order system solution can be expressed using the eigenvalues and eigenvectors of the system as

$$\begin{aligned} u_{1,1} &= B_1(T_1,T_2)e^{\lambda_1 T_\circ} \\ u_{2,1} &= B_2(T_1,T_2)\, e^{\lambda_2 T_\circ} - B_3(T_1,T_2)\frac{\lambda_2 e^{\lambda_3 T_\circ}}{(\lambda_2+\lambda_3)\lambda_3} + \text{cc} \\ u_{3,1} &= B_3(T_1,T_2)\frac{1}{\lambda_3}e^{\lambda_3 T_\circ} + \text{cc} \\ u_{4,1} &= B_3(T_1,T_2)e^{T_\circ \lambda_3} + \text{cc} \end{aligned} \tag{5.27}$$

where the B_i are functions of the slow time-scales to be determined by imposing the solvability condition in the higher-order problems and cc stands for the complex conjugate of the preceding term.

Substituting (5.27) into (5.24), we find that the B_i are independent of T_1 and evaluate the particular solution to the second-order system as

$$\begin{aligned} u_{1,2} &= B_2 e^{\lambda_2 T_\circ}(p_1 B_3 e^{T_\circ \lambda_3} + \text{cc}) + p_2 B_3^2 e^{2\lambda_3 T_\circ} + \text{cc} + r_1 B_3 \bar{B}_3 \\ u_{2,2} &= B_1 e^{\lambda_1 T_\circ}(r_2 B_2 e^{\lambda_2 T_\circ} + p_3 B_3 e^{\lambda_3 T_\circ} + \text{cc}) \\ u_{3,2} &= B_1 e^{\lambda_1 T_\circ}(r_3 B_2 e^{\lambda_2 T_\circ} + p_4 B_3 e^{\lambda_3 T_\circ} + \text{cc}) \\ u_{4,2} &= B_1 e^{\lambda_1 T_\circ}(r_4 B_2 e^{\lambda_2 T_\circ} + p_5 B_3 e^{\lambda_3 T_\circ} + \text{cc}) \end{aligned} \tag{5.28}$$

where the p_i are complex-valued constants, r_i are real-valued constants, and the overbar denotes the complex conjugate.

Substituting the first-order and second-order solutions, (5.27) and (5.28), into the third-order system (5.25), we determine the modulation equations governing the evolution of B_i by enforcing the solvibility condition on the third-order system. We use the polar transformation $B_3(T_2) = \frac{1}{2}a(T_2)e^{i\theta(T_2)}$ to simplify the equations and obtain

$$\begin{aligned} B_1' &= s_1 B_1 a^2 \\ B_2' &= 2\eta s_2 B_2 + s_3 B_2 a^2 \\ a' &= -(\zeta + \eta s_2)a + \eta s_4 a^3 - \frac{1}{2}\hat{A}_\circ \cos\gamma \\ a\gamma' &= -(\sigma + \eta s_5)a + s_6 a^3 + \frac{1}{2}\hat{A}_\circ \sin\gamma \end{aligned} \tag{5.29}$$

where the prime denotes the derivative with respect to T_2, $\gamma = \sigma - \theta$, and the coefficients s_i are

$$
\begin{aligned}
s_1 &= \frac{\left(I_{et}^4 - 12\eta I_{et}^2 + 4(I_{et}^2 - 2\eta)\omega_c^2\right)\omega_e^2}{2I_{et}N_3N_4(\omega_c^2 + N_1)} + \frac{I_{et}(I_{et}^2 + 4\omega_c^2 - 2\eta)\omega_e^4}{2N_3N_4\omega_c^2(\omega_c^2 + N_1)} \\
&\quad - \frac{(I_{et}^2 + \omega_c^2)(I_{et}^2 + 4\omega_c^2 - 8\eta)\omega_e}{2N_3N_4(\omega_c^2 + N_1)} - \frac{(I_{et}^4 + 5\omega_c^2 I_{et}^2 - 2\eta I_{et}^2 + 4\omega_c^4)\omega_e^3}{2N_3N_4\omega_c^2(\omega_c^2 + N_1)} \\
s_2 &= \frac{\omega_e}{N_3}, \quad s_5 = \frac{\omega_e^2}{\omega_c N_3} \\
s_3 &= -\frac{\omega_e\left(\omega_c^6 - 6\eta\omega_c^4 + 2\omega_e^6 + (5\omega_c^2 - 4\eta)\omega_e^4 + (4\omega_c^4 - 18\eta\omega_c^2)\omega_e^2\right)}{2N_3^2\omega_c^2\left(\omega_c^2 + N_2\right)} \\
&\quad - \frac{I_{et}\omega_e\left(I_{et} + 3\omega_e\right)\left(\omega_c^4 - 6\eta\omega_c^2 + \omega_e^4 - 2(\eta - \omega_c^2)\omega_e^2\right)}{2N_3^2\omega_c^2(\omega_c^2 + N_2)} + \frac{\eta\omega_e^2}{I_{et}N_3\left(\omega_c^2 + N_2\right)} \\
s_4 &= -\frac{\omega_e\left(2N_4\omega_e(\omega_c^2 - I_{et}\omega_e) + I_{et}N_3(4\omega_c^2 + 3N_4 + I_{et}\omega_e)\right)}{4I_{et}N_3^2N_4\omega_c^2} \\
s_6 &= \frac{3k_3}{8\omega_c^3} + \frac{\eta\omega_c\left(3I_{et}N_4 + \omega_e(I_{et} + \omega_e)(3I_{et} + 4\omega_e)\right)}{2I_{et}N_3^2N_4} \\
&\quad + \frac{\eta\omega_e\left(8\omega_c^4 + I_{et}\omega_e(2I_{et}^2 + 2\omega_e I_{et} - \omega_e^2)\right)}{2I_{et}N_3^2N_4\omega_c}
\end{aligned}
\tag{5.30}
$$

where

$$
\begin{aligned}
&N_1 = I_{et}^2 - 2\omega_e I_{et} + \omega_e^2\,, \quad N_2 = I_{et}^2 + 2\omega_e I_{et} + \omega_e^2 \\
&N_3 = \omega_c^2 + \omega_e^2\,, \quad N_4 = I_{et}^2 + 4\omega_c^2
\end{aligned}
\tag{5.31}
$$

The fixed points of the modulation equations $(a_\circ, \gamma_\circ)$ are obtained by setting the time derivatives in (5.29) equal to zero and solving a third-order algebraic equation for the fixed points.

Substituting the first-order and second-order solutions, (5.27) and (5.28), into (5.22), substituting the fixed points of the modulation equations, and dropping the exponentially decaying terms, we obtain the second-order approximation of the response of the MPG as

$$\begin{aligned} u_1 &= c_{11} a_\circ^2 \cos(2\hat{\Omega}\hat{t} + 2\gamma_\circ) + c_{12} a_\circ^2 \sin(2\hat{\Omega}\hat{t} + 2\gamma_\circ) + c_{13} a_\circ^2 \\ u_2 &= c_{21} a_\circ \cos(\hat{\Omega}\hat{t} + \gamma_\circ) + c_{22} a_\circ \sin(\hat{\Omega}\hat{t} + \gamma_\circ) \\ u_3 &= \frac{1}{\omega_c} a_\circ \sin(\hat{\Omega}\hat{t} + \gamma_\circ) \\ u_4 &= \frac{\hat{\Omega}}{\omega_c} a_\circ \cos(\hat{\Omega}\hat{t} + \gamma_\circ) \end{aligned} \tag{5.32}$$

where the coefficients c_{ij} are

$$\begin{aligned} &c_{11} = \frac{\omega_e(2\omega_e - I_{et})}{2N_3N_4}, \quad c_{12} = \frac{\omega_e(I_{et}\omega_e + 2\omega_c^2)}{2\omega_c N_3 N_4}, \quad c_{13} = \frac{\omega_e}{2I_{et}N_3} \\ &c_{21} = \frac{\omega_e}{N_3}, \quad c_{22} = \frac{-\omega_e^2}{\omega_c N_3} \end{aligned} \tag{5.33}$$

The mean extracted power P_e can be found in closed-form by substituting the steady-state velocity u_4 in equation (5.11) and carrying out the integration. The result is

$$P_e = -\frac{\hat{\Omega}\hat{A}_\circ}{2\omega_c\eta} a_\circ \cos\gamma_\circ - \frac{\zeta_m \hat{\Omega}^2}{\eta\omega_c^2} a_\circ^2 \tag{5.34}$$

We note that the output power depends implicitly on ω_e through $a_\circ$ and $\gamma_\circ$.

The equilibruim solution was used to generate the frequency-response curves of the inertial mass displacement for MPG #1 where the load resistance was set so that $\omega_e = 0.145$. These curves are compared in Figure 5.6 to the frequency-response curves obtained by numerically integrating equations (5.7) at the four levels of base excitation amplitudes $\hat{A}_\circ = 0.003$, 0.01, 0.015, and 0.02. The figure shows good agreement between the numerical and analytical results. The frequency-response curves are all bent to the right, indicating that the effective electromechanical nonlinearity is of the hardening-type. These results explain the reason for the underestimation of the linear model for the excitation frequency at which peak power occurs $\hat{\Omega}_{peak}$, since the hardening nonlinearity shifts the center frequency of the MPG to higher values.

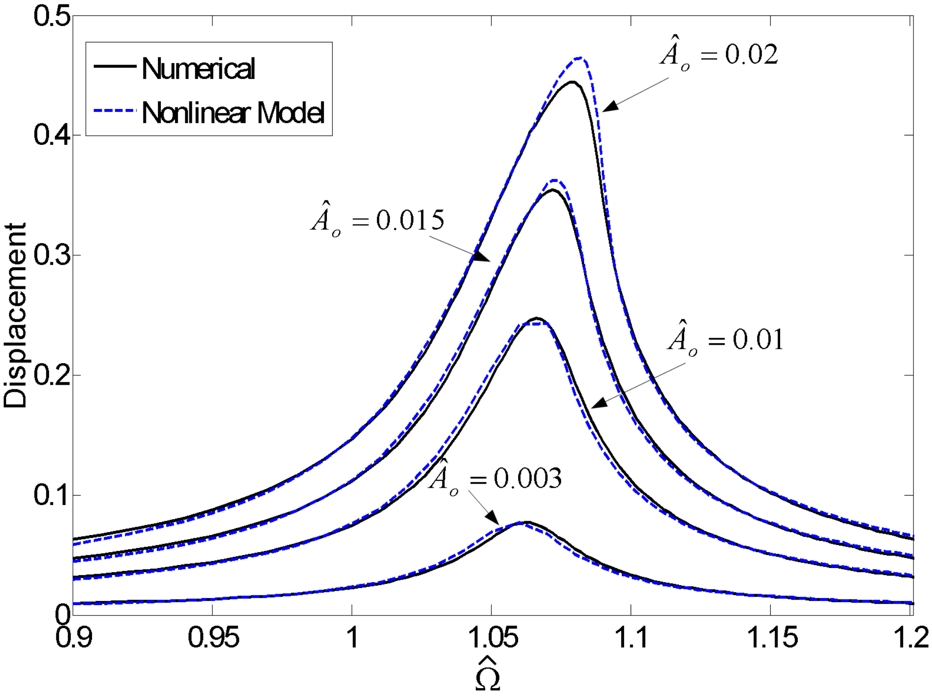

Figure 5.6: The frequency-response curves of the nondimensional displacement $\hat{x}$ at four levels of excitation.

Almost a vertical drop is observed in the response curve of $\hat{A}_\circ = 0.02$ at ($\hat{\Omega} = 1.09$), which indicates the impending appearance of a region of multi-valued responses at higher excitation amplitudes ($\hat{A}_\circ > 0.02$). Although operating the MPG at this level of excitation amplitudes might seem to promise higher levels of extracted power, this promise is complicated by the fact that a lower level of extracted power is also available in the multi-valued region. The actual extracted power in such a region will depend on the initial conditions.

The nonlinear model offers significant improvements in the prediction of the output power and peak frequency as the base excitation exceeds $\hat{A}_\circ > 0.01$. Figure 5.7 shows the peak output power $(P_e)_{peak}$ and the corresponding excitation frequency $\hat{\Omega}_{peak}$ for MPG #2 at a base excitation of $\hat{A}_\circ = 0.02$. The figure shows good agreement between the predictions of the nonlinear model and the results of numerically integrating (5.7). In particular, the deviation in the predicted peak frequency $\hat{\Omega}_{peak}$ is small enough to avoid mistuning the MPG away from the excitation frequency.

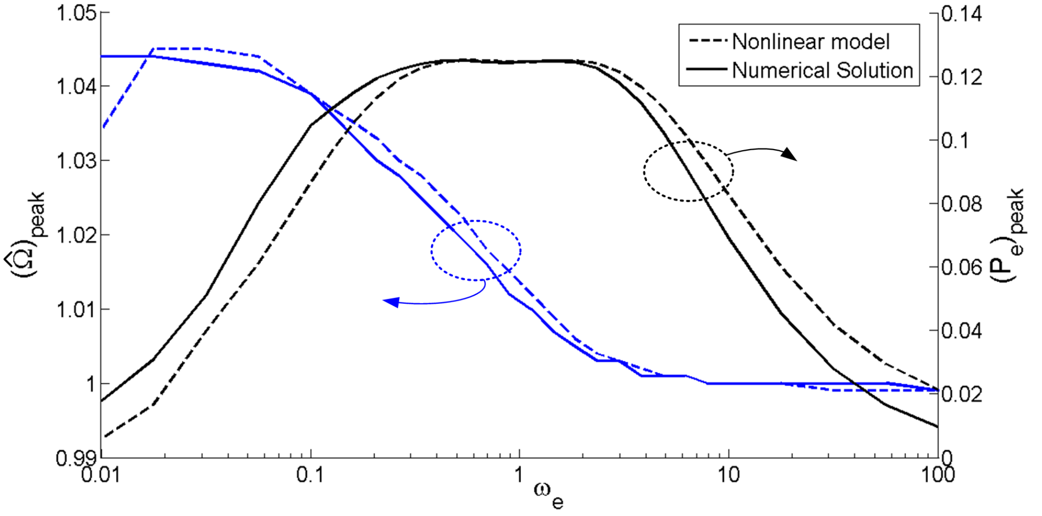

Figure 5.7: Peak output power $(P_e)_{peak}$ (black lines) and the corresponding excitation frequency $\hat{\Omega}_{peak}$ (blue lines) obtained from the full and the nonlinear models for $\hat{A}_\circ = 0.02$.

5.5 Model Validation and Discussion

To validate the nonlinear model of the electrostatic MPG, we compare our results to those experimentally obtained by Bartsch et al. [6] for an MPG, dubbed MPG #3, with the same architecture as ours. The parameters of the MPG are listed in Table 5.2. Each of the variable capacitors had 55 comb fingers. We estimated the stiffness of the support springs using static deflection analysis in the FEM code COMSOL. Bartsch et al. [6] used a power source, rather than an electret, to supply the voltage drop to the common capacitor. Therefore, we set ($C_{et} = \infty$). Further, the realized MPG had a significant

Table 5.2: Dimensions and Properties of MPG #3 [6, 7].

m	$0.1\,\mu$Kg	h	$30.0\,\mu$m
$C_\circ$	0.122 pF	C_p	0.12 pF
V_{et}	70 V	η	0.0956
k_1	6.931 N/m	k_3	14.5

parasitic capacitance C_p [7], which was factored in our model shifting the static charge on the variable capacitors to a value larger than $q_\circ$ and decreasing the electrical subsystem frequency ω_e and I_{et}.

Figure 5.8 compares the maximum displacement of the inertial mass x predicted using our model to their experimental results for two frequency sweeps at constant base displacement amplitudes of $y_\circ = 0.1\,\mu$m and $0.2\,\mu$m. A region of multi-valued responses appears at $\Omega = 1696$ Hz and $\Omega = 1738$ Hz for the small and large excitation amplitudes, respectively, where the experimental frequency-response curves exhibit a sudden drop. Our model was able to predict the experimental results well except for the high-frequency region of the large excitation frequency-response curve. In this region, the piezoelectric actuator that was used to supply the base excitation sees the most significant challenge to maintain a constant displacement amplitude as the frequency of excitation increases, which can be expected to decrease the realizable excitation amplitude, consistent with our model overestimation of the response.

In this chapter, we studied the system dynamics of electrostatic MPGs and found that the strength of electromechanical coupling in these MPGs depends on the magnitude of the electrical frequency ω_e and that two qualitatively different domains of MPG behavior exist. In the fast domain $\omega_e > 1$ (small load resistance), the electromechanical coupling is weak and the MPG behaves as a linear viscously damped system with the maximum output power occurring at $\hat{\Omega} = 1$. In the slow and mixed domains $\omega_e \leq 1$ (large load

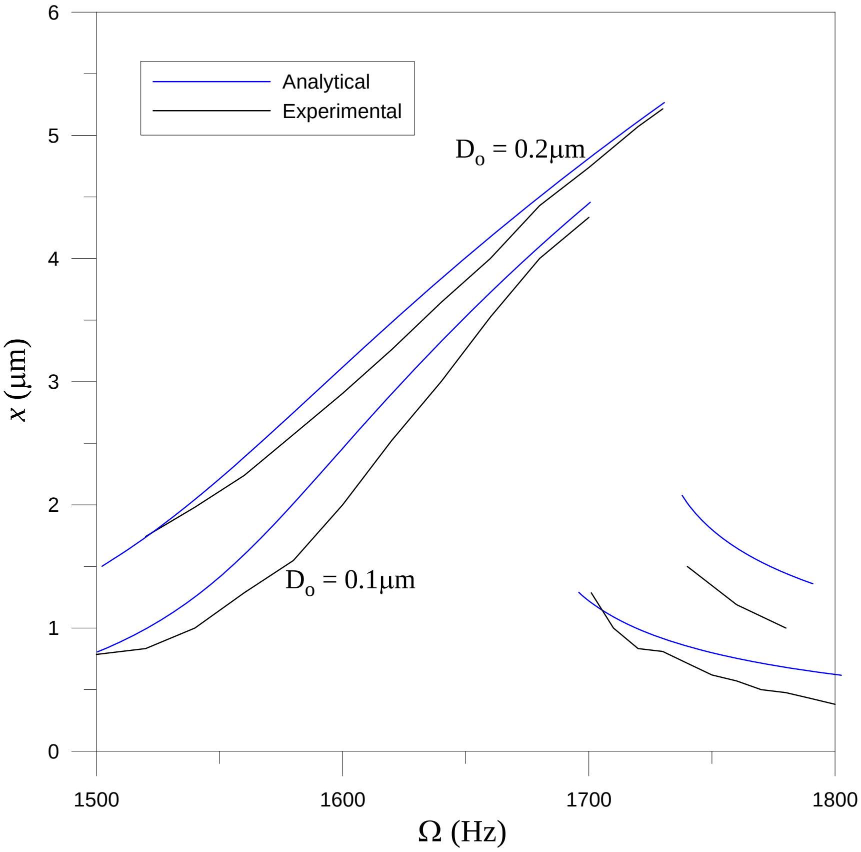

Figure 5.8: The maximum displacement of the inertial mass x as a function of the excitation frequency Ω.

resistance), the electromechanical coupling is strong, thereby introducing a hardening-type effective nonlinearity in the system response and shifting the maximum output power to the neighborhood of $\hat{\Omega} = \sqrt{1+2\eta}$. As a result, electrostatic MPGs have two distinct, fast and slow, optimal operating points.

It is possible to merge these optimal operating points in an intermediate range ($\omega_e \sim 1$) to obtain a wideband MPG. The design of wideband MPGs requires simultaneous optimization of the power output and locations of the operating points, which is obtained by satisfying the following design rules:

- The electromechanical coupling coefficient should be set to $\eta \approx \zeta_m$
- The load resistance should be set so that the frequency of the electrical subsystem lies in the domain: $\omega_e \in [\frac{\eta}{\zeta_m}, \frac{\zeta_m}{\eta}\omega_c^2]$

Linear and simplified linear models were found to be adequate for predicting the response of MPGs operating in the fast domain and lightly-excited MPGs ($\hat{A}_\circ \leq 0.01$) operating in the slow or mixed domains. This limitation is particularly important, since one of the two optimal operating points exists in the slow domain.

To address this need, we developed a nonlinear model and validated here. The model was found to be valid for MPGs operating under tight electromechanical coupling conditions (slow and mixed domain) and for moderately large base excitations. Although the model diverges for large excitations $\hat{A}_\circ \geq 0.03$, this is not a significant limitation since large displacements lead to multi-valued responses. This is an undesirable feature in MPGs since it makes the power output sensitive to initial conditions (environmental disturbances) and thereby unpredictable.

We also presented a general and analytical approach to identify the damping mechanism in electrostatic and piezoelectric MPGs more rigorous than merely observing that electrostatic MPGs are mostly Coulomb-damped and piezoelectric MPGs are mostly viscous-damped [21]. Using our analytical approach, we found that the damping in electrostatic and piezoelectric MPGs can be either viscous or Coulomb, depending on their time constants and whether they operate in the fast or the slow domain. We also found that their damping can be a mixture of both mechanisms in the mixed domain where the damping of the electric subsystem can not be reduced to either of these damping mechanisms and has to be included explicitly in the overall system dynamics. That is true even for lightly excited MPGs ($\hat{A}_\circ \leq 0.01$), where a coupled linear model can be used to represent the contribution of the electrical and mechanical subsystems to the overall system dynamics.

Chapter 6

Conclusions

6.1 Thesis Contributions

The major contributions of the thesis can be summarized as follows:

- A switchless electrostatic out-of-plane micro-power generator was modeled, designed, fabricated and tested. The new generator is sensitive enough to extract output power at very low base excitations. It is designed to use a ready-made electret as a charging source and is therefore portable and self-sustained. Moreover, the new MPG can be configured as a wideband MPG in its impact mode of operation. A bandwidth of up to 9 Hz has been realized in this mode of operation. An improved version of the MPG was found to produce almost 1mW output power at a base excitation amplitude and frequency of $0.08\,g$ (RMS) and 86 Hz. Two nonlinear models were developed to model the free-flight and impact modes of operation for this MPG allowing for further future system analysis and optimization.
- A new implementation of the in-plane electrostatic transducer was designed, fabricated using MEMS surface micromachining, and tested. It is estimated that the new

implementation can achieve 78% more output power than the original implementation [5]. This implementation was used in the fabrication of a novel MPG where the source voltage is unlimited by the pull-in instability and a low MPG center frequency can be realized. The MPG uses charged silicon nitride as a charging source. The MPG produces 65mV at a base acceleration amplitude and frequency of 2 g and 1.1 kHz. The prototype achieves 27% less MPG center frequency with only one eights the size of the previous implementation [4].

- A new MPG architecture was developed that eliminates the need for restoring force elements (springs) in the MPG. The architecture can realize arbitrarily low MPG center frequency. It is suitable for both rectilinear and cylindrical structures and can be used with different vibration energy transduction methods. A prototype was fabricated and tested to demonstrate the feasibility of this architecture. The center frequency of the prototype was found to be 2 Hz demonstrating low frequency operation.
- A consistent approximate analytical solution is developed to describe the nonlinear behavior of switchless comb-finger electrostatic MPGs. The method of multiple scale was used to develop such model. The model was found to be valid for MPGs operating under tight electromechanical coupling conditions and for moderately large base excitations.

6.2 Future work

The work presented in this thesis represented different novel MPGs to tackle different challenges in electrostatic MPGs. The experimental results of the developed prototypes demonstrated their success in overcoming many of the ES MPGs' challenges existing in the literature. These results were further used to develop robust models that accurately describe the behavior of switchless ES MPGs. The general frame work of future work of this thesis well be the use of these models to optimize the present prototype for optimal power generation. Some of these future directions are:

- Developing miniaturized out-of-plane switchless ES MPGs using MEMS technology.
- Developing and charging of electret using both organic (polymers) and inorganic (silicon dioxide and nitride) materials.
- Developing of post-processing techniques for further enhancement of the robustness of the dimple-based suspension.
- Deploying springless MPGs operation in different transduction mechanisms using both linear and cylindrical guides

Bibliography

[1] N. E. DuToit, B. L. Wardle, and S. G. Kim. Design considerations for mems-scale piezoelectric mechanical vibration energy harvesters. *Integrated Ferroelectrics*, 71:121–160, 2005. x, 8, 9, 122

[2] S. J. Roundy. *Energy Scavenging for Wireless Sensor Nodes with a Focus on Vibration to Electricity Conversion*. PhD thesis, University of California at Berkeley, Berkeley CA, May 2003. xi, 6, 12, 13, 21, 30, 65, 79, 80

[3] M. Miranda. *Electrostatic vibration-to-electric energy conversion*. PhD thesis, Massachusetts Institute of Technology, 2004. x, 8, 9, 20

[4] D. Hoffmann, B. Folkmer, and Y. Manoli. Fabrication, characterization and modelling of electrostatic micro-generators. *Journal of Micromechanics and Microengineering*, 19:094001 (11pp), 2009. x, 62, 93, 95, 138

[5] F. Peano and T. Tambosso. Design and optimization of a mems electret-based capacitive energy scavenger. *Journal of Microelectromechanical Systems*, 14(3):429–435, 2005. x, 64, 70, 75, 76, 77, 80, 120, 121, 122, 123, 126, 138

[6] U. Bartsch, A. Trautmann, P. Ruther, J. Gaspar, and O. Paul. Electrostatic transducers for micro energy harvesting based on soi technology. In *TRANSDUCERS and EUROSENSORS 2007*, pages 141–144, Lyon, France, 2007. x, 28, 64, 70, 80, 133, 134

[7] U. Bartsch and O. Paul. *Private communications*, 2009. x, 134

[8] www.mide.com. xi, 12, 13

[9] C. Williams, C. Shearwood, M. Harradine, P. Mellor, T. Birch, and R Yates. Development of an electromagnetic micro-generator. *IEE Proceedings on Circuits Devices Systems*, 148(6):337–342, 2001. xi, 14, 15

[10] www.perpetuum.co.uk. xi, 15

[11] S. Meninger. A low power controller for a mems based energy converter. Master's thesis, Massachusetts Institute of Technology, 1999. xi, 19, 21

[12] R. Tashiro, N. Kabei, K. Katayama, Y. Ishizuka, and K. Tsuchiya. Development of an electrostatic generator that harnesses the motion of a living body. *JSME International Journal*, 43(4):916–922, 2000. xi, 20, 22

[13] M. Miyazaki, H. Tanaka, and K Yano. Electric-energy generation using variable-capacitive resonator for power-free lsi: Efficiency analysis and fundamental experiment. In *Proceedings of the 2003 International Symposium on Low Power Electronics and Design*, pages 193–198, Seoul, Korea, 2003. xi, 21, 23

[14] P. Miao, A. S. Holmes, E. M. Yeatman, T. C. Green, and P. D. Mitcheson. Micromachined variable capacitors for power generation. In *Proceedings of Electrostatics 2003*, Edinburgh, UK, 2003. xi, 22, 24

[15] P. D. Mitcheson, T. C. Green, E. M. Yeatman, and A. S. Holmes. Architectures for vibration-driven micropower generators. *IEEE Journal of Microelectromechanical Systems*, 13(3):429–440, 2004. xi, 2, 8, 23, 24, 116

[16] J. Boland, Y. Chao, Y. Suzuki, and Y. C. Tai. Micro electret power generator. In *MEMS 2003*, pages 538–541, Kyoto, Japan, 2003. xi, 25, 26, 116

[17] T. Tsutsumino, Y. Suzuki, N. Kasagi, K. Kashiwagi, and Y. Morizawa. Micro seismic electret generator for energy harvesting. In *PowerMEMS 2006*, pages 279–282, California, USA, 2006. xi, 25, 26

[18] M. Edamoto, Y. Suzuki, N. Kasagi, K. Kashiwagi, Y. Morizawa, T. Yokoyama, T. Seki, and M. Oba. Low-resonant-frequency micro electret geenrator for energy harvesting application. In *MEMS 2009*, pages 1059–1062, Sorrento, Italy, 2009. xii, 26, 27, 62, 116

[19] Y. Naruse, N. Matsubara, K. Mabuchi, M. Izumi, and S. Suzuki. Electrostatic micro power generation from low-frequency vibration such as human motion. *Journal of Micromechanics and Microengineering*, 19:094002 (5pp), 2009. xii, 27, 28, 99

[20] T. Sterken, P. Fiorini, K. Baert, R. Puers, and G. Borghs. An electret-based electrostatic μ-generator. In *TRANSDUCERS 2003*, pages 1291–1294, Boston, USA, 2003. xiv, 28, 64, 70, 71, 72, 76, 80, 84, 116, 117, 122

[21] P. D. Mitcheson, E. M. Yeatman, G. K. Rao, A. S. Holmes, and T. C. Green. Energy harvesting from human and machine motion for wireless electronic devices. *Proceedings of the IEEE*, 96(9):1457–1486, 2008. 1, 7, 8, 12, 14, 136

[22] M. T. Penella, G. Forner, and Others. A review of commercial energy harvesters for autonomous sensors. In *Instrumentation and Measurement Technology Conference - IMTC 2007*, pages 1–5, Warsaw, Poland, 2007. 2

[23] S. Roundy, P. K. Wright, and J. Rabaey. A study of low level vibrations as a power source for wireless sensor nodes. *Computer Communications*, 26(11):1131–1144, 2003. 6

[24] L. Mateu. Energy harvesting from passive human power. *Wearable Computers*, 2004. 7

[25] L. Mateu. Review of energy harvesting techniques and applications for microelectronics. *Proceedings of SPIE*, 5837:359–373, 2005.

[26] D. Dunn-Rankin, E. M. Leal, and D. Walther. Personal power systems. *Progress in Energy and Combustion Science*, 31:422–465, 2005. 6

[27] J. A. Paradiso and T. Starner. Energy scavenging for mobile and wireless electronics. *IEEE Pervasive Computing*, 4(1):18–27, 2005. 6, 7

[28] S. P. Beeby, M. J. Tudor, and N. M. White. Energy harvesting vibration sources for microsystems applications. *Measurement Science and Technology*, 17(12):R175–R195, 2006. 8, 11, 12, 14

[29] H. A. Sodano, D. J. Inman, and G. Park. A review of power harvesting from vibration using piezoelectric materials. *Shock and Vibration Digest*, 36(3):197–206, 2004.

[30] S. R. Anton and H. A. Sodano. A review of power harvesting using piezoelectric materials (2003-2006). *Smart Materials and Structures*, 16(3):R1–R21, 2007. 12

[31] D. P. Arnold. Review of microscale magnetic power generation. *IEEE Transactions on Magnetics*, 43(11):3940–3951, 2007. 14

[32] A. D. Moore. *Electrostatics and Its Application.* John Wiley, 1973. 16, 25

[33] A. W. Simon. Theory of the frictional van de graaff electrostatic generator. *American Journal of Physics*, 43(12):1108–1110, 1975. 16

[34] S. Meninger, J. O. Mur-Miranda, R. Amirtharajah, A. Chandrakasan, and J. H. Lang. Vibration-to-electric energy conversion. *IEEE Transactions on Very Large Scale Integration (VLSI) Systems*, 9(1):64–76, 2001. 19, 64, 70, 80, 81, 87

[35] G. Despesse, T. Jager, J. Chaillout, S. Basrour, and B. Chalot. Fabrication and characterisation of high damping electrostatic micro devices for vibration energy scavenging. In *DTIP 2005*, pages 386–390, Montreux, Switzerland, 2005. 22

[36] G. M. Sessler, editor. *Topics in Applied Physics: Electrets*. Springer-Verlag, 1987. 25, 47, 58, 72

[37] Y. Tada. Experimental characteristics of electret generator, using polymer film electrets. *Japanese Journal of Applied Physics*, 31:846–851, 1992. 25

[38] T. Tsutsumino, Y. Suzuki, N. Kasagi, and Y. Sakane. Seismic power generator using high-performance polymer electret. In *MEMS 2006*, pages 98–101, Istanbul, Turkey, 2006. 25, 26

[39] T. Tsutsumino, Y. Suzuki, and N. Kasagi. Electromechanical modeling of micro electret generator for energy harvesting. In *TRANSDUCERS and EUROSENSORS 2007*, pages 863–866, Lyon, France, 2007. 26, 116

[40] Y. Suzuki and Y. C. Tai. Micromachined high-aspect ratio parylene spring and its application to low-frequency accelerometers. *Journal of Micromechanics and Microengineering*, 15:1364–1370, 2006. 27

[41] Y. Tsurumi, Y. Suzuki, and N. Kasagi. Non-contact electrostatic micro-bearing using polymer electret. In *MEMS 2008*, pages 511–514, Arizona, USA, 2008. 27

[42] Y. Suzuki, M. Edamoto, N. Kasagi, K. Kashiwagi, Y. Morizawa, T. Yokoyama, T. Seki, and M. Oba. Micro electret energy harvesting device with analogue impedance conversion circuit. In *Power MEMS 2008*, pages 7–10, Sendai, Japan, 2008. 27

[43] A. Modafe, N. Ghalichechian, A. Frey, J. H. Lang, and R. Ghodssi. Microball-bearing-supported electrostatic micromachines with polymer dielectric films for elec-

tromechanical power conversion. *Journal of Micromechanics and Microengineering*, 16:S182S190, 2006. 27

[44] U. Bartsch, P. Ruther, and O. Paul. Elektromechanischer energiewandler basierend auf soi-technologie. *Technisches Messen 74*, 20:636 – 641, 2007. 28, 62, 116

[45] H. Amjadi and C. Thielemann. Silicon-based inorganic electrets for application in micromachined devices. *IEEE Transaction on Dielectrics and Electrical Insulation*, 3(4):494–498, 1996. 29

[46] C. B. Williams and R. B. Yates. Analysis of a micro-electric generator for microsystems. *Sensors and Actuators A: Physical*, 52:8–11, 1996. 38, 80, 96, 116, 123

[47] G. K. Fedder. *Simulation of Microelectromechanical Systems.* PhD thesis, University of California at Berkely, 1994. 39, 41

[48] M. Soliman, E. M. Abdel-Rahman, E. F. El-Saadany, and R. R. Mansour. A wideband vibration-based energy harvester. *Journal of Micromechanics and Microengineering*, 18:115021 (11pp), 2008. 50, 96, 111

[49] M. Soliman, E. M. Abdel-Rahman, E. F. El-Saadany, and R. R. Mansour. Design procedure for wideband micropower generators. *Journal of Microelectromechanical Systems*, 18(6):1057–7157, 2009. 51, 53

[50] H. Kloub, D. Hoffmann, B. Folkmer, and Y. Manoli. A micro capacitive vibration energy harvester for low power electronics. In *PowerMEMS 2009*, pages 165–168, Washington DC, USA, 2009. 62, 64, 70, 80

[51] D. Elata and V. Leus. How slender can comb-drive fingers be? *Journal of Micromechanics and Microengineering*, 15(5):1055–1059, 2005. 64, 81

[52] P. D. Mitcheson, T. Sterken, C. He, M. Kiziroglou, E. M. Yeatman, and R. Puers. Electrostatic microgenerators. *Measurement and Control*, 41(4):114 – 119, 2008. 79

[53] W. S. N. Trimmer. Microrobots and micromechanical systems. *Sensors and Actuators*, 19(3):267–287, 1989. 79

[54] N. G. Stephen. On energy harvesting from ambient vibration. *Journal of Sound and Vibration*, 293:409–425, 2006. 80

[55] S. D. Senturia. *Microsystem Design*. Kluwer Academic Publishers, 2001. 82

[56] MEMSCAP. *PolyMUMPs Design Handbook*. 2003. 86

[57] S. Fouladi, M. Bakri-Kassem, and R. R. Mansour. Suspended on-chip rf mems components fabricated using polymumps technology. *Canadian journal of electrical and computer engineering*, 31(2):105–109, 2006. 88

[58] M. Ferraria, V. Ferraria, M. Guizzettia, B. Andb, S. Bagliob, and C. Trigonab. Improved energy harvesting from wideband vibrations by nonlinear piezoelectric converters. *Procedia Chemistry*, 1(1):1203–1206, 2009. 96

[59] J. Moehlis, B. E. DeMartini, J. L. Rogers, and K. L. Turner. Exploiting nonlinearity to provide adaptable energy harvesting. In *Proceedings of ASME Dynamic Systems and Control Conference DSCC2009*, California, USA, 2009. 96

[60] S. Roundy, E. S. Leland, J. Baker, E. Carleton, E. Reilly, E. Lai, B. Otis, J. M. Rabaey, P. K. Wright, and V. Sundararajan. Improving power output for vibration-based energy scavengers. *IEEE Pervasive Computing*, 4(1):28–36, Jan.-March 2005. 116

[61] M. A. Mahmoud, E. F. El-Saadany, and R. R. Mansour. Planar electret based

electrostatic micro-generator. In *PowerMEMS 2006*, pages 223–226, California, USA, 2006. 116

[62] F. Peano, G. Coppa, C. Serazio, F. Peinetti, and A. D'angola. Nonlinear oscillations in a mems energy scavenger. *Mathematical and Computer Modeling*, 43:1412–1423, 2006. 126

[63] A. H. Nayfeh. *Introduction to perturbation techniques*. Wiley-Interscience, New York, 1981. 126

[64] Y. Arakawa, Y. Suzuki, and N. Kasagi. Micro seiemic power generator using electret polymer film. In *PowerMEMS 2004*, pages 187–190, Kyoto-Japan, 2004.

[65] P. Basset, D. Galayko, A. M. Paracha, F. Marty, A. Dudka, and T. Bourouina. A batch-fabricated and electret-free silicon electrostatic vibration energy harvester. *Journal of Micromechanics and Microengineering*, 19:115025 (12pp), 2009.

[66] T. von Buren, P. D. Mitcheson, T. C. Green, E. M. Yeatman, A. S. Holmes, and G. Troster. Optimization of inertial micropower generators for human walking motion. *IEEE Sensors Journal*, 6(1):28–38, 2006.

[67] Y. Chiu, C. T. Kuo, and Y. S. Chu. Mems design and fabrication of an electrostatic vibration-to-electricity energy converter. *Microsystem Technologies*, 133:1663–1669, 2007.

[68] Y. Chiu and V. F. G. Tseng. A capacitive vibration-to-electricity energy converter with integrated mechanical switches. *Journal of Micromechanics and Microengineering*, 18:104004 (8pp), 2008.

[69] N. E. Dutoit and B. L. Wardle. Performance of microfabricated piezoelectric vibration energy harvesters. *Integrated Ferroelectrics*, 83:13–32, 2006.

[70] M. Edamoto, Y. Suzuki, and N. Kasagi. Electret-based energy harvesting device with parylene flexible springs. In *Asia-Pacific Conference on Transducers and Micro-Nano Technology*, pages 22 – 25, Tainan, Taiwan, 2008.

[71] N. Fondevilla, C. Serre, A. Perz-Rodrguez, M. C. Acero, J. Esteve, and J. R. Morante. Electromagnetic harvester device for scavenging ambient mechanical energy with slow, variable, and randomness nature. In *PowerMEMS 2009*, pages 225–228, Washington DC., USA, 2009.

[72] T. Genda, S. Tanaka, and M. Esashi. High power electrostatic motor and generator using electrets. In *TRANSDUCERS 2003*, pages 492–495, Boston, USA, 2003.

[73] S. M. Gracewski, P. D. Funkenbusch, Z. Jia, D. S. Ross, and M. D. Potter. Design and modeling of a micro-energy harvester using an embedded charge layer. *Journal of Micromechanics and Microengineering*, 16:235–241, 2006.

[74] J. P. Den Hartog. Forced vibrations with combined coulomb and viscous friction. *ASME Journal of Applied Mechanics*, 53:107–115, 1931.

[75] A. Khaligh, P. Zeng, and C. Zheng. Kinetic energy harvesting using piezoelectric and electromagnetic technologies: State of the art. *IEEE Transactions On Industrial Electronics*, 57(3):850–860, 2010.

[76] I. Kuehne, A. Frey, D. Marinkovic, G. Eckstein, and H. Seidel. Power mems–a capacitive vibration-to-electrical energy converter with built-in voltage. *Sensors And Actuators: Physical A*, 142:263–269, 2008.

[77] C. Lee, Y. M.i Lim, B. Yang, R. Kotlanka, C. Heng, J. He, M. Tang, J. Xie, and H. Feng. Theoretical comparison of the energy harvesting capability among various electrostatic mechanisms from structure aspect. *Sensors and Actuators A: Physical*, 156:208–216, 2009.

[78] H. Lo, R. Whang, and Y. C. Tai. A simple micro electret power generator. In *MEMS 2007*, pages 859–862, Colorado, USA, 2007.

[79] W. Ma, R. Zhu, L. Rufer, Y. Zohar, and M. Wong. An integrated floating-electrode electric microgenerator. *Journal of Microelectromechanical Systems*, 16(1):29–37, 2007.

[80] M. A. E. Mahmoud, E. M. Abdel-Rahman, E. F. El-Saadany, and R. R. Mansour. Electro-mechanical coupling in electrostatic micro-power generators. *Smart Materials and Structures*, 19:025007 (8pp), 2010.

[81] M. A. E. Mahmoud, E. M. Abdel-Rahman, E. F. El-Saadany, and R. R. Mansour. Battery-less electrostatic micro-power generator. In *2nd Microsystems and Nanoelectronics Research Conference (MNRC 2009)*, Ottawa, Canada, 2009.

[82] M. A. E. Mahmoud, E. F. El-Saadany, and R. R. Mansour. Modeling and optimization of planar electret-based electrostatic energy harvester. In *ASME International Mechanical Engineering Congress and Exposition*, Seattle, USA, 2008.

[83] C. Marboutin, Y. Suzuki, and N. Kasagi. Optimal design of vibration-driven micro electret generator for energy harvesting. In *PowerMEMS 2007*, pages 141–144, Sendai, Japan, 2007.

[84] D. Miki, M. Honzumi, Y. Suzuki, and N. Kasagi. Large-amplitude mems electret generator with nonlinear spring. In *MEMS 2010*, pages 176–179, Hong Kong, China, 2010.

[85] P. D. Mitcheson, T. C. Green, and E. M. Yeatman. Power processing circuits for electromagnetic, electrostatic and piezoelectric inertial energy scavengers. *Microsystem Technologies*, 13:1629–1635, 2007.

[86] P. D. Mitcheson, P. Miao, B. H. Stark, E. M. Yeatman, A. S. Holmes, and T. C. Green. Mems electrostatic micropower generator for low frequency operation. *Sensors And Actuators: Physical A*, 115:523–529, 2004.

[87] P. D. Mitcheson, E. K. Reilly, T. Toh, P. K. Wright, and E. M. Yeatman. Performance limits of the three mems inertial energy generator transduction types. *Journal of Micromechanics and Microengineering*, 17(9):S211 – S216, Sep. 2007.

[88] P. D. Mitcheson, E. K. Reilly, T. Toh, P. K. Wright, and E. M. Yeatman. Transduction mechanisms and power density for mems inertial energy scavengers. In *PowerMEMS 2006*, pages 2–5, California, USA, 2006.

[89] P. D. Mitcheson, B. H. Stark, P. Miao, E. M. Yeatman, A. S. Holmes, and T. C. Green. Analysis and optimisation of mems electrostatic on-chip power supply for self-powering of slow-moving sensors. In *ACM International Conference on Ubiquitous Computing*, pages 5–6, Goeteborg, Sweden, 2002.

[90] M. Mizuno and D. G. Chetwynd. Investigation of a resonance microgenerator. *Journal of Micromechanics and Microengineering*, 13:209–216, 2003.

[91] E. Romero, M. R. Neuman, and R. O. Warrington. Kinetic energy harvester for body motion. In *PowerMEMS 2009*, Washington DC., USA, 2009.

[92] Y. Sakane, Y. Suzuki, and N. Kasagi. The development of a high-performance perfluorinated polymer electret and its application to micro power generation. *Journal of Micromechanics and Microengineering*, 18:104011 (6pp), 2008.

[93] Y. Sakane, Y. Suzuki, and N. Kasagi. Performance perfluorinated polymer electret film for micro power generation. In *PowerMEMS 2007*, pages 53–56, Freiburg, Germany, 2007.

[94] N. Satol, H. Ishii, M. Urano, T. Sakata, J. Teradal, H. Morimura, S. Shigematsu, K. Kudou, and K. Machida. Novel mems power generator with integrated thermoelectric and vibrational devices. In *The 13th Intemarional Conference on Solid-state Sensors, Actuators and Microsystems*, pages 5–8, Seoul, Korea, 2005.

[95] P. Spies, M. Pollak, and G. Rohmer. Power management for energy harvesting applications. In *PowerMEMS 2007*, pages 6–11, Freiburg, Germany, 2007.

[96] B. H. Stark, P. D. Mitcheson, P. Miao, T. C. Green, E. M. Yeatman, and A. S. Holmes. Converter circuit design, semiconductor device selection and analysis of parasitics for micropower electrostatic generators. *IEEE Transactions on Power Electronics*, 21(1):27–37, 2006.

[97] B. H. Stark, P. D. Mitcheson, P. Miao, T. C. Green, E. M. Yeatman, and A. S. Holmes. Converter circuit design, semiconductor device selection and analysis of parasitics for micropower electrostatic generators. *IEEE Transaction on Power Electronics*, 21(1):27–37, 2006.

[98] B. H. Stark, P. D. Mitcheson, P. Miao, T. C. Green, E. M. Yeatman, and A. S. Holmes. Power processing issues for micro-power electrostatic generators. In *IEEE 35th Annual Power Electronics Specialists Conference, 2004. PESC 04. 2004*, pages 4156–4162, Aachen, Germany, 2004.

[99] T. Sterken, K. Baert, R. Puers, G. Borghs, and R. Mertens. A new power mems component with variable capacitance. In *Proceedings of Pan Pacific Microelectronics Symposium 2003*, pages 27–34, Hawaii, USA, 2003.

[100] T. Sterken, K. Baert, C. Vanhoof, R. Puers, G. Borghs, and P. Fiorini. Comparative modelling for vibration scavengers. *Proceedings of IEEE Sensors*, 3:1249–1252, 2004.

[101] T. Sterken, P. Fiorini, G. Altena, C. van Hoof, and R Puers. Harvesting energy from vibrations by a micromachined electret generator. In *TRANSDUCERS 2007*, pages 129–132, Lyon, France, 2007.

[102] T. Sterken, P. Fiorini, K. Baert, G. Borghs, and R. Puers. Novel design and fabrication of a mems electrostatic vibration scavenger. In *PowerMEMS 2004*, pages 18–21, Kyoto, Japan, 2004.

[103] Erick O Torres. Energy-harvesting system-in-package microsystem. *Journal of Energy Engineering*, 134(4):121–129, 2008.

[104] E. O. Torres and G. A. Mora. Electrostatic energy-harvesting and battery-charging cmos system prototype. *IEEE Transactions On Circuits And Systems*, 56(9):1938–1948, 2009.

[105] E. O. Torres and G. A. Rincón-Mora. Electrostatic energy harvester and li-ion charger circuit for micro-scale applications. In *IEEE Midwest Symposium on Circuits and Systems (MWSCAS), San Juan, Puerto Rico*, pages 65–69, 2006.

[106] T. Tsutsumino, Y. Suzuki, N. Kasagi, and Y. Tsurumi. High-performance polymer electret for micro seismic generator. In *PowerMEMS 2005*, pages 9–12, Tokyo, Japan, 2005.

[107] L. Tvedt, L. Blystad, and E. Halvorsen. Simulation of an electrostatic energy harvester at large amplitude narrow and wide band vibrations. In *DTIP 2008*, pages 296–301, Riviera, France, 2008.

[108] B. Vel, D. Hohlfeld, and V. Pop. Harvesting mechanical energy for ambient intelligent devices. *Information Systems Frontiers*, 11:7–18, 2009.

[109] B. Yen and J. Lang. A variable-capacitance vibration-to-electric energy harvester.

IEEE Transactions On Circuits And Systems–I: Regular Papers, 53(2):288–295, 2006.